International Conference on Advances and Innovations in Engineering

2.ICAIE

Conference Date
21-23 September

www.icaie.org.tr **2023**

Fırat University, Atatürk Culture and Congress Center

15 June 2023
Deadline for abstract submission

1 August 2023
Deadline for full-text submission

SPONSORS

arslanlı

MİRYILDIZ
MÜH.İNŞ.TİC.İTH.VE İHR.LTD.ŞTİ.

MEGA
Insulation Solutions

ALKEN İNŞAAT

2.ICAIE

2. International Conference on Advances and Innovations in Engineering

Abstracts Submissions Book

21-23th SEPTEMBER 2023

Fırat University Engineering Faculty /
ELAZIĞ

Editor in Chief
Erkut YALÇIN

Editor
M. Sefa ÇETİN

Fırat University

Honour Committee of the ICAIE

Prof. Dr. Fahrettin GÖKTAŞ, Rector
Prof. Dr. Mehmet YILMAZ, Vice Rector
Prof. Dr. Ebru AKPINAR, Dean

Committee Members

Chair of Conference
Prof. Dr. Ebru AKPINAR
Abdulkadir GÜL, Fırat University(Bioengineering)
Ahmet ÇINAR, Fırat University (Computer Engineering)
Akın ODABAŞI, Fırat University (Metallurgical and Materials Engineering)
Alper K. TANYILDIZI, Fırat University (Mechatronics Engineering)
Belkız TORĞUL, Fırat University (Computer Engineering)
Beyza Furtana YALÇIN, Fırat University (Civil Engineering)
Bircan ÇALIŞIR, Fırat University (Electrical and Electronics Engineering)
Çağrı KAYMAK, Fırat University (Mechatronics Engineering)
Erkut YALÇIN, Fırat Universit (Civil Engineering)
M. Barbaros DURMUŞ, Fırat University (Environmental Engineering)
M. Gökhan ALBAYRAK, Fırat University (Metallurgical and Materials Engineering)
M. Sefa ÇETİN, Fırat University (Electrical and Electronics Engineering)
Mehmet Erbil ÖZCAN, Fırat University (Mechanical Engineering)
Mesut GÖR, Fırat University (Civil Engineering)
Mukaddes KARATAŞ, Fırat University (Chemical Engineering)
Mustafa KANIK, Fırat University (Geological Engineering)
Özge Erdoğan YAMAÇ, Fırat University (Civil Engineering)
Özge HANAY, Fırat University (Environmental Engineering)
Sertaç Emre KARA, Fırat University (Mechanical Engineering)
Sinem AKYOL, Fırat University (Software Engineering)
Şeyda TAŞAR, Fırat University (Chemical Engineering)
Veyis SELEN, Fırat University (Bioengineering)
Yılmaz AYDIN, Fırat University (Software Engineering)
Yusuf KARGINOĞLU, Fırat University (Geological Engineering)

Scıentific Committee

A. Didem KILIÇ, Fırat University
A. Erçin ERSUNDU, Yıldız Technical University
A. Garcia HERNANDEZ, RWTH Aachen University
A. Münir ÖZDEMİR, Bursa Technical University
A. Şükran DEMİRKIRAN, Sakarya University
A. Tevfik BİLDİK, Fırat University
Abayhan BURAN, Fırat University
Abdulkadir GÜL, Fırat University
Abdullah Hilmi LAV, İstanbul Technical University
Abdullah SAR, Fırat University
Abdülcelil KÜLEKÇİOĞLU, Fırat University
Abdülhakim ZEYBEK. Muş Alparslan University
Abuzer ÇALIŞKAN, Fırat University
Adem ATMACA, Gaziantep University
Ahmet Arif AYDIN, İnönü University
Ahmet Bedri ÖZER, Fırat University
Ahmet Burak TATAR, Adıyaman University
Ahmet Can ALTUNIŞIK, Karadeniz Technical University
Ahmet ÇINAR, Fırat University
Ahmet ORHAN, Fırat University
Ahmet ÖZER, Fırat University
Ahmet ŞAŞMAZ, Fırat University
Ahmet TÜRK, Manisa Celal Bayar University
Ahmet YILDIZ, Fırat University
Akın ODABAŞI, Fırat University
Ali ARI, İnönü University
Ali TAŞKIRAN, Fırat University
Ali TOPAL, Dokuz Eylül University
Alper BAŞTÜRK, Erciyes University
Alper K. TANYILDIZI, Fırat University
Arif GÜLTEN, Fırat University
Arijit DE, The University of Manchester
Arkadiusz DOBRZYCKI, Poznan University of Technology

Arzu Fırat ERSOY, Karadeniz Technical University
Arzu Yadigar DURSUN, Fırat University
Aslı GİRAY, Alanya Alaaddin Keykubat University
Atike NAZİK, Çukurova University
Ayberk KAYA, Recep Tayyip Erdoğan University
AYÇA AK, Marmara University
Aydın ÇITLAK, Fırat University
Ayhan AKBAL, Fırat University
Ayhan ÜNLÜ, Fırat University
Aykut TOPDEMİR, Fırat University
Ayla ÖZER, Mersin University
Aynur UÇAR, Fırat University
Ayşe Erdoğan YILDIRIM, Fırat University
Ayşe Ruşen DURUCAN,Fırat University
Ayşe Vildan BEŞE, Atatürk University
Ayşe BİÇER, Turgut Özal University
Ayşegül AŞKIN, Eskişehir Osman Gazi University
Ayşegül UÇAR, Fırat University
Aytekim ÇELİK, Fırat University
Aziz AKSOY, Turgut Özal University
Baha Vural KÖK, Fırat University
Bahadır YILMAZ, Bursa Technical University
Bahtiyar ÖZTÜRK, Ondokuz Mayıs University
Banu TAŞKAN, Fırat University
Barbaros DURMUŞ, Fırat University
Barış KARAKAYA, Fırat University
Belkız TORĞUL, Fırat University
Betül AY, Fırat University
Beyda TAŞAR, Fırat University
Beyza Furtana YALÇIN, Fırat University
Bilal ALATAŞ, Fırat University
Bircan ÇALIŞIR, Fırat University
Burak ŞENGÖZ, Dokuz Eylül University
Burak YILDIRIM, Aarhus University
Burçak EBİN, Chalmers University

Burhan ERGEN, Fırat University
Bünyamin AKGÜL, Fırat University
C. Fahir ARISOY, İstanbul Technical University
Calibe Koç TAŞGIN, Fırat University
Canan DÜLGER, İzmir University of Economics
Canan KOÇ, Fırat University
Celal KISTAK, Fırat University
Cemal BÖLÜCEK, Balıkesir University
Cengiz YILDIZ, Fırat University
Cenk YANEN, Fırat University
Cevdet AKOSMAN, Fırat University
Cihan ÖZEL, Fırat University
Çağla DANACI, Fırat University
Çağrı KAYMAK, Fırat University
Davut HANBAY, İnönü University
Deniz ÜNER, Middle East Technical University
Dicle Bal AKKOCA, Fırat University
Dursun BAKIR, Fırat University
Dursun ÖZER, Fırat University
Duygu EVİN, Turgut Özal University
Duygu KAYA, Fırat University
E. Sabri KAYALI, Haliç University
Ebru AKPINAR, Fırat University
Ebubekir ERDEM, Fırat University
Elif AKGÜN, Fırat University
EMİNE CENGİL, Bitlis Eren University
Emine Işıl TOPAL, Fırat University
Emrah ÇELİK, Fırat University
Emre GÜÇLÜ, Fırat University
Emrehan YAVŞAN, Tekirdağ Namık Kemal University
Ender SUVACI Eskişehir Technical University
Engin GÜRTEKİN, Fırat University
Enis GÜNAY, Erciyes University
Ercan AKSOY, Fırat University
Ercan AYDOĞMUŞ, Fırat University

Erdal ÖBEK, Fırat University
Erdal ÖZBAY, Fırat University
Ergin TAŞKAN, Fırat University
Erhan AKIN, Fırat University
Erkan DUMAN, Fırat University
Erkin EREN, Fırat University
Erkut SAYIN, Fırat University
Erkut YALÇIN, Fırat University
Ertan BÜTÜN, Fırat University
Ertan EVİN, Malatya Turgut Özal University
Ertuğrul ÇAMBAY, Bitlis Eren University
Ertuğrul GÜL, Hakkari University
Eser SERT, Malatya Turgut Özal University
Esra İNCE, Fırat University
Esra Tuğrul TUNÇ, Fırat University
Esra YILDIRIM, Fırat University
Esra YÜZGEÇ, Fırat University
F. Rumeysa KÜLEKÇİOĞLU, Fırat University
Fatih ÖZYURT, Fırat University
Fatih KAYA, Fırat University
Fatih TOPALOĞLU, Malatya Turgut Özal University
Fatma MURAT DURANAY, Fırat University
Ferkan SİPAHİ, Gümüşhane University
Fethi KAMIŞLI, Fırat University
Feyza ALTUNBEY ÖZBAY, Fırat University
Figen BALO, Fırat University
Filiz KAR, Fırat University
Fulvio PARISI, University of Naples Federico II
Galip AYDIN, Fırat University
Gamze BİLGEN, Zonguldak Bülent Ecevit University
Gizem ARSLAN, Fırat University
Gökay BAYRAK, Bursa Technical University
Gökhan ALBAYRAK, Fırat University
Gökhan BAŞMAN, Eti Krom Elazığ
Gökhan ERGÜVEN, Munzur University

Gökhan KURNAZ, Fırat University
Gökhan ÖZER, Fatih Sultan Mehmet Vakıf University
Gökmen TAYFUR, İzmir Institute of Technology
Gülbeyi DURSUN, Fırat University
Gülşad Uslu ŞENEL, Fırat University
Gülşah ÇAKMAK, Fırat University
Gülşah KARADUMAN, Fırat University
Gültekin GÖLLER, İstanbul Technical University
Güngör YILDIRIM, Fırat University
H. Lütfi YÜCEL, Fırat University
H. Suha AKSOY, Fırat University
H.Soner ALTUNDOĞAN, Fırat University
Hakan ÇELİK, Fırat University
Halil HASAR, Fırat University
Halil GÖR, Hakkari University
Hande Yüksel BAYRAM, Fırat University
Hanzade AÇMA, İstanbul Technical University
Hasan ÇELİK, Fırat University
Hasan GÜLER, Fırat University
Hasan YETİŞ, Fırat University
Haşim PIHTILI, Fırat University
Hatice KARA, Fırat University
Haydar EREN, Fırat University
Hayrettin CAN, Fırat University
Hediye AYDIN, Kütahya Dumlupınar University
Hossein MOAYEDI, Duy Tan University
Hülya BİÇER, Kütahya Dumlupınar University
Hümeyra ŞAHİN, Fırat University
Hüseyin ÇİMENOĞLU, İstanbul Technical University
Hüseyin KARACA, İnönü University
Hüseyin YAĞLI, Gaziantep University
İbrahim BERKAN AYDİLEK, Harran University
İbrahim TÜRKMEN, Balıkesir University
İhsan DAĞTEKİN, Fırat University
İlhan AYDIN, Fırat University

İnanç ÖZGEN, Fırat University
İrem GÖRGÖZ, Fırat University
İrem MERTYÜZ, Fırat University
İsmail YILDIRIM, Fırat University
Kazım TÜRK, İnönü University
Kelami ŞEŞEN, İstanbul Technical University
Kıvanç DOĞAN, Fırat University
Kübra ARSLANOĞLU, Fırat University
Kübra KOÇAK, Fırat University
Kübra ŞİŞLİOĞLU, Fırat University
Kürşat Esat ALYAMAÇ, Fırat University
Latif ÖZLER, Fırat University
Levent TAŞÇI, Fırat University
Leyla KALENDER, Fırat University
Loke Kok FOONG, Duy Tan University
M. Cihat TUNA, Fırat University
M. Deniz TURAN, Fırat University
M. Emin EMİROĞLU, Fırat University
M. Erbil ÖZCAN, Fırat University
M. Salih KESKİN, Dicle University
Mahmut PALUTOĞLU, Fırat University
Mahmut Temel ÖZDEMİR, Fırat University
Mansour MOSALLANEZHAD, Shiraz University
Mediha İPEK, Sakarya University
Mehmet Ali ERTÜRK, Fırat University
Mehmet ALTUNBEY, Fırat University
Mehmet ARSLAN, Karadeniz Technical University
Mehmet CEBECİ, Fırat University
Mehmet DAŞ, Fırat University
Mehmet DURANAY, Fırat University
Mehmet EROĞLU, Fırat University
Mehmet KALENDER, Fırat University
Mehmet KARAKÖSE, Fırat University
Mehmet KARATAŞ, Fırat University
Mehmet KAYA, Fırat University

Mehmet KÖKÜM, Fırat University

Mehmet ÖZDEMİR, Fırat University

Mehmet POLAT, Fırat University

Mehmet Sait SÖYLEMEZ, Gaziantep University

Mehmet Sinan BİLGİLİ, Yıldız Technical University

Mehmet ŞAHİN, Fırat University

Mehmet YILMAZ, Fırat University

Mehtap MURATOĞLU, Fırat University

Mehtap ÜLKER, Fırat University

Melahat BEYARSLAN, Fırat University

Melek Ural, Fırat University

Melek YILGIN, Fırat University

Melike AVER, Fırat University

Melike ESEN GÜNGÖR, Fırat University

Meltem ÇAKMAK KALKAN, Fırat University

Meral ÖZEL, Fırat University

Merve YILDIRIM, Fırat University

Mesut GÖR, Fırat University

Mete KALYONCU, Konya Technical University

Mete Onur KAMAN, Fırat University

Metin GÜRÜ, Gazi University

Mevlüt ALATAŞ, Munzur University

Miray Çelikbilek ERSUNDU, Yıldız Technical University

Mohammed Abdullahi Mu'azu, University of Hafr Al-Batin

Muammer TÜRKOĞLU, Samsun University

Muhammad Masood RAFIi NED University of Engineering and Technology

Muhammed ATAR, Fırat University

Muhammed Emre ÇOLAK, Fırat University

Muhammed Fatih TALU, İnönü University

Muhammed Furkan KÜÇÜK, Fırat University

Muhammed Sefa ÇETİN, Fırat University

Muhammed TALO, Fırat University

Muhammed ULUCAN, Fırat University

Muhammed YILDIRIM, Malatya Turgut Özal University

Muhammet AYDIN, Fırat University

Muhammet KARATON, Fırat University
Muharrem AKGÜL, Balıkesir University
Muhsin Tunay GENÇOĞLU, Fırat University
Mukaddes KARATAŞ, Fırat University
Murat BAYDOĞAN, İstanbul Technical University
Murat DOĞAN, Gazi University
Murat ELİBOL, Ege University
Murat KARACASU, Eskisehir Osmangazi University
Murat ŞEN, Fırat University
Murat Yavuz SOLMAZ, Fırat University
Musa ÇIBUK, Bitlis Eren University
Musa YETKİN, Fırat University
Musharraf ZAMAN, University of Oklahoma
Mustafa BOYRAZLI, Fırat University
Mustafa Can BİNGÖL, Burdur Mehmet Akif Ersoy University
Mustafa Eren RİZELİ, Fırat University
Mustafa GÜR, Fırat University
Mustafa İNALLI, Fırat University
Mustafa KANIK, Fırat University
Mustafa KAPTANOĞLU, Fırat University
Mustafa Selman AYDOĞAN, Balıkesir University
Mustafa TUNCER, Kütahya Dumlupınar University
Mustafa TUNÇ, Fırat University
Mustafa TÜRK, Fırat University
Mustafa ULAŞ, Fırat University
Müslüm ARKAN, İnönü University
Müslün Sara TUNÇ, Fırat University
Namık AYSAL, İstanbul University
Necip ÜNLÜ, İstanbul Technical University
Neslihan DURANAY, Fırat University
Neslihan DURMUŞ, Fırat University
Nevin ÇELİK, Fırat University
Nevin KONAKÇI, Fırat University
Nicola TARQUE, Pontifical Catholic University of Peru
Nigar ÖZBEY, Fırat University

Nihat KAYA, Fırat University

Nihat TOSUN, Fırat University

Nilüfer KOÇER, Fırat University

Niyazi Furkan BAR, Fırat University

Nizamettin ÖZDOĞAN, Zonguldak Bülent Ecevit University

Nuno MENDES, University of Minho

Nurhan ARSLAN, Fırat University

Oğuz YAKUT, Fırat University

Oğuzhan HASANÇEBİ, Middle East Technical University

Onur ALKAÇ, Fırat University

Onuralp YÜCEL, İstanbul Technical University

Orhan ÇAKAR, Fırat University

Osman YİĞİD, Fırat University

Ozan İNCE, Fırat University

Ö. Faruk DURSUN, İnönü University

Ömer ARAL, Ankara Yıldırım Beyazıt University

Ömer Faruk OSMANLI, Fırat University

Ömer Faruk TAŞ, Fırat University

Ömer GÜLER, Munzur University

Ömer Sinan ŞAHİN, Konya Technical University

Ömer ŞAHİN, İstanbul Technical University

Ömer Yavuz BOZKURT, Gaziantep University

Özge Erdoğan YAMAÇ, Fırat University

Özge HANAY, Fırat University

Özgür AVŞAR, Eskişehir Technical University

Özgür KARADUMAN, Fırat University

Özgür YILDIZ, Malatya Turgut Özal University

Özkan ÖZDEMİR, Sakarya University of Applied Sciences

Özlem Öztekin OKAN, Fırat University

Özlem TEPE, Fırat University

Paki TURGUT, İnönü University

Pranshoo SOLANKI, Illinois State University

Ragıp İNCE, Fırat University

Ramazan ORHAN, Fırat University

Recep ARTIR, Marmara University

Remzi TÜNTAŞ, Van Yüzüncü Yıl University
Rouzbeh GHABCHI, South Dakota State University
S. Emre KARA, Fırat University
Saadettin KAPUCU, Gaziantep University
Said ERAY, Sivas Technical University
Salih AYDOĞAN, Konya Technical University
Sanjay MISRA, Atılım University
Seda ARSLAN TUNCER, Fırat University
Sedat SAVAŞ, Fırat University
Selçuk ALEMDAĞ, Gümüşhane University
Selçuk KARATAŞ, Fırat University
Selen GÜRBÜZ, Fırat University
Sencer ÜNAL, Fırat University
Serap Çolak EROL, Fırat University
Serdar Ethem HAMAMCI, İnönü University
Serkan ERDEM, Fırat University
Servet SOYGÜDER, Ankara Yıldırım Beyazıt University
Seval GÜLER, Munzur University
Sevcan KÜRÜM, Fırat University
Sibel ASLAN, Fırat University
Sibel KAYGILI, Fırat University
Sinan KAPAN, Fırat University
Sinem AKYOL, Fırat University
Soheil GHAREH, Payame Noor University
Şaban TANYILDIZI, Fırat University
Şeyda ÖZDEMİR, Fırat University
Şeyda TAŞAR, Fırat University
Şule KAYA, Fırat University
Taha TAŞKIRAN, Ankara Yıldırım Beyazıt University
Tahsin BOYRAZ, Sivas Cumhuriyet University
Taner ALATAŞ, Fırat University
Taner TUNCER, Fırat University
Taylan SANÇAR, Munzur University
Tevfik YİĞİT, Fırat University
Turgay KAYA, Fırat University

Tülay YILDIRIM, Yıldız Technical University
Utku KÖSE, Süleyman Demirel University
Vedat ÇELİK, Fırat University
Vedat TANYILDIZI, Fırat University
Venhar ÇELİK, Fırat University
Veyis SELEN, Fırat University
Yakup DEMİR, Fırat University
Yasemin Didem AKTAŞ, University College London
Yasemin TOPÇUOĞLU,i Fırat University
Yaşar NUHOĞLU, Yıldız Technical University
Yavuz EROL, Fırat University
Yılmaz AYDIN, Fırat University
Yılmaz YILDIRIM, Zonguldak Bülent Ecevit University
Yunus AKSOY, Fırat University
Yunus Emre BENKLİ, Atatürk University
Yusuf CALAYIR, Fırat University
Yusuf DONAT, Fırat University
Yusuf KARGINOĞLU, Fırat University
Z. Fuat TOPRAK, Dicle University
Zeki ÇİZMECİOĞLU, İstanbul Ticaret University
Zülfü Çınar ULUCAN, Fırat University
Zülfü GÜROCAK,i Fırat University
Zümriye AKSU, Hacettepe University

Session Chairmans

Bedri ÖZER

H. Soner ALTUNDOĞAN

Muhammet KARATON

İhsan DAĞTEKİN

M. Emin EMİROĞLU

Oğuz YAKUT

Güngör YILDIRIM

M. Temel ÖZDEMİR

Zülfü GÜROCAK

Bilal ALATAŞ

Nevin ÇELİK

Akın ODABAŞI

Murat KARACASU

M. Yavuz SOLMAZ

Leyla KALENDER

Mehmet EROĞLU

Ayşegül UÇAR

Ahmet ÇINAR

M. Onur KAMAN

Özge HANAY

Erkut SAYIN

Filiz KAR

Ragıp İNCE

Cevdet AKOSMAN

Nihat TOSUN

Barış KARAKAYA

Mustafa KANIK

Murat ŞEN

Mustafa ULAŞ

Fatih ÖZYURT

INTRODUCTION

Dear Distinguished Delegate,

The second edition of the International Conference on Advances and Innovations in Engineering (ICAIE) was held between 21-23 September 2023 at Fırat University Faculty of Engineering, Elazığ.

International Conference on Advances and Innovations in Engineering is an international scientific forum of distinguished scholars engaged in scientific, engineering and technological research, dedicated to the furtherance of science, engineering and technology. The academic research conference since its inception is at the cutting edge of international nonprofit scientific, engineering and technological progress to promoting excellence in science.

The conference plays an influential role in science and promotes developments in science, engineering and technology in a wide range of ways. The conference aims to foster research in the area of science and technology and its impact to mainstream human activities. Specifically, it serves as a venue for discussions and exchange of ideas in current issues in science and technology.

All full paper and abstract submissions to the conference are peer reviewed and refereed and evaluated based on originality, research content and correctness, relevance to contributions, and readability. In this content the full paper and abstract submissions are chosen based on technical merit, interest, applicability and how well they fit a coherent and balanced technical program. The accepted papers after rigorous peer reviewing process have been published in the refereed international conference proceedings

Chair of ICAIE Committee
Prof. Ebru AKPINAR

CONTENTS

International Conference on Advances and Innovations in Engineering

International Conference on Advances and Innovations in Engineering
2ICAIE

Green synthesis zinc oxide and iron oxide nanoparticles using different plant extracts, and evaluation of their antimicrobial activities

İlkay ÜNAL[1], BURCU AYDOGDU[2], Mehmet AYTAR[3]

[1]Department of Gastronomy and Culinary Arts, Faculty of Fine Arts, Design and Architecture Education, Munzur University, Tunceli, Turkey,
[2]Department of Mechanical Engineering, Faculty of Engineering, Munzur University.Tunceli, Turkey
[3]Department of Biology, Graduate School of Natural and Applied Sciences, Adnan Menderes University, Aydin, Turkey

Abstract

Indrtoduction:

In this study, Zinc oxide (ZnO) nanoparticles and magnetite (Fe3O4) nanoparticles were synthesized using a precipitation approach with plant extracts of Ocimum basilica(1), Cinnamomum zeylanicum(2), Lactarius salmonicolor(3) and Paeonia kesrouanensis(4) as reduction/stabilizers. It is important to note that the properties and characteristics of nanoparticles synthesized with plant extracts may vary depending on plant species, extract composition, synthesis conditions, and purification methods. Therefore, the effects of different plant extracts on nanoparticle formation and antibacterial activities were investigated in this study MATERIALS-METHODS: Synthesis of ZnONPs; The zinc acetate solution was prepared in a hawk tube and kept in a water bath at 50 °C. Then 25 mL of plant extract was added. The pH was adjusted with KOH. After this time, the solution was centrifuged, washed and dried in an oven at 40 °C for 24 hours.Synthesis of Fe3O4NPs; FeCl2 and FeCl3 solutions were prepared in Falcon tubes and kept in a water bath at 70 °C, then the FeCl2 and FeCl3 solutions were mixed. Then 25 ml of plant extract was added, and the pH was adjusted with NaOH. At the end of this period, the solution was centrifuged, washed and dried in an oven at 40 °C for 24 hours. (ZnO, Fe3O4) were investigated by X-ray diffraction (XRD), transmission electron microscopy (TEM), Dynamic light scattering (DLS) and Fourier Transform Infrared (FTIR). The shape and morphology of green synthesized ZnO NPs and Fe3O4NPs were evaluated by TEM analysis. The agar well diffusion method was used to examine the antimicrobial activity of ZnO and Fe3O4 nanoparticules against gram-negative Escherichia coli (E. coli, ATCC 25922), Pseudomonas aeroginosa (P. aeroginosa, PAO1), gram-positive Staphylococcus aureus (S. aureus, ATCC 25923) and Candida albicans (C.albicans 90028) fungus at different concentrations (5, and 10 mg/mL).Results and CONCLUSIONS: According to the TEM image, the ZnONPs showed a flower-like structure cluster, while the Fe3O4NPs had a spherical shape with different size distributions. Among the synthesized NPs, ZnONPs-4 showed a smaller distribution, while Fe3O4NPs-3 had a uniform and single-crystal. The size and shape of the NPs can be controlled according to experimental conditions, such as ratios of reactants, reducing/stabilizing agents, temperature, and time [2]. ZnONPs and Fe3O4NPs have different shapes: rod-like, star-like, special, flower-like, cubes, triangles, tetrapod's, and isometric. NP shapes are one of the most important factors influencing their application areas. While ZnONP-3 and ZnONP-4 with low PDI values showed a more homogeneous distribution, all Fe3O4NPs with high PDI values showed a heterogeneous size distribution. The zeta potential values of the NPs differed according to the type of plant extract. While this value was between -5.35 and -16.9 for ZnONPs, it varied between -7.43 and -20.7 for Fe3O4NPs Nanoparticles synthesized with Cinnamomum zeylanicum extract showed very different results for zeta potential, -5.35±0.49 for ZnONP and -20.7±3.5 for Fe3O4NP. This result showed that Cinnamomum zeylanicum extract is more suitable for preventing nanoparticle aggregation by facilitating the absorption of positively charged metal ions in the synthesis of Fe3O4NP. Likewise, the zeta potential of ZnONPs nanoparticles synthesized with Ocimum basilicum extract was -16.9±3.71, which was the highest stability value, and it was the most suitable plant extract for synthesizing ZnONPs among these four different plant extracts. X-ray powder diffraction (XRD) patterns of the nanoparticle powder samples were taken to determine the crystal structures of magnetite nanoparticles synthesized from four different plant extracts, whether the Fe3O4 phase was formed, and to calculate the average crystal sizes. The characteristic peaks and 2θ values observed in the XRD curves confirm that the obtained particles are in the pure Fe3O4 phase. Likewise, X-ray powder

---

[1] Corresponding author

diffraction (XRD) patterns of nanoparticle powder samples were taken to calculate the average crystal sizes of the crystal structures of ZnONPs nanoparticles. The characteristic peaks and 2θ values observed in the XRD curves indicate that the obtained ZnONPs nanoparticles are identical to the hexagonal phase of zinc oxide. ZnO nanoparticles exhibited antimicrobial activity against the S. aureus strain alone. However, the Fe2O3NPs did not show any antibacterial effects against any strain. It was seen that the use of particles could become more efficient by choosing the synthesized nanoparticles according to the purpose of use.

Keywords: Zinc oxide, magnetite, green synthesis, nanoparticles, antimicrobial activity

Utilization an effective nanostructure for doxorubicin release

Burcu AYDOGDU[1], İlkay ÜNAL[2], Muharrem INCE[3], Olcay Kaplan İNCE[2]

[1]Department of Mechanical Engineering, Faculty of Engineering, Munzur University, Tunceli, Türkiye
[2]Department of Gastronomy and Culinary Arts,Faculty of Fine Arts, Design and Architecture, Munzur University Tunceli, Türkiye
[3]Department of Chemical Technologies,Graduate Education Institute Munzur University, Tunceli, Türkiye

Abstract

Introduction

Carbon nanotubes, one of the most widely used nanostructures produced by nanotechnology, have many physical and chemical advantages as high flexibility, electrical conductivity, and thermal conductivity. Because of these properties, it is frequently used in many industries. Aggregation of carbon nanotubes is one of the difficulties in their use. However, this disadvantage can be eliminated by linking functional groups to the ends of the chains and functionalizing them. Recently, its use in drug release studies has come to the fore. Especially in cancer types such as blood cancer, lung cancer, and breast cancer, controlled drug release, that is, smart drugs are produced, thus increasing the effectiveness of the drug and reducing its side effects. For this purpose, carbon nanotubes and various nanoparticles as cobalt ferrite ($CoFe_2O_4$), platinum (Pt), gold (Au), and silver (Ag) nanoparticles combined with carbon nanotubes are used to increase their efficiency. In this study, silver nanoparticles (AgNP) with antibacterial properties were supported on multiwalled carbon nanotubes and loaded with doxorubicin (DXR) that used in cancer treatment. Than the DXR release was investigated in simulated body fluids.

Material and method

At the functionilization step of pristine multiwalled carbon nanotubes (MWCNT); 25 mL, 4 mol L-1 of HNO3 and 75 mL, 10 mol L-1 of HCl were mixed and then this solution was added to 0.5 g of pristine MWCNT. This mixture was stirred at room temperature for a day. Then sonicated for 90 min using an ultrasonic bath. At the end of this period, MWCNTs were removed from the solution by filtering with filter paper, washed using ultrapure water and dried in an oven (120 °C and 24 hours).

At the supporting MWCNT with AgNP step (MWCNT@AgNP); 0.05 mol L-1 of AgNO3 was added to functionalized MWCNT and sonicated. Then ethanol/water extract of Marrubium astracanicum plant was put in it and stirred for 24 hours. In the last stage the mixture was filtered, washed and dried in an oven. The functionalized MWCNT and MWCNT@AgNP characterization analysis were done by X ray diffraction (XRD) spectrophotometer, Fourier transform infrared (FTIR) spectrometer with attenuated total reflectance (ATR), and transmission electron microscopy (TEM).

At the loading on functionalized MWCNT supported with Ag+ step; at different concentrations from 150 ppm to 300 ppm DXR was added to at certain amounts of MWCNT@AgNP and stirred for 24 hours. Then DXR loaded MWCNT@AgNP was separated from the solution by centrifugation and dried.

At the release study; simulated body fluid at pH 5.0 and pH 7.4 was prepared and DXR loaded MWCNT@AgNP was put into these solutions. At certain times 1 mL of solution was taken and analyzed by using UV-Vis spectrophotometer and the cumulative DXR release percentage was calculated. Considering the cumulative release percentage, it was determined that the release occurred rapidly up to the 250th minute at pH 5.0 and pH 7.4, after that the release rate slowed down as the time.

---

[1] Corresponding author

Results

For characterization XRD analyses were done at room temperature in the range of 20º-90º. In the XRD pattern of functionalized MWCNT 26º, 42º, 44º, 50º, and 54º and in the XRD pattern of MWCNT@AgNP 26º, 38º, 44º, 64º, 77º and 81º crystallographic planes can be seen. The FTIR spectra of functionalized MWCNT and MWCNT@AgNP were found different from each other. The band at 860 cm-1 was the Ag-O streching bond was determined in FTIR spectrum of MWCNT@AgNP. In the TEM images, it was seen that the MWCNT were successfully supported with AgNP.

Thermogravimetric analysis (TGA) was done from 25 °C to 800 °C, under air flow at a rate of 10 mL min-1. According the results of TGA, it was determined that the decomposition temperature of MWCNT@AgNP was lower than the decomposition temperature of MWCNT. The presence of AgNP in the structure reduces the thermal stability of MWCNT.

Release experiments of DXR loaded on MWCNT@AgNP at different concentrations were performed at two different pH and the data obtained were compared. Consistent with the data in the literature, it was found that the DXR release at pH 5.0 was higher than the release at pH 7.4. It should be noted that the cumulative DXR release also reaches approximately 30% at pH 5.0. Due to the tumour's acidic environment, drug release occurs in an acidic environment

As a result, it is thought that MWCNT@AgNP has good DXR loading and release data, so it can be used in smart drug applications. The used nanocarrier system, MWCNT@AgNP, also provides a great advantage in terms of being non-toxic and antibacterial.

Keywords: doxorubicin, characterization techniques, cumulative release, cancer

The match usıng of geomorphologıcal unıts for urban resistant agaınst dısaster

Murat SUNKAR[1], İlhan Oğuz AKDEMİR[2]

Department of Geography, Faculty of humanities and social sciences, Fırat University, Elazığ, Türkiye.

Abstract

The energy released during the breaking of the earth's crust spreads in the form of seismic waves, creating strong ground shaking. During periods of strong tremors, most of the non-resilient structures are severely damaged and destroyed. With this destruction, the earthquake turns into a disaster by causing great loss of life and property. In the transformation of an earthquake into a disaster, the magnitude of the earthquake, soil and geomorphological features, construction material and construction style are effective. On the basis of the problems experienced in today's cities; In addition to population growth, urban planning defects that do not comply with local principles and decisions, unconscious and methodless selection of settlements take the first place. The study is based on empirical examples in order to understand analytically the relationship between geomorphological units and earthquake disaster with a reductionist approach.

Lithological and tectonic characters are effective in the development of geomorphological units, which are also defined as landforms. Accordingly, there are direct/indirect correlations between geomorphological units and earthquake disaster. Because of this relationship, geomorphological characters should be analyzed along with proximity to the fault and soil properties in determining the settlement areas. With a more assertive approach, sometimes only the analysis of geomorphological characters may be sufficient to understand the earthquake resistance of the settlement area. When geomorphological and geomorphogenic studies and analyzes are made for a newly established settlement area, it will contribute to the easy determination of more resistant areas by reducing the costs in the very costly studies known as ground survey. In this context, when the plain floors, accumulation cones and fans consisting of loose fillings, and landslide areas are correctly determined; Without the need for extra budgets for ground survey, it will be possible to direct the settlement to more resistant areas. Most of the time, since the boundaries of plains, accumulation cones and fans and landslide areas are not determined correctly, settlements in related areas are less resistant to earthquakes. In addition:

Appropriate site selection parallel to geomorphological units,

- Distance from the benefit and location and application of fault containment bands (fault buffers),
- Location analyzes suitable for street and street systems,
- Settlement location suggestions for housing pattern and population density,
- Detection of hydro-geomorphological risky areas,

Many similar topics can be solved with the principles of applied geomorphology and terrestrial view. Apart from general geomorphological features, each geomorphological unit should be analyzed separately. For example, in the use of a ridge, the surface of the ridge and the use of slopes do not show the same resistance. As a matter of fact, the fact that the earthquake caused different damage in different locations within the same settlement in the 6 February 2023 Kahramanmaraş earthquakes showed that it was due to the characteristics of the geomorphological unit in which the settlement was established. Since it is possible to establish settlements with high resistance to earthquakes with the correct classification of geomorphological units, it is thought that geomorphological analyzes will provide great advantages in determining settlement areas.

Keywords: Geomorphology, earthquake, disaster, resilience

---

[1] Corresponding author

AI Approach for Postural Assessment

Tolga GÜZEL[1], Metehan ÇAM[2], Faruk DİRİSAĞLIK[3]

[1,2,3]Department OF Electrical and Electronics Engineering, Eskisehir Osmangazi University, Eskisehir, Turkey.

Abstract

Posture refers to the balanced positioning of the body achieved through coordinated movements while engaging in various activities such as sitting, lying down, standing, or walking. Posture disorder is characterized by the abnormal positioning of the spine, leading to stressful postures of the joints, muscles, and vertebrae. This disorder can arise from factors such as previous accidents or impacts, a sedentary lifestyle, muscle weakness, poor physical condition, improper sitting or lying habits, excessive weight, pregnancy, imbalanced load distribution, chronic slumped shoulders due to neurological and muscular factors and genetic factors. Prolonged poor body positioning can lead to deterioration in the musculoskeletal system, compression of tissues, organ dysfunction, and pain in the joints, head, waist, neck, and back, and extreme fatigue. Furthermore, it can adversely affect person's physical appearance and mental well-being, significantly impact their overall quality of life.

Postural disorders are categorized into three types: scoliosis, kyphosis, and lordosis. Scoliosis is a lateral curvature of the spine observed in the thoracic or lumbar regions. Kyphosis, also known as humpback, results from an excessive forward bending of the spine. Lordosis refers to an inward curvature of the spine, especially in the waist area, that exceeds normal parameters. Given the increasing prevalence of postural disorders, early detection becomes crucial. Ignoring posture disorders or delaying treatment can lead to rapid progression in disease. In severe cases of postural disorders, surgical operation may become necessary. While visual observation, physical examination and photogrammetric methods which are practical and accessible diagnosis techniques can only provide a general assessment of these disorders, more advanced techniques like radiography, electromagnetic-based solutions, and 3D analysis systems exist. However, these methods are less accessible, requiring laboratory environment, expensive, and may carry potential risks. Thanks to current technology, early diagnosis of these disorders is now achievable through user-friendly applications, real-time deep learning techniques, and wearable technological devices.

This study aims to develop a user-friendly mobile application to enable individuals to self-assess their own posture, emphasizing the importance of early detection in postural disorders. The mobile application utilizes photographs taken from various perspectives to detect postural disorders, employing contemporary image processing techniques for analysis. Additionally, a wearable device equipped with sensors has been developed to prevent disease progression in users with early or moderate postural disorders. This device collects real-time data on the user's posture and provides audible and vibrating alerts if prolonged poor posture is detected, encouraging the user to adjust their positioning. In the developed mobile application, a web server was implemented using Flask in Python, enabling communication with Flutter through an Internet Protocol (IP). The user's photographs, captured from three different perspectives (right, left, and front), are simultaneously processed by the PoseNet model to identify the coordinates of key points in the human body. To assess posture disorders, six key points are

---

[1] Corresponding author

identified in the front photograph, while three key points are marked in both the right and left photographs. The coordinates of these marked key points, along with the angular variations between them, are compared with the predefined threshold values. Based on this comparison, the user is informed about the type and its severity level of the disorder. Furthermore, recommendations are provided to aid in the posture adjustment process. To assist in monitoring patient posture, a wearable device has been developed. This device consists of an STM32F407 microcontroller, an MPU6050 which is a sensor for motion processing device, and audible and vibrating devices. The microcontroller continuously monitors filtered acceleration and gyroscope data from the MPU6050, which is then converted into angular data using Euler formulas, used to describe rotations in three-dimensional space. By comparing these angular values against predefined ranges, the device gives audible and vibrating warning to the users if body position stays long exceeded of these ranges, thereby promoting users to adjust their body position.

As a result, the scoliosis detection rate in the conducted tests, involving sample photographs with and without posture disorders, was found to be 93%. The kyphosis detection rate was 89%, while the lordosis detection rate reached 68%. The success rate of detection varies depending on the severity level of the disorder, with higher success rates observed in severe stages of posture disorders compared to early and moderate stages. Additionally, the success rate is affected by photo quality and the angle of the photographs captured. However, the study concludes that such an approach including software and hardware implementation can be utilized for the early diagnosis of postural disorders and their treatment if the case is not severe.

Keywords: Kyphosis, Lordosis, Postural assessment, Posture disorders, Scoliosis

Determination of natural gamma radioactivity levels in grape, chard, and parsley samples collected from Rize and its districts

Esra Yılmaz BAYRAK[1]

[1]Gümüşhane University, Gumushane, Turkey

Abstract

Introduction

Humans and other living organisms are constantly exposed to a radiation environment throughout their lifetimes, which includes cosmic radiation from space and natural radioactive elements such as U-238, Th-232, Cs-137, K-40 and originating from the Earth's crust. It is well-known that a significant portion of gamma radiation originates from the surface layer, particularly within the 0-25 cm depth. Over the past century, this natural level has seen a considerable increase due to nuclear bomb testing and the use of certain technological products.

Natural and artificial radionuclides found in food and beverages are known to contribute to an effective internal dose when consumed. According to an estimate, food consumption accounts for a sizable portion of the mean yearly effective dosage resulting from natural sources. The dosage generated by consuming food products can be estimated by measuring the radionuclide concentrations that are present in foods. This kind of activity also enables the establishment of baseline values for comparison with subsequent measurements.

Rize province has been subjected to investigation due to its geographical location and contamination with radiation following the Chernobyl nuclear power plant accident. This study aims to assess the radiation levels in vegetables and fruits grown in Rize and compare the calculated effective annual dose with internationally permitted levels for health assessment.
In this study, gamma radioactivity levels of grapes from Pazar, Derepazarı, and Ardeşen; Swiss chard from Pazar, Derepazarı, and Fındıklı; and parsley from Ardeşen, Derepazarı, and Fındıklı were determined.

Metarials and Methods

Three sampling stations were selected in each region. Subsequently, samples of grapes, Swiss chard, and parsley were collected. The collected samples were placed inside aluminum foils and incinerated at 600°C in a muffle furnace for a duration of 10 hours to turn them into ash. The weight of the obtained ash from each sample was measured, and they were then transferred and labeled in plastic sample containers. The containers were sealed with tape and left undisturbed for 21 days to establish radioactive equilibrium. Subsequently, gamma spectrometric analysis was performed on the samples, and counting values were recorded at predetermined intervals.
Using a coaxial HPGe detector with a 55% relative efficiency and 1.9 keV accuracy 1332 keV gamma radiation at the Co-60, gamma spectrometry measurements were performed on all samples (Ortec, GEM55P4-95 model). The device was protected by a lead well that was 10 centimeters thick and had 2 mm Cu foils inside of it. The computer program Genie 2000, which was purchased from CANBERRA, was used to conduct the spectrum study.

The U-238 series is characterized by gamma energy levels of 351.9 keV (Pb-214) and 609.3 keV (Bi-214), while the Th-238 series is represented by energy levels of 911.1 keV (Ac-228)

---

[1] Corresponding author

and 583.1 keV (Tl-208). Applying gamma lines at 1460.8 keV, K-40 was studied. The following equation was used to calculate the activity values of the U-238, Th-232, Cs-137, K-40 in the analyzed samples:

$A=s/[(I\gamma).w.t.\varepsilon]$

Where, A (Bq/kg) is the activity, s is the net field of the total absorption line, $I\gamma$ is the absolute intensity of the transition, w is the mass of the sample, t is the sample measurement period and ε is the full energy peak capacity.

After counting the samples in the HPGe detector, the activity concentrations of radionuclides (U-238, Th-232, Cs-137, K-40) were calculated in Bq kg^{-1} units for each sample. Additionally, effective annual dose were calculated in µSv $year^{-1}$ units.

Result and Conclusions

The calculated results for grapes showed concentrations of U-238, Th-232, Cs-137, K-40 as (4.10±0.37), (3.16±0.41), (1.75±0.18), and (272.15±7.63) Bq kg^{-1}, respectively. Swiss chard exhibited concentrations of U-238, Th-232, Cs-137, K-40 as (28.63±2.50), (14.58±1.49), (22.13±2.18), and (840.18±28.13) Bq kg^{-1}, respectively. For parsley, the concentrations were (53.39±4.20) Bq kg^{-1} for U-238, (20.67±6.09) Bq kg^{-1} for Th-232, and (B.D.L.) for Cs-137, and (1134.59±50.04) Bq kg^{-1} for K-40. The calculated effective annual dose for grapes, Swiss chard, and parsley were 0.765, 0.239, and 0.448 µSv $year^{-1}$, respectively.

When comparing the obtained data, the highest concentration of U-238 was found in parsley (53.39±4.20) Bq kg^{-1}, and the lowest in grapes (4.10±0.37) Bq kg^{-1}. For Th-232, the highest concentration was detected in parsley (20.67±6.09) Bq kg^{-1}, while the lowest was in grapes (3.16±0.41) Bq kg^{-1}. The highest concentration of Cs-137 was observed in Swiss chard (22.13±2.18) Bq kg^{-1}, whereas it was below the detection limit (B.D.L.) in parsley. For K-40, the highest concentration was recorded in parsley (1134.59±50.04) Bq kg^{-1}, and the lowest in grapes (272.15±7.63) Bq kg^{-1}. The highest effective annual dose was found in grapes, and the lowest in Swiss chard.

The World Health Organization's established effective annual dose (H) is 290 µSv $year^{-1}$, and the permissible Cs-137 value is 1000 Bq kg^{-1}. Based on this research, the levels of Cs-137 and dose values were found to be significantly lower in these food items, indicating no health risks for consumers.

Keywords: Radioactivite, foodstuff, effective annual dose, health risks.

The relationship between the dynamic elasticity modulus of a series of concrete specimens calculated by international regulations and the compressive strength

Esra TUGRUL TUNC[1]

[1]Department of Civil Engineering, Faculty of Engineering, Fırat University, Elazığ, Turkey.

Abstract

Introduction

Concrete is an important building material that is formed as a result of mixing granular materials such as sand, gravel and crushed stone called aggregates with cement and water that bind them. Cement acts as a binder in the mixture. Fine aggregate fills the gaps between coarse aggregate grains and increases the compatibility of concrete. Gravel or crushed stone grains form a kind of skeleton of the concrete. Thus, they resist possible forces. Concrete is a load-bearing building material. In the first stage of its production, concrete is a highly viscous liquid; it can be placed in molds of different shapes. This quality shows the superiority of concrete over natural stones, because natural stones are not used outside of certain geometric shapes without being processed or chiseled, they do not create a continuous bearing environment.

One of the most important mechanical properties of concrete is its compressive strength. Compressive strength of concrete is affected by many factors. Although the same aggregate and cement are used in concrete production and no change is made in production methods, the strengths of the concretes obtained can be different from each other. The main factors affecting the compressive strength of concrete can be listed as factors related to cement, amount of water, and compatibility of concrete.

Elastic deformation is the deformation in which a material can return to its original shape when the load is removed after being subjected to deformation under load. When the elastic limit is exceeded, most materials undergo plastic deformation that does not return to its initial shape. Elastic strain is proportional to stress in most building materials and varies linearly. Elastic strain is considered to be time independent. In the case of uniaxial loading, this relation is expressed as $\sigma=E\times\varepsilon$ (Hooke's Law) and constitutes the fundamental law of elasticity. The coefficient “E” in this relation is called the elasticity modulus of the material.

Knowing the elasticity modulus of concrete is important for calculating the deformations of concrete, reinforced concrete and prestressed concrete structures. Since these deformations must be known in many respects, the elasticity modulus is a mechanical property that must be determined. We can also calculate the stresses by measuring the deformations using the knowledge of the elasticity modulus. There is a relationship between elasticity modulus and compressive strength of concrete. With the equations derived from this relationship, it is possible to calculate the approximate elasticity modulus of concrete without destroying the concrete. The presence of a viscous phase such as cement paste in concrete causes the deformation of this material to be different from the deformation of solid objects.

Materials and Method

In the present study, limestone aggregate extracted from Elazığ province was used for the production of concrete specimens. Aggregate mixtures with the largest grain diameter of 31.5 mm were used in the calculation of concrete mix design according to TS 802.

---

[1]Corresponding author

CEM I 42.5 N Portland cement produced in Elazığ Cement Factory was used in the experimental studies. The present study was carried out at Fırat University, Faculty of Engineering, Department of Civil Engineering, Building Materials Laboratory (FÜYAMLAB).

The specimens were placed in a curing pool with a temperature of 23°C and removed from the pool at the end of the 28th day. Compressive strength tests were performed on 150x150x150 mm sized concrete cube specimens with dry surface in accordance with TS EN 12390-3 standard. The same compressive strength apparatus with constant loading rate was used for the crushing of the obtained concrete specimens.

Since it is difficult to determine the elasticity modulus from the σ - Ɛ relationship, the dynamic elasticity modulus of the concrete specimens manufactured in the present study was calculated using empirical formulas according to TS 500-2000 - ACI 318-95 and CEB-FIP 1978 based on the experimental data in this study.

Results

Within the scope of the present study, the compressive strengths of a total series of concrete specimens produced for different cement dosages (300, 350 and 400 kg/m3) using limestone aggregate were determined. Using these experimental compressive strength values, the dynamic elasticity modulus was calculated according to the relevant regulations TS 500-2000, ACI 318-95 and CEB-FIP 1978.

When the variation of the compressive strength of the concrete specimens tested within the scope of the present study was examined with the water cement ratio, it was determined that the compressive strength decreased by approximately 10% on average with an increase in the water cement ratio from 0.25 to 0.30. Dynamic elasticity modulus values was calculated in accordance with the calculations and rules in TS500 (2000) regulation. Accordingly, it was determined that there was approximately 20% increase in the dynamic elasticity modulus values in response to approximately two-fold increase in the compressive strength of concrete. Dynamic elasticity modulus values was calculated in accordance with the calculations and rules in ACI 318 (1995). Accordingly, it was determined that there was an increase of approximately 40% in the dynamic elasticity modulus values in response to approximately two-fold increase in concrete compressive strength. Dynamic elasticity modulus values was calculated in accordance with the calculations and rules in CEB-FIP (1978) regulation. Accordingly, it was determined that there was approximately 20% increase in the dynamic elasticity modulus values for approximately two times increase in concrete compressive strength.

Conclusions

As a result, it was determined that the dynamic elasticity modulus increased with the increase in concrete compressive strength. However, it was observed that the rate of increase in concrete compressive strength was higher than the rate of increase in dynamic elasticity modulus.

Keywords: Concrete specimens, Compressive strength, Dynamic elasticity modulus, Concrete quality.

Experimental investigation of the maximum scour depth downstream of a free-falling v-notch weirs

Mustafa TUNC[1], Muhammet Emin EMIROGLU[2]

[1,2]Department of Civil Engineering, Faculty of Engineering, Fırat University, Elazığ, Turkey.

Abstract

Introduction: It is obvious that the construction of any water structure on the rivers will disrupt the existing balance as there will be a change in the flow of the river. The restoration of this balance in the river is possible through the formation of scour and sediment deposits in places. In other words, since the natural flow of the river is blocked, local scouring may occur at the downstream base due to the potential energy accumulated by the flow. These local scour can increase over time and weaken the foundation of the water structure, causing damage or even collapse of the hydraulic structure in question. Depending on the river flow, the bottom material transported from the local scour pits will cause deposits on the river bed. These sediment deposits may also cause the structure to be inefficient. Because these ripples downstream of the dam directly affect the well water depth, the spillway and the power plant operation.

The aim of this study is to investigate experimentally the time variation of the maximum scour depth downstream of free-falling V-notch weirs. It was found that previous studies were generally carried out for small-scale laboratory models and for non-shrinkage weirs. In the present study, the scour in the downstream of a V-notch weir is investigated by considering different dimensionless parameters. Thus; it is aimed to provide useful findings to practical engineers and the literature.

Materials and Method: Within the scope of this study, local scour in the downstream of conventional V-notch weirs with shrinkage was investigated experimentally. Within the scope of this study, the existing experimental setup in the Hydraulics laboratory of the Department of Civil Engineering, Faculty of Engineering, Fırat University was used. In the experimental setup, the upstream channel length was taken as 6 m which is sufficient length to provide the developed flow condition. There are two tanks in the hydraulic laboratory. The tank located in the basement of the laboratory is 100 m^3. The tank approximately 11 m above this tank is 50 m^3. An overflow weir is placed on the tank on the upper floor to keep the water level static and to ensure the sump condition. Three 22 kW pumps were used to pump water from the tank below to the tank above. Each of the pumps can pump a flow rate of 77 L/s to the upper tank. Thus, the desired flow rates could be safely taken to the experimental setups with the help of valves on the main pipeline. In the experimental setup used in this study, a 45 kW pump was also installed to pump the water so that the desired flow rates could be easily obtained. The experimental setup was carefully constructed using sheet metal, glass, plexiglass, profile, chrome-nickel, sleeve, nipple, valves and other fittings. Then it was painted with special metal paint. Scaffolding stairs were built.

The existing experimental setup was manufactured to be adjustable for four head heights. The experiments were carried out for 9 hours for four head heights and four unit flows in a free fall V-notch weir. The upstream channel is 60 cm wide, 90 cm high and 6 m long. There is a reservoir and tranquilizers before the experimental channel. The downstream pool is 2 m wide, 2 m high and 2.5 m long. The downstream pool was filled with 1 m high bottom material (d_{50}=1.3 mm, quartz sand). The drop heights were 25, 50, 100 and 167 cm; the flow rates were 5, 8, 12 and 15 L/s and the tailwater depth was 25 cm.

---

[1] Corresponding author

Results

When the variation of the scour depth with time depending on the head and flow rate was analyzed; it was determined that the equilibrium scour depth increased as the flow rate increased. It can be said that the equilibrium scour depth generally decreases with the increase in the height of the drop.

When the jet trajectory is analyzed in V-notch weirs; the distance of the jet hitting the downstream pool increases with increasing flow rate. The distance between the exit point of the water jet and the point of impact on the downstream pool does not change significantly with increasing flow rate.

When the jet widths for the tested V-notch weir are analyzed; the jet width increases with the increase in flow rate and head height. As the jet width increases and the jet impact angle increases, more air bubbles are introduced into the downstream pool. Due to the shrinkage of the V-notch weir, the jet width increased with increasing head.

Conclusions

Jet trajectory, downstream scour geometry and bottom topography were determined for the free-falling V-notch weir flow.

- As the flow rate increased, the equilibrium scour depth also increased.
- In general, the equilibrium scour depth decreased with the increase in drop height.
- With the increase in flow rate, the distance of the jet hitting the downstream pool increases.
- The distance between the exit point of the water jet and the point of impact on the downstream pool does not change significantly with increasing flow rate.
- The sand pile formed in the downstream pond is spread in a crescent shape across the width of the scour chamber.

Keywords: Flow characteristics, Hydraulic structure, Local scour, Maximum scour depth, V-notch weir.

Acknowledgement
This study was supported by TUBITAK-1001 Project No. 115M478.

International Conference on Advances and
Innovations in Engineering

Effectiveness of drucker-prager material model for micro level analysis of the masonry walls

Ertuğrul ÇAMBAY[1],Muhammet KARATON[2]

[1,2]Civil Engineering Department, Bitlis Eren University, Bitlis, 23119, Turkey

Abstract

Graphical/Tabular Abstract

It is important research area that micro modelling of the masonry walls in terms of the understanding of the response of the structural elements. Masonry buildings are widely built in our country, especially in rural areas, as in many countries of the world, because they are economical and can be easily constructed with local materials. For this purpose, the brick/stone, which is the construction material of the building, and the mortar used to connect these elements should be modeled in detail and the wall strengths should be determined. This modeling technique is called "Micro modeling" and has been the field of study of many researchers. In this research, experimental results of the Eindhoven walls are used for appropriate equations for the Drucker-Prager material model. In the first loading phase, pre-loading were applied in vertical direction of the walls. After loading phase, displacement controlled loading were applied at top of the wall in horizontal direction. Pre-loading values which has 30 kN, 120 kN and 210 kN, were called as JD4, JD6 and JD7, respectively. The dimensions of the Eindhoven walls are 990×1000×100 mm and were built using 210×52×100 mm bricks and 16 rows of brick-mortar with a mortar thickness of 10 mm. The walls are 990x70x100 mm steel plates at the top and bottom of the model. In this model, a total of 11200 nodal points and 11096 plane solid finite elements are used. Base shear force-top displacement graphs were obtained and cracking regions under these loadings. Numerical results were calculated by using different brick and mortar material properties. Numerical analysis results were obtained with the help of Ansys finite element program. Appropriate equations for the Drucker-Prager material model is obtained by using maximum loading capacity, threshold displacement value and damage regions.

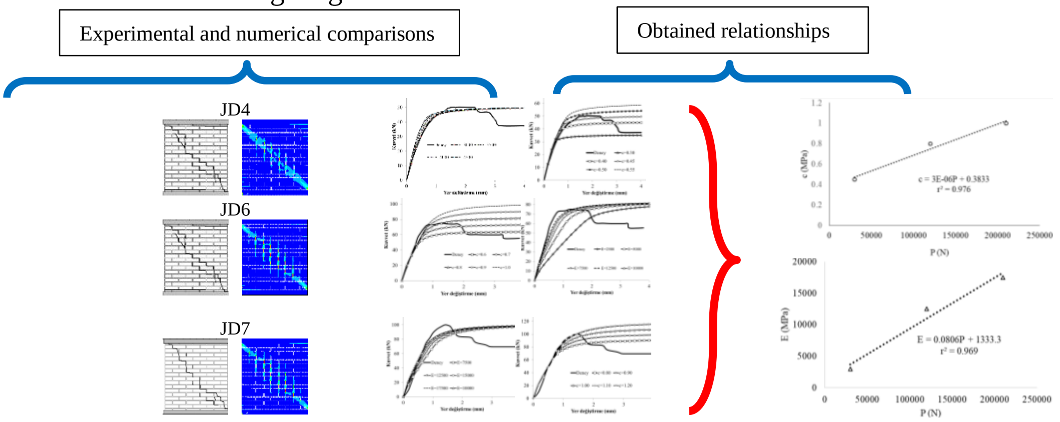

Purpose: In this study, the effectiveness of the Drucker-Prager material approach in analysis by the micro model of the masonry walls are investigated. Some equations for the material properties of the bricks are recommended in the numerical modelling of the walls.

Theory and Methods: The Drucker-Prager material model is widely used for numerical analysis of the brittle materials. This model is obtained by von Mises criteria which include hydrostatic stress. The model is used two material coefficient as cohesion and internal friction angle. Yield surface of the model is a right cone shape. Plastic strains which perpendicular to the surface, are occurred for principal stress outside of the yield surface.

---

[1] Corresponding author

Results: When comparing with experimental and numerical results with regard to maximum loading capacity, threshold displacement and total energy values of the JD4, JD6 and JD7 walls, the modulus of elasticity, the internal friction angle and the cohesion values of the brick unit. In the all solutions, the plastic strain regions were obtained as three regions. First region started from the upper right corner of the walls and it propagated to the left side in the horizontal direction. Second region started from the lower left corner of the walls and it propagated to the right side in the horizontal direction. Additional damage zone was obtained as diagonal form that propagated from the upper left corner to the lower right corner. In the all numerical solutions, no internal friction angle are affected. It is observed that cohesion and internal friction angle of the brick unit are varied that depending on the preloading values of the Eindhoven walls.

Conclusion: In all the numerical solutions, it is observed that although the cohesion and elasticity modulus material properties of the brick material are affected to numerical results, the internal friction angle of the brick material is not influenced. Thus, appropriate values for modulus of elasticity, internal friction coefficient and cohesion of brick material in the JD4, JD6, and JD7 Eindhoven walls, are determined by using comparisons to maximum load capacity, threshold displacement and total energy values obtained from experimental and numerical results. In this research, appropriate equations for the Drucker-Prager material model is obtained. It is determined that no numerical solutions are affected by material properties of the mortar. Modulus of the elasticity and cohesion values are varied that depending on the pre-loading values of the walls. Therefore, correlations between preloading-cohesion of the brick and pre-loading-the elasticity modulus of the brick are obtained as $c_T = 3\ 10^{-6}P + 0.3833$ and $E_T = 0.0806P + 1333.3$, respectively.

International Conference on Advances and
Innovations in Engineering

Development of an approach combining Bayesian network, stratified Best-Worst Method and TOPSIS Sort for occupational safety risk assessment and its application in a ready mixed concrete plant

Coskun KARCI[1] , Melih YUCESAN [2], Muhammet GUL [3]

[1]Department of Engineering Management, Munzur University, Tunceli, Turkey.
[2]Department of Emergency Aid and Disaster Management, Faculty of Health Sciences, Munzur University, Tunceli, Turkey.
[3]Faculty of Transportation and Logistics, Istanbul University, Istanbul, Turkey.

Abstract

Introduction: In the production industry, the suitability of the workplace environment, the quality of the production machinery/tools and the participation and adoption of the employees are important for the production activities to be carried out according to the principles of occupational health and safety (OHS). Therefore, occupational risk assessment is very important for manufacturing industries. When deciding on the prioritization of risks in occupational risk assessment, considering how the parameters defining the risk will change in different possible states (under different conditions that will arise in the future) strengthens the decision-making process. Therefore, the main motivation of this study is to develop a new occupational risk assessment approach that will address future changes in the importance levels of risk parameters and minimize the uncertainties that may arise in the risk assessment process.

Materials and Methods: To adapt this dynamic situation to the approach, stratified multi-criteria decision making (MCDM) has been preferred. The concept of stratification with the best-worst method (SBWM), which is an important MCDM method, is used to determine importance weights of the risk parameters of occupational risk assessment. In addition, Bayesian version of BWM has been used to bring together and evaluate the evaluations of more than one decision maker without loss of information. Unlike the literature, GeNle software, a Bayesian Network tool, was used to calculate the posterior probability values of the future states considered within the scope of the study. In determining the priority scores of each hazard, the TOPSIS Sort method, which works according to the logic of proximity to the ideal solution and has the purpose of classification, is used. Thus, while determining the priority score and order of each hazard, the class of this hazard can also be determined. In this context, each hazard has been assigned to five classes as “very high risk, high risk, substantial risk, possible risk, risk”.

Results: The study was applied to the analysis of risks in a ready-mixed concrete production facility located in Tunceli. Five different risk parameters were determined for the problem. These are probability, severity, detectability, cost, and feasibility of preventive measures. Classical methods, which are widely discussed in the literature and commonly used by SMEs in the manufacturing industry, usually contain two or three parameters. Seven different states affecting the importance weights of these parameters are discussed. These are respectively S1-Current state; S2-Changes in the technology, materials and equipment used in the workplace and in the production method; S3-Occurrence of work accident, occupational disease or near miss event; S4-The emergence of a danger (natural disaster, Covid-19 epidemic, etc.) originating from outside the workplace and affecting the workplace; S5-3. and simultaneous occurrence of the situations in item 4; S6-2. and simultaneous occurrence of the situations in item 4; and S7-All situations occur at the same time. To calculate the importance weights of the risk parameters, the transition probabilities of these seven states were calculated. Here, the network structure of the strata is created with the Bayesian network.

---

[1] Corresponding author

On the other hand, Bayesian BWM has been used in the pairwise comparison of risk parameters for each state by decision-making experts and merged with stratification. In this way, it is aimed to introduce an approach called stratified Bayesian BWM that can be used for further studies in the literature. According to the results obtained regarding the probabilities of the states, S2 has the highest transition probability with a probability value of 25%. This was followed by S3 (21%), S1 (16%), S6 (12%), S5 (9%), S7 (9%) and S4 (8%). The final importance weights of the five criteria were obtained by multiplying these posterior probability values with the criteria weight values (obtained from Bayesian BWM) under each state. According to these results, while the cost criterion is in the first place with 27% importance, it is followed by the applicability of preventive measures with 24% and detectability with 19%, respectively. The weight of probability and severity parameters, which are the two most important parameters of classical risk analysis methods, are in the last two places with 15% per each. According to TOPSIS Sort results, in the ready mixed concrete facility where the application is made, there are 2 hazards in the very high-risk class, 9 hazards in the high-risk class, 23 hazards in the substantial risk group, 8 hazards in the possible risk class and finally one in the risk class. It has been determined that the most prioritized and high risks are caused by accidents due to excessive speed and traffic accidents inside and outside the operation area due to the truck/construction machinery not complying with the speed limits. Following these, it was concluded that the hazards such as working at height, unsuitable lifeline, and improper cleaning activities in cement silos cause risks in the high-risk class.

Conclusions: OHS and the concept of occupational risk assessment, which is at the center of this concept, is a process that both concerns the life and health of employees and affects production costs, with the awareness it provides in reducing the negative effects of risks that arise in production facilities. With the new approach proposed in this study, a process that directly affects employee health in a positive sense was produced by reflecting the effect of possible future situations to the analysis. It has enabled a more effective risk assessment than traditional occupational risk assessment practices.

This study is part of a research project supported by Scientific and Technological Research Council of Türkiye (TUBİTAK) with the Grant No. 122M702 under 1002-Short Term R&d Funding Program. We thank TUBİTAK for is support

Keywords: Occupational risk assessment, Stratified Bayesian Best-worst method, multi-criteria decision making, TOPSIS sort, ready-mixed concrete production

International Conference on Advances and Innovations in Engineering

Shear strengthening of a steel bridge girder

Tuğçe Sevil YAMAN[1]

[1]Civil Engineering Department, Faculty of Engineering, Mersin University, Mersin, Türkiye.

Abstract

1. Introduction

Plate girders are designed to carry severe loads over large spans. Flanges resist moment and web stands shear forces. While designing plate girders different failure mechanisms, e.g. shear buckling, compression buckling, local buckling of the web, local buckling of the flanges, and lateral-torsional buckling of the girder are considered. Shear strength of steel girders with slender webs is far less than the yielding shear capacity, which generally controls the capacity of compact and non-compact webs of girders. It is primarily because of the web buckling before reaching the material's yield strength. Elastic buckling of the web is directly related to the web stress level caused by the principal compressive forces at the high shear regions of the girder. Reducing the stress level in the web occurring at the same load, could delay the elastic bucking occurrence, thus improving the shear capacity of the girder. Webs are usually reinforced with transverse stiffeners to enhance the buckling strength by decreasing panel aspect ratio. Stiffened webs stand shear also after buckling, which is named as post buckling strength [3].

2. Phases I and II

A comprehensive research program was realized as three phases to investigate the usage of carbon fiber reinforced polymer (CFRP) strands for uniaxial compressive and shear strengthening of steel plates and for shear strengthening of steel girders. In the first phase of the program, bond characteristics of the proposed material was evaluated. Afterwards in the second phase, the strengthening system's performance was tested in increasing the shear capacity of steel plates under pure shear stresses [1, 2].

3. Analysis and Stiffeners' Design

As the third phase of the research, the effectiveness of the strengthening system in increasing the shear capacity of a steel bridge girder was tested through 12 experiments. Before the tests, the design shear strength check, design flexural strength check, and the stiffeners' design of the steel girder specimen were performed by the author [3]. The steel girder was a built-up section. It was designed intentionally to fail in shear buckling. Analysis and stiffeners' design were realized according to the provisions for load and resistance factor design (LRFD) in the ANSI/American Institute of Steel Construction (AISC) 360-16 – Specification for Structural Steel Buildings [4].

4. Experimental Program

The steel girder web was stiffened and comprised six shear panel zones. Two panels at the girder ends were tested as controls and strengthened sections. The steel girder was simply supported and laterally braced. The loading was applied by hydraulic jacks located on a loading beam set on top of the girder. Experiments were conducted utilizing the remaining four steel web panels. Each panel was tested three times. The first test was a reference test, the second test was done by strengthening the panel with one layer of CFRP strands, and the third test was done by strengthening the panel with two layers of CFRP strands. High modulus CFRP strand was utilized in the experiments. Parameters used were orientation of CFRP and the number of CFRP layers.

---

[1] Corresponding author

5. Analytical Study

Phases of the research program concerning the usage of CFRP strands to increase the compressive and shear strength of steel plates showed that finite element models and simple hand calculations are sufficient to estimate the behavior and strength increase obtained by utilizing the strengthening system. The classical elastic relationship was utilized to determine the shear stress in the panel. CFRP compressive elastic modulus determined from the coupon tests was used in the calculations. In addition, Tresca criteria was used to find shear stress from steel normal stress and then to calculate the theoretical shear strength. The estimated shear strength was checked with the measured values for all tests. The comparison demonstrated that the shear load can be efficiently predicted from the composite transformed section properties of the strengthened panel [2].

6. Results and Conclusion

Results showed that the CFRP strands were very effective in increasing the shear strength before the steel web yielding. In addition, increasing the CFRP layers' number improved the shear capacity of the web regardless of the CFRP strand orientation. The system demonstrated no debonding of CFRP up to failure. The high modulus CFRP strand was found out to be an efficient material in enhancing the shear capacity of steel girders. The increase of the lateral stiffness was related to the increase in reinforcement ratio. Moreover, CFRP strands placed parallel to the compressive stress direction had the highest increase in lateral stiffness followed by CFRP strands oriented vertically. Increasing the CFRP reinforcement ratio increased the shear strength of the system. Slenderness ratio increase of the plates improved the effectiveness of the strengthening system. Furthermore, optimum orientation was obtained by installing the strands in the principal compressive stress direction.

Keywords: plate girder, shear buckling, strengthening, carbon fiber reinforced polymer

References

[1] Kazem H, Guaderrama L, Selim H, Rizkalla S, Kobayashi A. “Strengthening of steel plates subjected to uniaxial compression using small-diameter CFRP strands”. Construction and Building Materials, 111(2016), 223-236, 2016.
[2] Kazem H, Rizkalla S, Kobayashi A. “Shear strengthening of steel plates using small-diameter CFRP strands”. Composite Structures, 184(2018), 78-91, 2018.
[3] Sevil Yaman T. “Analysis and stiffeners' design of a steel bridge girder”. Journal of Structural Engineering & Applied Mechanics, 5(3), 181-196, 2022.
[4] American Institute of Steel Construction (AISC). “ANSI/AISC 360-16: Specification for Structural Steel Buildings”. AISC, Chicago, IL, US, 676, 2016.

The influence of lower floor fires on the comprehensive structural performance of a residential structure

Abdulsamet AKTURK[1] , Burak Kaan CIRPICI [2]

[1,2]Civil Engineering Department, Engineering and Architectural Faculty, Erzurum Technical University, Erzurum, Turkey.

Abstract

In the years that ensued after the events of the September 11 attacks on the World Trade Center (WTC) in New York City in 2001, a multitude of investigations have concentrated on comprehending the effects of fire on building structures. The collapse of the WTC towers underscored the necessity for a more profound comprehension of how tall buildings behave under the influence of fire. It is imperative to guarantee that structural frameworks possess sufficient fire resistance capabilities across various fire scenarios. The failure of columns in the event of a fire can trigger the gradual collapse of a building, typically culminating in significant economic and human losses. After initial research and analysis, an eight-story residential steel structure was modeled using SAP2000. Multiple fire scenarios were replicated on various floors, including those affecting exposed primary load-bearing steel components, in order to generate temperature-dependent strength data. The evaluation of steel elements' strength involved examining their performance in terms of axial compression, bending moment, and shear forces across different situations, encompassing yield and ultimate stress conditions, as well as variations in the modulus of elasticity. Furthermore, the thermal characteristics of the reinforcement mesh within the concrete block of the slabs were examined at varying depths. This examination took into account alterations in axial, moment, and shear forces under scenarios involving both protected and unprotected steel elements. Additionally, the displacement of the slab caused by the prolonged exposure to high temperatures was assessed and compared to permissible deflection limits.

These analyses were conducted to investigate the effects of fire on steel structure performance, aligning with the ISO 834 standard adopted by European Standards. The results of the fire scenario analysis under varying temperature conditions were obtained for a fire event on the first three floors. The findings reveal a correlation between increasing temperature values and a decrease in structural integrity. After 60 minutes of exposure to elevated temperatures, the ground floor experiences a 48.82% reduction in axial force (compression) in the HE300A column, with no change in moment. However, there is a 48.42% reduction in shear force. In the case of the HE140A console beam, although there is no axial force, there is a 76.47% reduction in moment and a 38.25% reduction in shear force. The HE140A edge beam shows a 28.46% decrease in moment and an 8.17% reduction in shear force. With increasing temperature levels, the stress ratios of load-bearing steel structural elements also increase. For example, the HE 300A column exhibits stress ratios of 1.289 at 600ºC and 6.084 at 940ºC. The HE140A console beam shows a stress ratio of 1.497 at 940ºC, and the HE 140A edge beam records a value of 6.367 at 940ºC. These values surpass the ideal stress ratio range of 0-1. This suggests that at the specified temperatures, the load-bearing capacity of the steel elements has been compromised. Additionally, it has been deduced that steel structural components on various floors and axes, excluding the exposed column beams, have been influenced by the elevated temperatures, resulting in increased stress levels. This analysis offers insights into the degree to which the overall structural integrity of the simulated multi-story building has been impacted.

Keywords: compartment fires, fire protection, residential structure, structural fire performance

---

[1] Corresponding author

Mineralogical characterization of Pb-Zn-Cu mineralizations at Karagöl, (Çelikhan, Adıyaman)

Yavuz KAYA[1], Leyla KALENDER[2]

[1]Malatya Sular İdaresi Müdürlüğü, Malatya
[2]Fırat Üniversitesi, Mühendislik Fakültesi, Jeoloji Mühendisliği Bölümü, 23119, Elazığ

Abstract

The study area is located in the southwest of Adıyaman province. The oldest outcropping unit is the Pütürge metamorphic rocks (Cambrian-Carboniferous), which outcrops in the northeast of Çelikhan, and forms augen gneisses, quartzites, amphibolite schists, micaschists, and chlorite schists. The rocks of the Maden Group (Middle Eocene) and some volcanic-plutonic intrusions form the other lithological units of the study area. The Pütürge metamorphites reached their observed positions with the geological events in the Upper Cretaceous-Early Miocene interval. The study area is located between Çelikhan and Malatya, where different geological structures are observed. The lithological units identified so far are the Koçali Complex, the Yüksekova Complex, the Maden Group, and sedimentary and volcanic rocks. These units show both intrusive and tectonic contacts with Pötürge metamorphic rocks. The intrusive and tectonic/structural contacts are mineralization settings. The source of mineralizations can be considered as volcanic and plutonic rocks with different characteristics in the study area. Metabasic, metagranitoid, and metacarbonates associated with structural units consisting of both dip-slip reverse and strike-slip faults in the Pütürge metamorphites indicate the preference of mineralizations to settle within weak zones. It can be said that the ore-bearing zones generally form sulphide compounds within the north-south trending faults. In most mineralizations, metal aggregations can occur at different stages and may reflect multiple paragenesis and successions. It is necessary to distinguish between the deep origin and the superficial origin phase of ore-mineral formations characteristics. For example, in Pb-Zn mineralizations; sphalerite forms before galena. The presence of pyrite in this paragenesis indicates that solutions containing iron are effective in the formation of pyrite. It can be said that the compounds of zinc with sulphur and the formation of sphalerite may have occurred later. Like pyrite, pyrrhotite is one of the first minerals to form. Silver and its compound antimonite are the last minerals to form. In determining the sequence, the formation of the mineralization should first be defined by the host rock petrography. This is because the paragenesis and succession characteristics mentioned above may change for each mineralization formation. For example, pyromethasomatic formation successions may be different, hydrothermal ore formation successions may be different. The more a mineralization is formed at a higher temperature, the better the succession can be defined. The mineralogy of the ore was determined using SEM-EDX (Scanning Electron Microscope-Energy Dispersive X-ray) and polarising microscopy on samples taken from altered ore zones outcropping around Karagöl. From the mineralogical studies, both the polarising microscope data and the SEM images and EDX results indicate that the metal contents in the carbonate host rocks can be divided into three groups. The first group is galena, sphalerite, silver sulphur salts or native silver formed by high Pb>Zn>Ag and sulphur compounds. Second group; pyrite, sphalerite, galena composed of high Fe>Zn>Pb and sulphur compounds; the third group; chalcopyrite, covelin, galena, sphalerite, and barite formed by Cu>Pb>Zn>Ba and sulphur compounds. Considering that the mineralization follows weak zones in the host rocks and the hydrothermal solution in these zones may have been shaped by pH and redox conditions, it can be said that the hydrothermal cycle is effective in paragenesis and succession. It can be said that the gold enrichments, which are notable for with their high pyrite content, occurred before the silver enrichments. Sphalerite formations due to low Fe and high Zn contents are indicative of intermediate sulphidation conditions, whereas the association of high Cu contents with pyrite shows that intermediate sulphidation conditions are transitional to high sulphidation conditions. From the SEM-EDX data it can be seen that the high sulphidation redox conditions, accompanied by Ba, allow the formation of barite due to the oxidation of Cu compounds, therefore barite is formed together with

---

[1]Corresponding author

copper minerals. It is noted that the high levels of Si, Mg, and Na reflecting the country rock feature in only one sample indicate that the intrusion causing the mineralization is basic. The manganese content (347 ppm) must originate from the Mineral Group (Middle Eocene) volcanic sedimentary rocks. In the sample from the study area, the chemical primary element composition of the whole rock is 4.87% Fe, 2.82% Ca, 0.33% Mg, and the trace element contents of Au, Ag, Pb, Zn, Cu (1.8 ppb, 1278 ppb, 114 ppm, 228 ppm, 250 ppm, respectively) show that they are compatible with the mineralogical composition.

Keywords: Karagöl, mineralization, succession, paragenesis

Estimating undrained strength of an alluvial soil using resedimented samples prepared from disturbed samples

Muhammet Oğuz SÜNNETCİ[1], Hakan ERSOY[2]

[1,2]Department of Geological Engineering, Karadeniz Technical University, Trabzon, Türkiye

Abstract

In this study, an estimation model was developed to determine the shear strength parameters of disturbed soil samples using resedimented samples. In this context, plastic and index property determinations and UU triaxial compressive strength tests were carried out on undisturbed alluvial soil samples obtained by core drillings from Bafra district of Samsun city, Türkiye. 5 boreholes, each 10 m deep, were drilled in the study area and undisturbed soil samples were collected using custom-made 9 cm diameter, 60 cm long (maximum sample length is about 50 cm), thin-walled UD samplers. To minimize sample disturbance, no drilling fluid was used, and the samplers were driven into the soil by hydraulic pressure without rotation. Groundwater was encountered at a depth of 2 to 3 meters, and since the resedimented samples would be fully saturated, undisturbed samples were collected between 4 and 10 meters to ensure maximum saturation. By collecting a single undisturbed sample every 50 cm, a total of 60 undisturbed samples were collected from all 5 boreholes (12 samples from each borehole). Since it would be practically difficult to obtain 3 triaxial test specimens (needed to determine cohesion and internal friction angle) from one UD sampler, a single triaxial test specimen was obtained from each sampler. In this way, 3 specimens obtained from 3 consecutive UD samplers were considered as a single set of samples. The remaining part of the specimens in each UD sampler were used to determine their plastic and index properties. Natural water content, natural unit weight, specific gravity, void ratio, saturation degree, Atterberg limits, and grain size distribution of all samples are determined by laboratory tests conducted conforming to the corresponding international standards, or by using phase relation equations among the parameters determined during the tests. Additionally, undrained shear strength (s↓u) and shear strength parameters (cohesion, c and internal friction angle, ϕ) of the samples are also determined by unconsolidated-undrained (UU) triaxial tests conducted using a servo-controlled semi-automatic testing system. The triaxial tests were carried out under 50, 100, and 200 KPa of confining pressures with a 0.5 mm/min shear rate until 20% strain is occurred. Ultimately, 20 sample sets were created with known index, plastic, and strength properties. These samples, which were disturbed after the initial experiments, were resedimented in the second stage of the study by reflecting their original characteristics in the field. Consolidometers with a diameter of 9 cm, designed and produced within the scope of this study, were used in the resedimentation process. During the resedimentation process, each sample was subjected to a consolidation stress equal to the burden stress at the depth from which it was taken from the boreholes. The disturbed soil sample was dried in an oven at 105°C for 24 hours. The dried sample was ground in a ring grinder to pass through a #100 sieve. Approximately 1 kg of material was ground for each resedimented sample to be prepared. The ground soil sample was mixed with deaired distilled water of 2 times its initial liquid limit in weight. To obtain a homogeneous mixture, an attempt was made to mix the slurry with a laboratory mixer for 10 minutes. However, due to the high degree of agglomeration in the samples prepared in this manner, the mixing process was performed manually. The prepared homogeneous slurry was slowly poured into a consolidometer with filter paper on the bottom to avoid air bubbles. The slurry was left to stand for 24 hours. At the end of 24 hours, a piston with filter paper on the bottom was placed on top of the sample and the top cover of the consolidometer was closed tightly. The loading arms were attached to the top cover and a load of 0,5 kg (approximately 2.5 KPa of stress) was initially applied to the sample. The load was then gradually increased by doubling the load on the specimen until the desired consolidation stress was reached. Each loading step was applied for 24 hours. The final loading step was applied for 48 hours. Once the loading process was complete, the load on the sample was removed while holding the piston stationary. The UU triaxial compressive strength tests were repeated on the resedimented samples. Multivariate regression (MVR) analyses were

---

[1] Corresponding author

performed on the physical and mechanical properties of undisturbed and resedimented samples to predict the cohesion, internal friction angle, and undrained shear strength of undisturbed samples. Multivariate regression analyses were performed using SPSS® v23 software and the significance of each independent variable was also tested. Independent variables with low significance coefficients were removed from the analysis and the analyses were repeated to develop empirical equations with high correlation coefficients (R) and as few parameters as possible. Again, for ease of application, linear equations were preferred to logarithmic or exponential equations unless there was a large difference in R values. As a result of the MVR analyses, 6 equations were obtained for undrained strength, cohesion, and internal friction angle with highest coefficient of correlation values of 0.803, 0.817, and 0.850, respectively. When the statistical analyses are evaluated, it can be seen that the MVR analyses produced equations based on a maximum of 3 different parameters and with high correlation coefficients (0.795 and above). Using these equations, the shear strength parameters of the undisturbed samples can be estimated with high accuracy using the shear strength parameters of the resedimented samples.

Keywords: Resedimentation, disturbed sample, undrained shear strength, cohesion, internal friction angle, multivariate regression

International Conference on Advances and Innovations in Engineering

Evaluation of rockfall risk in the southern of İçme (Elazığ) By 2D numerical analysis method

Ali Burak AKTAŞ[1], Mustafa KANIK[2]

[1]Ministry of Environment Urbanization and Climate Change, Planning and Settlement
[2]Department of Geological Engineering, Faculty of Engineering, Fırat University

Abstract

Rock falls are defined as rapid and sudden movements of rock blocks under the influence of gravity where the rock blocks slide along the discontinuity surfaces then move along the direction of the inclination Rock falls have triggered numerous disasters worldwide, including incidents in Turkey. While rockfall events may not impact large populations like earthquakes, floods, or fires, they can lead to loss of life and property within localized areas. Rockfalls pose a significant danger when they occur in areas frequented by people and other living creatures.

This study aimed to assess the potential rockfall hazard in the southern section of the İçme residential area in Elazığ. To conduct comprehensive engineering geology research for analyzing the rockfall issue, detailed field investigations were initiated. Through these investigations, areas prone to rockfall problems were identified and an engineering geology map of the region were drawn. The risk of rockfall in the study area occurs within the limestones of Maastrichtian- Eocene aged Hazar Formation.

This study investigated the potential rockfall risks in the southern part of the İçme residential area in Elazığ and identified two distinct source rock masses. For source rock 1, the region susceptible to its influence was assessed along three different lines, considering potentially hazardous blocks. Kinematic analyses were conducted for these slopes to determine their stability. Additionally, numerical analyses were performed using RocFall2D software for both source rock 2 and source rock 1 regions. These analyses considered historical rockfall events and determined the potential distances that blocks could travel.

This study commenced with field investigations aimed at identifying discontinuity orientations and characteristics using the scanline survey method. Following the scanline surveys, field-obtained discontinuity trends were processed using Dips v 5.1 software, resulting in the identification of seven dominant discontinuity sets and random discontinuities within the study area. The internal friction angle of the rock was determined to be approximately 39 degrees through field tilt tests. Kinematic analyses were conducted based on the obtained discontinuity data, and these analyses encompassed four distinct lines in the source rock 1 region. The selection of four different lines was motivated by the potential for instabilities along any of these lines to directly impact the southern section of the residential area.

Numerical analysis software plays a crucial role in determining the travel distances of rock blocks dislodged from the source rock and provides valuable insights into the areas to be secured and precautionary structures when assessing the potential locations where these blocks might land and their maximum projected heights. Within the scope of this study, RocFall2D software for numerical analysis was utilized. To ensure the accuracy and precision of our numerical analyses, it was imperative to extract the topographic sections with great precision. After determining the field lines, detailed cross-sections were meticulously drawn. In our

---

[1] Corresponding author

analyses, we treated rock blocks as rigid bodies, an approach justified by the examination of previously fallen rock blocks in the field and the measurements taken from them, ensuring realistic block shapes. This approach allows us to determine both the translational and rotational speeds and energies of the rock blocks. The block shapes chosen from the program options reflected those observed in the field, such as super ellipsoid (2:3) and polygonal (2:3). Initial movement speeds were set at 0.5 m/sec. Block sizes for the analysis were selected based on measurements taken in the field, including dimensions like 130/130/110 cm, 140/110/76 cm, 110/60/85 cm, 130/100/75 cm, 95/80/50 cm, and 80/70/40 cm..

Taking into account both the historical rockfalls and potential future incidents, it becomes evident that rockfalls along Line I pose no direct threat to the residential area. Conversely, it is clear that rockfalls along Lines II, III, and IV present a direct risk to the southern part of the residential area. In the analysis conducted along Line V, it is observed that the blocks could potentially reach the border of the zoning plan. By evaluating the data obtained from these various observational, kinematic, and numerical analyses, the necessary precautions and their respective application locations were pinpointed. These findings have been meticulously documented on the engineering geology map.

As a result of our comprehensive studies, it has been determined that the most economical and safe approach for the Line V region, which has previously experienced rockfalls, is to construct a barrier using the fallen rocks from that area. For Lines II, III, and IV, where the analysis indicates a risk of falling rocks, it is recommended to install energy-absorbing steel barriers with a minimum height of 2 meters, as modeled in the analyses. Considering the potential heights that rocks could reach, the use of energy-absorbing steel barriers is highly advisable. A continuous energy-absorbing steel barrier spanning 160 meters along the designated line is proposed. Furthermore, to enhance safety within the development plan area and mitigate the risk posed by the blocks extending towards the southern part of the residential area, it is recommended to construct a protective wall using existing rock blocks. This wall should have a minimum height of 1.5 meters and should extend along a 100-meter line. Implementation of these measures will help mitigate potential rockfall risks.

In light of all the aforementioned factors, it is strongly recommended that there exists a real and imminent risk of rockfall affecting the southern portion of the area encompassed by the "Settlement Area Boundaries in İçme (Elazığ)" study. Immediate precautionary measures should be prioritized to ensure the safety and security of this residential area.

Keywords: Rock Fall, Kinematic Analyses, Numerical Analyses

International Conference on Advances and
Innovations in Engineering

Investigation of the landslide induced tsunami waves in artificial dam lakes: the case of hardısağır landslide

Murat KARAHAN[1], Hakan ERSOY[2]

[1,2]Department of Geological Engineering, Karadeniz Technical University, Trabzon, Türkiye

Abstract

Within the scope of the study, tsunami wave effects caused by gravity in the artificial reservoir area were investigated. Within the scope of the study, the effect of the impulse wave that will occur in the lake area as a result of the movement of the riskiest of these landslides by earthquake effect of the North Anatolian Fault on the lake area and the dam body was investigated. Kürtün dam is a rock-fill dam with a concrete-covered front face. The maximum water level is 645 m, the crest elevation is 650 m and the water column thickness at the deepest spot is 100 m. The landslides identified are Süme, Dutluca and Hardısağır landslides. It was understood from the field studies that there was no movement in the Süme landslide, and even if there was a movement, it was not risky considering the water depth in the impact zone and the geometry of the impact zone. Half of the Dutluca landslide is submerged, and no current deformation has been detected in the landslide. In the studies carried out on the Hardısağır landslide, many deformations were detected indicating that the landslide was active. Considering the activity, volume, and location of the Hardısağır landslide, it has been determined that the riskiest landslide is the Hardısağır landslide. After the riskiest landslide was identified, the effects of the impulse wave that would occur as a result of earthquake effect of the landslide were investigated with 3D numerical simulations. Within the scope of the study, firstly, data from the drillings carried out by SHW 22nd Regional Directorate were obtained. From the drillings, the slope debris-bedrock boundary was determined. Afterwards, 3 approximately 400-m long ERT (Electric Resistivity) measurements were made for the boundaries of the landslide area to determine the groundwater status and formation boundaries. In order to determine the necessary physical and mechanical properties of the soil to be used in stability analyses, 5 research pits were opened within the borders of the landslide area and disturbed and undisturbed samples were taken. Shear box, liquid limit, plastic limit, and sieve analyzes were performed on the soil samples taken. As a result of the literature investigations, field studies, and laboratory tests, the dimensions and physical and mechanical properties of the landslide were revealed. After these features were determined, a 3-D limit equilibrium analysis was performed and the safety number of the landslide for the earthquake situation and the amount of material to slide into the lake area were determined. One of the most important parameters affecting the properties of the impulse waves is the volume of the material that will slide into the lake area. For this reason, the amount of material to slide has been calculated with precision in 3D. After determining the amount of material that will slide from the Hardısağır landslide to the lake area as a result of a possible earthquake on the North Anatolian Fault line, the impulse wave that will occur was simulated in 3D using the Flow-3D software. The solid model of the study area required for the 3D numerical simulation was created from the point cloud produced from the orthophotos obtained from the General Directorate of Mapping. After creating a 3D solid model of the lake area and its surroundings, probes were placed on the solid model in a coordinated manner for point measurements of dam body, landslide material to flow into the lake area, reservoir water, and hydraulic data. After the model was established, the effects of the impulse wave that will occur as a result of a possible movement of the Hardısağır landslide were investigated numerically in 3D. As a result of all the studies, it has been determined that the average thickness of the landslide material is 30 meters in width and 300 meters in length. As a result of the geophysical studies, it has been determined that the electrical resistivity values vary between 900 and 1010 ohm.m, the P-wave velocities vary between 400 and 905 m/sec and the S-wave velocities vary between 175 and 223 m/sec. According to the laboratory test results, it has been determined that the unit weight of the soil is 17.7 to 18.8 kN/m3, its cohesion is between 7.2 and 11.4 kPa, the internal friction angle varies between 20.4 and 30.4 degrees, and the soil is of ML-OL, MH-OH classes according to the unified soil

---

[1] Corresponding author

classification system. It has been determined that 875,240 m3 of material will slide into the lake area from the 3D limit equilibrium analysis made for an earthquake situation. The solid model of 875.240 m3 material obtained from the 3D limit equilibrium analysis was integrated into the 3D solid model of the entire lake area and 3-dimensional numerical analyzes were carried out in the Flow3D software. Analyzes were made for the maximum water level at 645 m elevation. In numerical simulations made taking into account the 3D lake area topography, the impact speed of the landslide mass is 45 m/s., the impact time of the landslide mass is 9 sec., the maximum wavelength in the impact zone is 30 meters, the amount of advance on the opposite shore (horizontal) is 193 m, the amount of advance on the opposite shore (vertical) is 75 m, the time to reach the dam body is 101 seconds, the wave height reaching the dam body is 2.5 m and the speed of the wave reaching the dam body is 22 m/sec. Considering the characteristics of the wave formed as a result of the earthquake effect of the Hardısağır landslide, it was determined that the impulse wave had a destructive effect on the lake area and its surroundings. In particular, it has been determined that the destructive wave formed in the impact zone poses a great risk for Özkürtün and the fish farms on the right coast.

Keywords: Landslide, tsunami, impulse wave, Hardısağır landslide, Kürtün Dam

Petrogenesis of late Cretaceous subduction-related volcanics rocks, southeast of Elazığ, Turkiye

Mehmet Ali ERTÜRK[1]

[1]Department of Geological Engineering, Fırat University, Elazığ, Turkey

Abstract

The Southeast Anatolian Orogenic Belt (SAOB), located between the Taurides and the Arabian Platform, is one of the most complex segments of the 7000-km-long Alpine-Himalayan orogenic belt. In the SAOB, subduction-related volcanism is an important part of the arc system located between the convergence zone of the Arabian Platform and Taurides. The SAOB resulted from the north-dipping subduction of the southern Neotethys oceanic lithosphere in the late Cretaceous, and is approximately EW-trending and represents the northwestern part of the Bitlis-Zagros Suture Zone. The study area is the central part of the SAOB, located between the Taurides in the north and the Arabian Platform in the south. The region comprises Guleman ophiolites and Elazığ magmatic Complex, two important late Cretaceous units. The Guleman ophiolite is typically composed of harzburgites containing dunite and podiform chromite. The Guleman ophiolite contains mantle tectonites, mafic and ultramafic cumulates, and the bottom part of the oceanic lithosphere. Tectonites, cumulates, isolated dykes, diabase, and fundamental volcanic rocks make up this formation. Tectonites are composed of banded gabbros, dunite-verlite-clinopyroxenite cumulates, and harzburgites with dunite and podiform chromite at the unit base. On tectonites, typically in their vicinity are cumulate group rocks. At these levels, harzburgites with dunite and podiform chromite predominate. Layered cumulates have covered mantle tectonites. The ophiolite is divided into several structural levels by diabase dikes. More than a few kilometres of mantle tectonites exist. The Elazığ magmatic complex is made up of plutonic rocks, including gabbro, diorite, tonalite, quartz diorite, granite, granodiorite, quartz monzonite, and monzodiorite, as well as volcanic rocks such as basalt, basaltic andesite, andesite, dacite, and rhyolite. The rocks of the Elazığ magmatic complex contain abundant mafic microgranular enclaves, and the rocks are cut by dykes of aplite, diabase and lamprophyre. This study investigates mineralogy, petrography and petrogenesis for subduction-related volcanics. The volcanic rocks are represented by basalt and basaltic andesite. The volcanics have phenocrysts of plagioclase and pyroxene and exhibit aphanitic, microlitic, ophitic, glomeroporphyritic, intersertal, and amygdaloidal textures. The volcanics are mostly dark grey, grey to dark black basalts. Volcanic rocks are observed as pillow shapes and massive lavas. These rocks contain characteristic pillow-shaped structures attributed to the ellipsoidal, flattened, spherical, swollen tube-like lobes and local peduncles. This study includes the subduction-related volcanism cropped out southeast of Elazığ district and aims to reveal the origin of these rocks by major-trace element and isotope geochemistry. The geochemistry data of these rocks supported by their ages were determined by the zircon U-Pb geochronological dating method. Major elements were measured using X-ray fluorescence analyses (XRF) and trace elements using inductively coupled plasma mass spectrometry (ICP–MS). The isotopic ratios 87Sr/86Sr and 143Nd/144Nd were measured in a subset of samples using a multi-collector ICP–MS (Finnigan-Thermo Neptune) after separating the Sr and Nd by repeated digestion and chemical separation. The zircon U–Pb isotopic analyses were dated using an Agilent 7500s quadrupole ICP-MS instrument equipped with a Photon Machines 193 nm Analyte G2 excimer laser ablation system The samples have variable contents of SiO2 (45–59.75 wt.%), TiO2 (0.45–2.38 wt.%), Al2O3 (12.77–18.88 wt.%), Fe2O3 (6.40–14.47 wt.%), Na2O (1.13–6.36 wt.%), K2O (0.00–1.11 wt.%), P2O5 (0.06–0.42 wt.%), and MgO (2.92–8.16 wt.%). The samples show two sets of similar trends in the primitive mantle-normalized immobile element diagrams, with E-MORB (group 1) and N-MORB (group 2). Two separate trends for LREEs are shown in the chondrite-normalized REE diagram. Group 1 sample exhibits depletion in LREEs (LaN/YbN = 0.34-1.56) and HREEs (LaN/YbN = 0.75-1.53) are mostly flat-lying, but group 2 samples display depletion in LREEs (LaN/YbN = 0.34-1.56) and more fractionation in LREEs. 87Sr/86Sr(i) values vary from 0.705250 to 0.706114,

---

[1] Corresponding author

143Nd/144Nd(i) values range from 0.512834 to 0.512888, while Nd(T) values range from 5.9 to 7.0. The crystallization age of the volcanism was 83.93 1.21 Ma, according to zircon U-Pb dating. The geochemical, isotopic and geochronological constraints point to a tectonic process of an intra-oceanic arc setting from the northward subduction during the Late Cretaceous as the potential sources and evolution of the subduction-related volcanic rocks.

Keywords: geochemistry, petrography, Sr-Nd isotope, subduction-related volcanics, U-Pb geochronology

Chemistry of Cr-spinel in podiform chromitites from Islahiye Ophiolite (Gaziantep, SE Anatolia)

Mustafa Eren RİZELİ[1]

[1]Department of Geological Engineering, Faculty of Engineering, Fırat University, Elazığ, Türkiye

Abstract

Geoscientists frequently study ophiolites, fragments of ancient oceanic crust and upper mantle, to reveal the evolution of ancient oceans and orogenic belts. In recent years, studies on mantle peridotites and chromitites have played an important role in describing events such as melt formation and melt-mantle interaction in the ancient oceanic lithosphere. Revealing the mineral compositions of mantle peridotites and chromitites supplies critical knowledge about the features of the melts formed due to the partial melting of the mantle and the tectonic environments to form ophiolites. Due to the relatively high resistance of the chromian spinel (Cr-spinel) to alteration, this mineral is frequently used as a petrogenetic indicator to reveal the main melt composition and the degree of partial melting of the mantle under different tectonic conditions. Tethyan ophiolites, separated by Gondwana-derived microcontinents during the Mesozoic-early Cenozoic, are located in the nearly east-west-trending. The Bitlis-Zagros suture zone divides the Tauride Belt in the north from the Arabian Platform in the south. The closure of the southern branch of Neotethys resulted in the collision of the Tauride Belt and Arabian Platform during the middle-late Miocene. The rocks examined in the Islahiye region are divided into Ophiolite Nappes, Tertiary Cover Units and Autochthonous Arabian Platform. The Autochthonous Arabian Platform (lower Cambrian to upper Ordovician) contains sandstone, quartzite, shale, and limestone from bottom to top. Upper Triassic-lower Cretaceous dolomite and dolomitic limestone unconformably overlain these basement rocks. Upper Triassic-lower Cretaceous aged dolomite and dolomitic limestone are unconformably overlain by these basement rocks. Ophiolitic rocks tectonically overlie the Arabian platform. The ophiolitic rocks in the investigated area are extremely fragmented and altered and generally consist of gabbro and mantle peridotites. Due to the intensity of tectonism in the region, it is not easy to separate peridotites into different lithological units according to their chemical and mineralogical properties. The mantle peridotites of the late Cretaceous Islahiye ophiolite are generally serpentinized dunite, dunite, serpentinite and serpentinized harzburgites in the study area. Highly serpentinized dunite and harzburgites, the prevailing rock type of the Islahiye ophiolite, host chromite formations. According to previous studies, chromites in the region are thought to be mostly related to tectonic movements and crop out in a limited area; these chromites were generally observed as lenticular and banded masses with disseminated and massive textures. Most of the Cr-spinels investigated have notable cracks and breccias, which are considered to be generated by dynamic metamorphism. The chromitites typically contain less than 15% silicate. Cr-spinels are mainly fresh. However, ferrous alteration is occasionally observed in some grain boundaries, cracks and brecciated areas. The mineral chemistry of chromites is an important and reliable means of petrogenetic interpretation. Polished thick sections were prepared at the Department of Geological Engineering, Fırat University (Elazığ, Türkiye). The general mineralogy and petrographic features were studied with a Leica DM2500 P microscope under transmitted and reflected light equipped with a Leica Flexacam C3 12 MP digital camera. Chemical compositions of the Cr-spinel of peridotites were investigated with an electron probe micro-analyzer (EPMA) at the Institute of Earth Sciences, Academia Sinica (Taipei, Taiwan). The mineral identification was done using Oxford Instruments Ltd., Xmax − 50 with INCA − 350, and the precise compositions were obtained using a JEOL EPMA JXA − 8900R equipped with four wavelength dispersive spectrometers. Secondary- and back-scattered electron images guided the analyses to the target positions. The instrument was operated at an acceleration voltage of 15 kV with a 12 nA beam current and a defocused beam with a diameter of 2 μ. Approximately 76 EPMA spot analyses were performed on the unaltered cores of Cr-spinel, exhibiting a wide range of compositional

---

[1] Corresponding author

variations as Cr2O3 (45.97 – 60.40), Al2O3 (5.73 – 19.95), FeO (13.57 – 27.59) and TiO2 (<0.10). The Cr-spinels of the Islahiye chromitites plot within the ophiolitic podiform chromitite field. Chromitites can be divided into two groups compositionally: (1) high-Cr (or metallurgical) chromitites with a Cr# (Cr / Cr + Al) higher than 0.60, and (2) high-Al chromitites (or refractory) lower than Cr# 0.60. The values of Cr# vary from 0.61 to 0.87 and Mg# from 0.32 to 0.65. The investigated chromitites are high-Cr chromitites (or metallurgical; Cr# > 0.6). The spinel-type of high-Cr Islahiye chromitites with metallurgical character are magnesiochromite and chromite. According to previous studies, Islahiye chromites present an enrichment in IPGE with the occasional presence of Ru and Ir and higher Os contents in chromite. Mineralogical and geochemical data from the Cr-spinel of the Islahiye chromitites show that high-Cr chromites are formed regarding boninitic composition melts formed by re-consumption of the previously partially depleted mantle.

Keywords: Cr-Spinel, podiform chromitite, high-Cr chromitite, mineral chemistry, Islahiye ophiolite, Gaziantep

Petrography and mineralogy of the Doğanşehir bauxites (Malatya-Turkey)

Hatice KARA[1]

[1]Firat University, Department of Geological Engineering, Elaziğ, 23119 Turkey

Abstract

Bauxite deposits can be divided into three main groups, depending on the bedrock lithology: bauxite deposits overlying aluminosilicate rocks and bauxite deposits overlying carbonate rocks. Tikhvin-type deposits, the product of erosion of lateritic bauxite deposits, covering the eroded surface of aluminosilicate rocks. Bauxites made of laterite that are remnant deposits or deposits that have only undergone limited redeposition. Regardless of whether the bedrock surface is karstified or not, or the level of karstification, bauxite found on carbonate rocks can be classified as karstic. Karst bauxites, which make up 14% of the world's bauxite deposits, have been further classified into several types based on their morphology, composition, and geo-paleogeographical characteristics. Doğanşehir region (Malatya-Turkey) is located in the Eastern Taurus Orogenic Belt, one of the main tectonic belts of Turkey. In terms of structural makeup, the Tauride Belt is the region where autochthonous and nappe structures predominate. The Tauride belt is rich in bauxite deposits of various ages (they range from Permian to Eocene) and formation types (Muğla, Payas-Islahiye, Isparta, Seydişehir, Bolkardağı, Alanya, Tufanbeyli-Saimbeyli-Kadirli bauxite deposits), with the karst type being the most significant. The Permo–Triassic Malatya Metamorphics form the basement of this region. This unit is overlain by Late Cretaceous Eocene Berit Metaophiolite, Eocene Maden Complex, Early–Middle Eocene Doğanşehir Granitoid and Plio–Quaternary cover sedimentary units. The Malatya Metamorphics are in tectonic and intrusive contact with the Doğanşehir Granitoid, and tectonic with the Maden Complex. While Berit Metaophiolite overlies the Middle Eocene Maden Complex at the bottom due to Eocene tectonism, it is tectonically overlain by the Malatya Metamorphics at the upper. The Doğanşehir granitoid crops out in a tectonic window, where the Malatya-Keban metamorphics were eroded along E–W trending Sürgü and NE–SW trending Malatya-Ovacık fault zones. Various researchers have regarded the extensively observed Malatya Metamorphics as the southern extensions of the Keban Metamorphics and similar units to the Keban Metamorphics. The Malatya Metamorphics, which is the last drift slice that settled in the region, into two parts, Lower and Upper Metamorphics. In Doğanşehir region, there are oolitic and pisolitic bauxite mineralisations within Permo Triassic carbonate rocks. These mineralisations found in carbonate rocks containing fossils are observed through massive and lenses. The bauxite lenses are overlain by thin middle-layered Permo–Triassic carbonate rocks. The bauxite lenses are oriented NE–SW and reach up to 300 m lengths. The thickness of the bauxite layer ranges from about a few meters to tens of meters, largely controlled by the karst topography. In general, the ore texture is massive and oolitic-pisolitic. The bauxite zone is coloured brownish-red, dark red. In the field, only iron oxide (hematite) can be recognised by the naked eye. In petrographic studies of bauxites, it was determined that the minerals were fine-grained. Spherical grains are generally observed in ooliths and pisolites but also testify to the original heterogeneity of the colloids resulting from the alteration and weathering of the carbonate rocks. The various shapes and sizes of ooliths and pisolites, together with elongated nodules, indicate re-depositional conditions during the evolution of this sediment. The mineralogical composition of the bauxite ore samples was investigated via a petrographic examination of thin and polished sections and X-ray diffraction (XRD). X-ray diffraction analyses show that diaspore and hematite are the main minerals of the ores. Minerals such as anatase, gibbsite and zeolite were formed as minor minerals in the ores. The geochemistry of the depositional/diagenetic environment of bauxite production has been hypothesized to be "vadose" and "phreatic" at its extremes, and/or to be characterized by goethite. In contrast, phreatic bauxites are characterised by goethite, siderite and/or pyrite with or without chlorite, diaspore, and/or boehmite as aluminium minerals. In terms of mineral assemblage and ore texturing, Doğanşehir bauxite formations can be compared to

---

[1] Corresponding author

vadose bauxites. Moreover, Among them, the major component in subtropical regions is boehmite, whereas predominantly gibbsite bauxite appears to be more confined to the tropicsand is characterised by a warm rainy climate with alternating dry periods. Among them, the primarily component in subtropical locations is boehmite, howewer gibbsite bauxite appears to be more confined to the tropicsand is characterised by a warm rainy climate with dry periods. According to studies, it is uncommon to see diaspore directly accumulate from Al solutions. These investigations also imply that higher pressure hydrothermal processing of the gibbsite may result in the formation of diaspore.

Keywords: bauxite, Eastern Tauride, petrography, mineralogy

International Conference on Advances and Innovations in Engineering

International Conference on Advances and Innovations in Engineering
2.ICAIE

Earthquake cycle of the East Anatolian Fault section between Palu and Pütürge: Preliminary findings

Mehmet KÖKÜM[1], Havva Neslihan Kıray[2], Cengiz Zabcı[2], Hüsnü Serdar Akyüz[2], Erhan Altunel[3], Semih Ergintav[4], Abdulrahman Elhisso[1]

[1]Department of Geological Engineering, Faculty of Engineering, Firat University, Elazığ, Türkiye.
[2]Department of Geological Engineering, Faculty of Mines, Istanbul Technical University, Istanbul, Türkiye
[3]Department of Geological Engineering, Faculty of Engineering, Eskişehir Osmangazi University, Eskişehir, Türkiye
[4]Department of Geodesy, Kandilli Observatory and Earthquake Research Institute, Boğaziçi University, Istnabul, Türkiye

Abstract

Türkiye is among the world's most seismically active zones as it is located on several active fault lines, with the most potentially devastating being the North Anatolian Fault Zone (NAFZ) and the East Anatolian Fault Zone (EAFZ). There have been more than a hundred recorded destructive earthquakes during the 20th and 21st centuries. The East Anatolian Fault Zone runs from Karlıova in the northeast, starting at the Karlıova Triple Junction where it meets the North Anatolian Fault Zone. As the East Anatolian Fault Zone continues to the southwest, it is divided into several distinct geometric segments. The main trace of the fault zone between Karlıova in the northeast and Türkoğlu in the southwest is generally agreed upon. However, the southwestern continuation beyond Türkoğlu is debated, as summarized with three possible scenarios: (1) The East Anatolian Fault Zone intersects the Dead Sea Fault Zone near Türkoğlu, (2) the Dead Sea Fault Zone connects with the East Anatolian Fault Zone with Karasu Fault near Turkoğlu, (3) the East Anatolian Fault Zone meets the Dead Sea Fault Zone in the Amik Basin. On February 6, 2023, a magnitude-7.8 earthquake hit at 4:17 a.m. local time near Pazarcık City in south-central Türkiye. This earthquake was followed by a second earthquake of magnitude 7.7 at 1:24 p.m. with the epicenter in Elbistan City. Both events are associated with the East Anatolian Fault Zone. Although the East Anatolian Fault Zone is one of the most important tectonic structures of the region, it is relatively poor in terms of historical earthquake and geological slip rate studies. The aim of this study is to determine the earthquake history and geological slip rates of the Palu and Pütürge segments of the East Anatolian Fault Zone to characterize the earthquake cycle of this transform fault system and to reveal the earthquake hazard for the region. The main motivation of this study is that the Palu and Pütürge segments of the East Anatolian Fault Zone in terms of paleoseismology and geological slip rate studies are limited. Another importance of the geographical scope of the project is that nearfield GPS, InSAR, and creepmeter data reveal the creep (aseismic slip) on this segment of the East Anatolian Fault Zone. In the scope of this study, a total of four trenches were excavated on the Palu and Pütürge segments of the East Anatolian Fault Zone. The Yeşilova trench (YT) was excavated at the northern edge of the elongated ridge within a small fan overlying old river deposits, where the fault scarp is prominent. The trench was about 18 m long and 3 m deep and exposed a sequence of predominantly fine sediments (silt and clay), with intercalated layers of sand and pebbles. Geological evidence of two possibly three surface faulting earthquakes that deformed the walls of the trench in Yeşilova trench was recognized. The Kartaldere trench (KT) was excavated across a gentle and broad cumulative south-facing scarp. Overall, the fault trace produces relative subsidence on the southern side, where ponding is observed against the scarp. The Kartaldere trench was about 18 m long and 2.5 m deep and exposed a sequence of predominantly fine sediments (silt and clay) that are considered low-energy environments. The trench exposed 2 main fault zones, which are distributed within a 5-m-wide zone. Evidence of two possibly three surface faulting earthquakes were found. Following the 24 January 2020

---

[1] Corresponding author

Mw=6.8 Sivrice (Elazığ) Earthquake that occurred in the East Anatolian Fault Zone, tension gashes were co-seismically developed within the brittle ice cover. The Kösebayır trench (KsT) was excavated across these structures. The Kösebayır trench was about 15 m long and 2.5 m deep and exposed a sequence of predominantly fine sediments (silt and clay) are considered low-energy environments. The trench exposed a few fault zones, which is distributed within a 2-m-wide zone. Evidence of two possibly three surface faulting earthquakes were found. The Yazıca trench (YT) was excavated across a gentle and broad cumulative north-facing scarp. The Yazıca trench was about 18 m long and 2,5 m deep and exposed a sequence of predominantly fine sediments (silt and clay). Evidence of two possibly three surface faulting earthquakes were found. The dating results of the charcoal and organic sediment samples collected from these four trenches are not yet available. Trenching along the Palu and Pütürge faults will provide new data about the earthquake history of this part of the EAFZ, as well as new insights on earthquake recurrence. This research is supported by the Project Number 121Y283 of The Scientific and Technological Research Council of Turkey (TUBITAK).

Keywords: earthquake, paleoseismology, strike-slip fault

Comparison of compression and tensile elasticity modules of rock material

Zülfü GÜROCAK[1] , Yasemin Aslan TOPÇUOĞLU [2], Alperen CANPOLAT [3]

[1,2]Geological Engineering Department, Faculty of Engineering, Fırat University, Elazığ, Turkey
[3] Graduate School of Natural and Applied Sciences, Fırat University, Elazığ, Turkey

Abstract

The modulus of elasticity is one of the most important input parameters in material studies and engineering designs, and is a measure of the material's capacity to resist deformation or rigidity. Rock material under stress is deformed as a result of stress, and shape, and sometimes both shape and volume changes occur in the rock material. One of the most important parameters controlling these deformations in the rock material is the modulus of elasticity. It is one of the elastic properties used as input parameter in many engineering designs such as dam, tunneling, slope stability, excavability and blasting design. The method used to determine this parameter is to measure the axial deformations in the rock material while performing a uniaxial compression test in the rock material and is to calculate the modulus of elasticity from the dip angle of the stress-strain curve drawn using the stress and axial deformations values. Determination of this parameter realistically and reliably has a significant impact on the reliability and cost of the design. While it is possible to obtain reliable values with experimental studies carried out in accordance with international standards, misuse of the modulus of elasticity is one of the most important obstacles to a reliable design. The most common misuse of this parameter is to use of compression elasticity modulus instead of tensile elasticity modulus, as it can be determined more easily. The tensile elasticity modulus of the rock material must be used especially in studies such as excavability, blast design, slope reinforcement and support in underground excavations while the compression elasticity modulus of the rock material is used as the input parameter in some engineering designs. Because, the elasticity modulus calculated under compression stress is the compression elasticity modulus and has a different value than the tensile elasticity modulus calculated for the rock material under tensile stress. Very few studies on this subject show that the compression and tensile modulus of elasticity of rock material is not the same, and the compressive modulus of elasticity is larger than the tensile modulus of elasticity. However, due to the difficulties in determining the tensile modulus of elasticity, designers use the more easily determined compression modulus of elasticity of the rock material instead of the tensile modulus of elasticity. This misuse affects the reliability and cost of the design, negatively. For this reason, it is necessary to investigate the relationships between compression and tensile modulus of elasticity in rock mechanics. The aim of this study is to compare the elasticity modules of compression and tensile and to determine the relationship between them. For this purpose, core samples were collected from 4 different lithologies: tuffite, clayey limestone, marl and andesite, and prepared for experimental studies. Uniaxial compression and direct tensile tests were performed on rock materials in accordance with the International Society for Rock Mechanics and Rock Engineering (ISRM) recommendations. The axial deformations in each sample were determined using strain-gauge glued to the rock samples and data-logger while performing uniaxial compression and tensile tests. Stress-strain graphs were drawn for each rock sample using the data obtained from uniaxial compression and tensile tests. The elasticity modules of compression and tensile were calculated with the help of stress-strain curves. At the last stage, statistical analyzes were evaluated to determine the relationships between these parameters. The average elasticity modules of compression and tensile of the rock materials used in this study were compared with statistical evaluations. In the comparisons, it was determined that the compression and tensile elasticity modules for different rock lithologies differ from each other at different rates. It was determined that the compression modulus of elasticity was 49% higher in tuffite, 20% in clayey limestone, 47% in marl, and 38% in andesite than tensile modulus of elasticity.

---

[1] Corresponding author

While the difference between the compression and tensile modules of elasticity was greater in low-strength rock materials such as tuffite and marl, it was less in clayey limestone and andesite, which have higher strength than other rock types. Also, it was determined that the compressive elasticity modulus was 36% higher than the tensile modulus of elasticity when the values of average compressive and tensile modules for all rock samples are taken into account. The relationship between the compressive and tensile modulus of elasticity of all rock material samples used in the study was investigated by simple regression analysis. According to the simple regression analysis; there was a strong positive relationship between these two parameters with a correlation coefficient (R) of 0.81

Keywords: Elasticity modulus, rock material, compression stress, tensile stress

Preliminary findings of dadağlı barite mineralization (Kahramanmaraş): Implication to its mineralogy and alteration geochemistry

Cihan YALÇIN[1]

[1]General Directorate of Industrial Zones, Worldbank PIU, Ministry of Industry and Technology, Ankara, Türkiye.

Abstract

Studying the alterations in the geochemistry of Paleozoic carbonate-hosted barite deposits is a complex area of research in the field of economic geology. The deposits, which are known for having high concentrations of barite, are important industrial minerals that have many different uses. However, the formation and evolution of these deposits are not only controlled by the accumulation of barite, but they are also closely connected to geological, geochemical, and hydrothermal processes. The changes in the geochemistry of these deposits are a complex subject that has been extensively studied. The deposits are associated with alteration minerals such as barite, quartz, calcite, dolomite, and pyrite. The specific deposit can cause variations in the relative abundance of these minerals, but they all contribute to the formation and development of barite mineralization.

Barite is considered to be one of the most significant alteration minerals because it suggests that the fluids responsible for creating the deposit contained a high concentration of sulfate ions. Quartz, which is another commonly occurring alteration mineral, is formed when hydrothermal fluids that are abundant in silica ions are deposited. This suggests that the fluids responsible for the formation of the deposit were both hot and acidic. Calcite and dolomite are minerals made of carbonate that are discovered in the rocks that contain Paleozoic carbonate-hosted barite deposits. These minerals can undergo changes caused by hydrothermal fluids that create barite, leading to the creation of other carbonate minerals such as smithsonite and celestite. Pyrite, a mineral containing sulfide, is frequently found alongside barite deposits. When hydrothermal fluids that create barite come into contact with pyrite, it can undergo oxidation. This process leads to the creation of other sulfide minerals such as marcasite and goethite.

The Kahramanmaraş region is a geographically significant area characterized by the convergence of two distinct tectonic plates, namely the Taurus plate and the Arabian plate. As a result, lithologies associated with these continents are observed in close proximity. The tectonic belts associated with the Arabian plate are typically situated in the southern region of Kahramanmaraş. The Dadağlı region, situated in the Kahramanmaraş province, holds significant importance within the marginal fold belt of the Arabian plate. The region exhibits exposure of sedimentary rocks from the Paleozoic era, carbonates from the Mesozoic era, and basalts from the Cenozoic era. The alluvium of Quaternary age is indicative of the most recent geological units. The region exhibits fault zones that generally trend in a northeast-southwest direction. Furthermore, it should be noted that the Gölbaşı-Türkoğlu segment of the Eastern Anatolia Fault is in close proximity to this particular region, and its presence has had a significant impact on the structural evolution within the area. The occurrence of barite mineralization can be observed in the Paleozoic-aged carbonates that are exposed in the northern region of Dadağlı. The mineralization that occurs within the fractures and cracks of carbonate rocks is classified as vein-type and epigenetic in nature. The ore structure frequently exhibits a lens-shaped morphology. The ore zone is observed within a spatial extent of 200 meters. The ore paragenesis is composed of various minerals, including barite, galenite, sphalerite, cerussite, smithsonite, goethite, pyrite, quartz, and calcite.

The geochemical analysis of the samples within the ore zone reveals that the concentration of BaO reaches a maximum value of 65.07%. The concentrations of SrO are observed to be low, while the concentrations of SiO_2 are comparatively high. The concentration of CaO ranges from 0.26% to 12.77% with an average of 2.88%, while the

---

[1] Corresponding author

concentration of Fe_2O_3 ranges from 0.12% to 15.97% with an average of 4.15%. The elevated Fe_2O_3 concentrations observed in certain barite specimens can be attributed to the existence of ferrous minerals, namely pyrite and goethite. The samples exhibit relatively low concentrations of Al_2O_3, MnO, Na_2O, K_2O, TiO_2, and P_2O_5, respectively

Carbonatization and sericitization are commonly observed in both field and microscopic studies of samples found near ore veins. A series of alteration geochemistry investigations were conducted with the objective of discerning the geochemical fluctuations within the studied area. The indices were computed for utilization in this research. The chlorite-carbonate-pyrite index (CCPI) values observed within the ore zone range from 21.41 to 96.90, with an average value of 72. Similarly, the chemical alteration index (CIA) values range from 4.69 to 78.22, with an average value of 21.03. Additionally, the alteration index (AI) values within the ore zone range from 7.56 to 84.63, with an average value of 24.49. The values upheld by the Central Intelligence Agency (CIA) are indicative of weathering that ranges from low to moderate. Based on the analysis of geochemistry diagrams and microscope examinations, it can be inferred that the prevalent types of alteration observed are carbonatization and albitization.

Keywords: Arabian plate, Barite, Paleozoic-aged, vein-type, Alteration Geochemistry, Dadağlı (Kahramanmaraş).

Rare earth element (REE) Indicators of Pertek Fe-Skarn formation

Cihan YALÇIN[1]

[1]General Directorate of Industrial Zones, Worldbank PIU, Ministry of Industry and Technology, Ankara, Türkiye.

Abstract

Skarn deposits represent geological formations that can manifest during different epochs and are characterized by a prevalence of minerals such as garnet and pyroxene. They typically form as a result of the interaction between carbonate rocks and igneous intrusions through processes such as contact and regional metamorphism, as well as metasomatism. The study of skarn formation necessitates the elucidation of various factors, including the inherent characteristics of the protolith rock, the chemical properties of the fluids involved, the temperature conditions during formation, and the potential involvement of magmatic processes. Data interpretation is facilitated through the utilization of both field and laboratory studies.

The most significant skarn deposits globally consist of iron (Fe) skarns primarily composed of magnetites, with potential trace amounts of copper (Cu), cobalt (Co), nickel (Ni), and gold (Au). The examination of Fe skarns and their genesis holds significant relevance within the mining industry. The Anatolian orogeny was initiated as a result of the subduction process involving the Paleo-Tethys and Neo-Tethys oceanic crusts. The Southeast Anatolian Orogenic Belt (SAOB) is a highly intricate component of the Alpine Himalayan system, situated in Southeastern Anatolia, between the Anatolid/Tauride Platform and the Arabian Platform.

The Pertek region, located in Tunceli, Turkey, is recognized as a significant area for Fe-Skarn mineralizations. The area is distinguished by the presence of Keban Metamorphites, which originated during the Permo-Carboniferous period. Additionally, metacarbonates, marbles, and schists are prevalent in the region. These rocks have been intersected by intrusive formations from the Upper Cretaceous Elazığ Magmatic Complex (EMC). The presence of tertiary volcanic rocks and sedimentary rocks can be observed to overlay both units, exhibiting an angular unconformity.

The Fe-Skarn mineralization occurred at the contact zone between the carbonate rocks of the Keban Metamorphites and the diorite rocks of the EMC. The examination of ore samples under a microscope allowed for the identification of magnetite crystals and garnet minerals, which were readily discernible based on their distinct coloration. The samples obtained from the Pertek Fe-Skarn formation exhibited elevated concentrations of major oxides, particularly with regards to Al_2O_3, which reached a concentration of 17.96%. This was observed specifically in samples where clayification is a prevalent process.

Rare Earth Elements (REEs) play a pivotal role in the identification and evaluation of Fe-Skarn deposits, which are mineral deposits formed through hydrothermal processes and known for their abundance of iron and calcium-rich minerals. The economic significance of these deposits lies in their potential for the production of valuable metals, such as iron, copper, zinc, gold, and silver. Rare earth elements (REEs) function as valuable indicators by providing insights into the distribution and patterns of specific REEs, including cerium, lanthanum, and europium. These elements exhibit notable variations that can be attributed to differences in partitioning mechanisms occurring during mineral formation and alteration processes.

---

[1] Corresponding author

The determination of the ratio between Light Rare Earth Elements (LREEs) and Heavy Rare Earth Elements (HREEs) can yield valuable information regarding the genesis of skarn deposits, facilitating the identification of hydrothermal fluids and their corresponding temperature and pH conditions by geologists. Gaining insight into the mobility of rare earth elements (REEs) within the deposit can provide valuable information regarding its alteration history, as these elements frequently exhibit mobility during alteration processes.

Skarn deposits frequently display zonation patterns in relation to rare earth elements (REEs), characterized by the presence of distinct zones that are either rich or poor in REEs. The utilization of the spatial distribution of rare earth elements (REEs) can facilitate the delineation of the internal configuration of the deposit and provide valuable guidance for exploration endeavors. Analytical methodologies such as inductively coupled plasma mass spectrometry (ICP-MS) and laser ablation inductively coupled plasma mass spectrometry (LA-ICP-MS) play a crucial role in the quantification of trace element concentrations in skarn samples.

Rare earth elements (REEs) can also function as pathfinder elements, serving as indicators for the existence of other economically significant metals that are commonly found in skarn deposits. Through the examination of the dispersion, arrangements, and proportions of rare earth elements (REEs), geologists are able to enhance their comprehension of the past events and mineralization mechanisms associated with these deposits. This, in turn, facilitates the advancement of exploration and resource evaluation endeavors.

The rare earth element (REE) compositions of the samples collected from both the ore and side rock in the field were analyzed using the inductively coupled plasma mass spectrometry (ICP-MS) technique. The ore and host rocks are generally poor in REE. The chondrite-normalized trace element distribution diagram demonstrates that light rare earth elements (LREE) display a higher degree of enrichment compared to heavy rare earth elements (HREE). The normalized distribution diagrams of the studied rocks reveal an enrichment of elements with a large ion radius (LIR), while elements with high field energy (HFEE) show a depletion. The results of the Rare Earth Element (REE) analyses do not indicate any significant enrichment in the Pertek Fe-Skarn deposit, thereby suggesting a unique and distinct nature of the deposit.

Keywords: REE, Skarn, Formation, vein-type, Permo-Carboniferous, Pertek (Türkiye).

Geochemistry - Isotope (Sr-Nd) properties of ulukale porphyric dome and çağlarca radial dykes and comparison with tunceli volcanics

Abdullah SAR[1] , Sevcan KÜRÜM [2], Muhammed Yasir YURT [3]

[1,2]Department of Geological Engineering, Engineering Faculty, Fırat University, Elazığ, Turkey.
[3]Cengiz Holding, Eti Bakır A.Ş., Adıyaman, Turkey

Abstract

In this study, the whole rock geochemistry, mineral chemistry and Sr-Nd isotope properties of the Ulukale (Çemişgezek-Tunceli) porphyric dome and Çağlarca (Hozat-Tunceli) radial dykes were compared with the Neogene Tunceli volcanics in which they are found. Stronge terrestrial volcanic activities have been active since the Miocene, especially in and around Tunceli. The volcanism around Çemişgezek, Pertek and Hozat (Tunceli) is also represented by effusive volcanism in the form of dykes and extrusive (lava domes / chimney plugs) products, especially explosive volcanism. Pyroclastic rocks, which are mostly products of explosive volcanism in the region and form a rather thick sequence, start with tuffs with intense pumice content. The density of pumices in the tuffs indicates that the magma forming the volcanism may be a more viscous/acidic magma, and these areas may also be important outlet centres. While the tuffs are generally not well compacted and therefore not resistant to surface conditions, the volcanic breccias that form thick stacks in the region are composed of gravel and blocks of very different grain sizes and shapes (from a few cm to m). In these volcanic breccias, pumice levels in places and layering with lava locally or in places to form pockets indicate intermittently repetitive volcanism. Basaltic-andesitic composition lavas, which are the last volcanic product in the region and form the top part of the succession, have formed a very rough and different surface-shaped terrain with the erosion of the unstable pyroclastics. Due to their compositional properties, these low-viscosity lavas with basic composition are found in a cover of a few meters or less in thickness. The fact that these basic composition lavas have firing zones at their contact with the tuffs indicates that the volcanism was active at different times. All rocks, identified to have trachy andesitic composition according to whole-rock chemical analysis, were determined to have similar high K calc-alkaline features or behaviour. Still, the magma forming the dome has a more acidic composition by mineral chemistry analysis. The SiO_2 values of the samples vary between 61.23-62.32%, except for one sample belonging to the dyke (Y-11 = 64.02% SiO_2). Generally, the samples from the porphyritic dome had regular distribution of variation in major element oxides and some trace elements with SiO2, while samples from the dykes had more irregular distribution. On the binary diagrams, all samples generally had a very regular distribution of K_2O, CaO, MgO, Fe_2O_3 and TiO_2, while there was a relatively irregular distribution in Na_2O and Al_2O_3. Similarly, while all samples showed a harmonious distribution in Ba, Rb and Y, the two dyke samples were more enriched in the Ba element at the maximum value, unlike the samples containing the same SiO_2. In the trace element distribution diagram normalized to the primitive mantle, examples of domes and dykes show similar characteristics. The fact that all samples are more enriched by light rare earth elements (LREEs) indicates that the magma is associated with active continental margin magmatism. However, in the diagram, the negative anomaly of the Nb, Ta and TiO_2 elements of the samples means that the subduction component is also effective in the formation of the main magma of these rocks. This situation occurs as the elements (LREE, Rb, Ba, Th, K) separated from the subducting plate during the subduction process are enriched in the mantle. The samples appear to have similar features to each other on trace element diagrams normalized to chondrite. The diagram shows more enrichment in heavy rare earth elements (HREEs) compared to LREE. The high LREE / HREE ratios in the samples suggest that

---

[1] Corresponding author

these rocks may have been formed by the effect of partial melting from a mantle source under the influence of subduction, consistent with the data in the diagram normalized to the primary mantle. Sr-Nd isotope analyses performed on each sample of domes and dykes are also similar. In the dome sample, the $^{87}\mathrm{Sr}/^{86}\mathrm{Sr}_{(i)}$ isotope ratio is 0.7064325, and the $^{143}\mathrm{Nd}/^{144}\mathrm{Nd}_{(i)}$ isotope ratio is 0.512516. The $^{87}\mathrm{Sr}/^{86}\mathrm{Sr}_{(i)}$ isotope ratio of the dyke sample is 0.706074, and the $^{143}\mathrm{Nd}/^{144}\mathrm{Nd}_{(i}$) isotope ratio is 0.512535. Similar isotope results indicate that these rocks may have originated from the same/similar magma or were formed through differentiation from the same/similar magma.

As a result, these volcanic rocks, which show similar geochemical features, show enriched mantle + lithospheric source characteristics at shallow depths. However, all geochemical analyses and Sr-Nd isotope analysis data revealed that magma mixing, the effect of continental crust in the form of contamination and the effect of sediment melts developed due to subduction are important in the formation of magma differentiation

Keywords: Tunceli volcanics, geochemistry, Sr-Nd isotope, lava dome, radial dyke

Catalytic degradation of metronidazole with Halloysite-Fe3O4-Ag nanocomposite and NaBH4

Türkan ALTUN[1], Hüseyin ECEVİT[2]

[1,2]Department of Chemical Engineering, Faculty of Engineering and Natural Sciences, Konya Technical University, Konya, Turkey

Abstract

Antibiotic residues in the environment are an important problem for the environment and public health, even at low concentrations, as they cause bacteria to develop antibiotic resistance. The main sources of antibiotic pollution are households, healthcare facilities, poultry and farm animals, and pharmaceutical manufacturers. Antibiotics mixed with wastewater from these sources can reach groundwater, soil and even drinking water. The ineffectiveness of conventional wastewater treatment methods for the removal of antibiotics necessitates studies to develop new technologies and methods in this field.

Metronidazole, a nitroimidazole class antibiotic, is a broad-spectrum agent that is widely used on both humans and animals, and is effective against many parasites. Due to its widespread use, metronidazole contributes to antibiotic pollution in water and soil.

For the removal of antibiotics, catalytic degradation processes are a remarkable approach, as they ensure that the pollutants are broken down and eliminated at the molecular level and do not form waste/sludge. As an alternative to advanced oxidation processes based on the formation of free radicals and the oxidation of pollutants by these radicals, $NaBH_4$ is a reducing reagent that can be used in the catalytic reduction of organic pollutants in the presence of metal nanoparticles. The surfaces of the nanoparticles used play an important role in the transfer of hydrogen from $NaBH_4$ to pollutant molecules by providing electron transfer.

Clays are materials that have the potential to show high catalytic efficiency thanks to the metals they contain in their structures, and high adsorption capacity thanks to their high surface areas. Thanks to these properties, they serve as a useful support material for composite catalysts to be formed by doping metals on their surface. Halloysite is a clay in alumina silicate structure naturally found in nanotube form and efficient results have been obtained in many studies on its use in the production of functional materials such as catalysts.

Although there are several studies in the literature in which organic pollutants are degraded using the $NaBH_4$ reagent, only four of these studies are on the removal of antibiotics. Of these four studies, only one targeted metronidazole removal.

In this study, the removal of metronidazole (MNZ) from the solution medium by catalytic degradation with $NaBH_4$ reagent was investigated. In the removal process, HNT-Fe_3O_4-Ag nanocomposite obtained by doping magnetite (Fe_3O_4) and silver nanoparticles to halloysite nanoclay activated by treatment with 0.1 M HCl was used as a catalyst. The removal of MNZ was investigated at different pHs by using the produced nanocomposite. Since the results obtained did not change much with pH, the natural pH value of 30 ppm MNZ solution was determined as 7, the optimum pH. In all MNZ removal trials, the removal efficiencies obtained as a result of three different processes, namely catalytic degradation, non-catalytic degradation and adsorption, were determined in Ct/C0 by measuring the MNZ concentration every 15 minutes depending on time (Ct: MNZ concentration at time t, C0: initial MNZ concentration). As this value approaches from 1 to 0, the removal efficiency increases. In the experiments, $NaBH_4$ reagent and HNT-Fe_3O_4-Ag nanocomposite were added to the MNZ solution in the catalytic degradation process, only $NaBH_4$ reagent was added in the catalyst-free degradation process and only HNT-Fe_3O_4-Ag nanocomposite was added as adsorbent in the adsorption process. In this way, the effects of all agents and processes used in removal have

---

[1] Corresponding author

been observed. As a result of the applied processes, after 120 minutes at pH 7, the Ct/C0 values were found to be 1.00 for the adsorption process, 0.77 for the catalyst-free degradation process and 0.07 for the catalytic degradation process (other parameters; MNZ concentration: 30 ppm, $NaBH_4$ concentration: 10 mM, nanocomposite dosage: 2 g/L). In all of these removal studies, the MNZ concentrations of the solutions were analyzed by measuring the light absorbance values of the solution samples at a wavelength of 318 nm with the help of a UV-visible spectrophotometer. In addition, since the HNT-Fe_3O_4-Ag nanocomposite is paramagnetic, a neodymium magnet was used to separate it from the solution. In this way, samples were taken from the MNZ solution, which was separated from the solid particles magnetically, at the end of the 15-minute contact time periods, and the MNZ concentrations were analyzed and the samples were added back into the mixture.

Together with the obtained HNT-Fe_3O_4-Ag nanocomposite, raw halloysite, HCl activated halloysite and Fe_3O_4 doped halloysite particles were analyzed by Fourier Transform Infrared Spectroscopy method and their chemical structures were characterized and it was revealed that iron and silver adhered to the halloysite surface as a result of nanocomposite formation processes.

Keywords: Degradation, antibiotic, metronidazole, halloysite, NaBH4, nanocomposite

A study on the removal of astrazon golden yellow dye molecules by chitosan-based magnetic field sensitive particles

Ömer İPEK[1], Şeyda TAŞAR[2], Fatih KAYA[3]

[1,2,3]Chemical Engineering Department, Engineering Faculty, Fırat University, Elaziğ, Turkey.

Abstract

Biodegradable, hydrophilic, renewable, and favorable to the environment, chitosan is a natural polymer. It is not harmful or toxic [1]. Three functional reactive groups make up chitosan; the C-2 position is occupied by an amino group, and the C-3 and C-6 positions, respectively, by primary and secondary hydroxyl groups [2]. Due to weak basic groups, chitosan is positively charged in contrast to other natural polymers. Chitosan can thus easily interact with negatively charged macromolecules, polyanions, and polymers. Due to its weak mechanical characteristics, low reusability, and ease of solubility in acids, natural chitosan has a limited range of applications [3]. However, these drawbacks can be overcome by applying physical or chemical modification procedures. The mechanical strength and sorption capacities of CS can be improved. It can be made physically and chemically modified to stop it from dissolving in strong acids. The physical modification method often involves blending CS or CS derivatives with other inorganic materials or transforming them into other forms such as porous particles, microspheres, gel particles, fibers, and films without altering the characteristics of CS [4]. In addition, it can enhance the kinetic sorption process or remove the challenge of solid-liquid separation after sorption thanks to the physical alterations of CS [5]. The most popular technique for enhancing the mechanical characteristics and structural stability of CS is cross-linking technology. Commonly used crosslinkers are tripolyphosphate (TPP) [3], glutaraldehyde (GLA) [6], epichlorohydrin (ECH) [7, 8], ethylene glycol diglycidyl ether (EGDE) [9], polyethylene glycol (PEG) [10]. These three-dimensional network structures made of linear CS molecules are challenging to dissolve in water. As a result, it is possible to create sorbents that can keep their chemical stability in acidic environments and broaden the sorption application range of CS adsorbents. In addition, both chitosan and particles made of chitosan have low specific gravities. Only centrifugation or filtering is used to extract CS adsorbents after sorption. This procedure is expensive and time-consuming. Magnetic CS particles are anticipated to find widespread use in the treatment of industrial wastewater because of their benefits of low cost, great sorption capacity, convenient separation, and superior stability.

The main aim of this study was to create chitosan-based and magnetic field-sensitive particle sorbents and assess their sorption effectiveness. The precipitation-collection approach was used to create chitosan-based polymeric particles and the produced particles were analyzed with SEM and FTIR methods. Then, wastewater that contained the reactive dyestuff (Astrazon golden yellow, AGY) was used to examine the sorption activities of chitosan-based polymeric particles. On the sorption effectiveness of dye molecules, the impact of different sorption parameters such as temperature, beginning pH, sorbent amount, initial dyestuff concentration, contact time, etc. was examined. The optimum sorption conditions were determined. Additionally, the ideal sorption conditions were found; the ideal solution temperature, beginning pH, chitosan concentration, contact time, and initial concentration of AGY dye were 25 °C, 7 ±0.02, 180 min, and 75 mg/L, respectively. The sorption capacities at 25, 30, 35, and 40 °C were 207.40, 293.35, 314.79, and 330.96 mg/g, respectively. Under the sorption conditions, the chitosan particles were seen to preserve their physical stability. It is thought that the sorbent produced with the epichlorohydrin crosslinker will likewise be effective at adsorbing sulfate ions and acidic dyes. Repeated the investigation using actual wastewater will help to more precisely identify the reactive dyestuff capabilities of the synthesized sorbent due to the complicated structure of textile wastewater, which comprises several pollutants. Furthermore, it is thought that the study be extended to the continuous system with the column system created using chitosan particle sorbents.

---

[1] Corresponding author

References

[1] Du, J., Tan, E., Kim, H.J., Zhang, A., Bhattacharya, R., Yarema, K.J., "Comparative evaluation of chitosan, cellulose acetate, and polyethersulfone nanofiber scaffolds for neural differentiation". Carbohydrate Polymers, 99,483-490, 2014.

[2] Youssef, A.M., Abou-Yousef, H., El-Sayed, SM, Kamel, S. "Mechanical and antibacterial properties of novel high-performance chitosan/nanocomposite films", International journal of biological macromolecules, 76,25-32, 2015.

[3] Ngah WS, Fatinathan S., "Adsorption characterization of Pb(II) and Cu(II) ions onto chitosan-tripolyphosphate beads: Kinetic, equilibrium and thermodynamic studies". J Environ Manage 91(4):958–969, 2010.

[4] Solisio C, Lodi A, Torre P, Converti A, Del Borghi M., "Copper removal by dry and rehydrated biomass of Spirulina platensis". Bioresour Technol 97(14):1756–1760, 2006.

[5] Song MH, Kim S, Reddy DH, Wei W, Bediako JK, Park S, Yun YS., "Development of polyethyleneimine-loaded core-shell chitosan hollow beads and their application for platinum recovery in sequential metal scavenging fll-and-draw process". J Hazard Mater 324(Pt B):724–731, 2017.

[6] Shankar P, Gomathi T, Vijayalakshmi K, Sudha PN., "Comparative studies on the removal of heavy metals ions onto cross linked chitosan-g-acrylonitrile copolymer". Int J Biol Macromol 67:180–188, 2014.

[7] Coelho TC, Laus R, Mangrich AS, de Fávere VT, Laranjeira MC., "Efect of heparin coating on epichlorohydrin cross-linked chitosan microspheres on the adsorption of copper (II) ions". React Funct Polym 67(5):468–75, 2007.

[8] Liu H, Yang F, Zheng Y, Kang J, Qu J, Chen JP., "Improvement of metal adsorption onto chitosan/Sargassum sp composite sorbent by an innovative ion-imprint technology". Water Res 45(1):145–154, 2011.

[9] Liu Y, Cao X, Hua R, Wang Y, Liu Y, Pang C, Wang Y., "Selective adsorption of uranyl ion on ion-imprinted chitosan/PVA cross-linked hydrogel". Hydrometallurgy 104(2):150–155, 2010.

[10] Reiad NA, Salam OEA, Abadir EF, Harraz FA., "Adsorptive removal of iron and manganese ions from aqueous solutions with microporous chitosan/polyethylene glycol blend membrane". J Environ Sci 24(8):1425–1432, 2012.

Keywords: Chitosan, gel particle, optimum sorption conditions, characterization

Adsorption of reactive yellow 3 dye molecules by nut shell based activated carbon

Elif KARDAŞ[1], Şeyda TAŞAR[2], Fatih KAYA[3], Neslihan DURANAY[4], Melek YILGIN[5]

[1,2,3,4,5]Chemical Engineering Department, Engineering Faculty, Fırat University, Elaziğ, Turkey

Abstract

Technologies used in the treatment of wastewater containing typical dyestuffs are divided into three groups. These; are chemical, biological, and physical processes. The adsorption process is the most preferable process for the treatment of dye molecules from industrial wastewater due to its simplicity, convenience of use, simple design, and ease of scaling up. It is also insensitive to dangerous compounds, has a high removal capacity, and has a good removal yield [1]. For many poor countries, the use of high-energy input processes such as reverse osmosis and UV degradation processes is impossible. Due to the high cost of photocatalyst synthesis and the high energy consumption of ultrasonic treatment, adsorption is preferred to these techniques. The adsorption process is the optimum treatment method for wastewater. Some of the most often used natural adsorbents are clay, silica, kraft lignin, fly ash, sludge, slag, and red mud. Commercially accessible adsorbents include activated carbon [2], activated alumina [3, 4], silica gel, and zeolites [5]. Aside from inorganic materials including clay, Fuller's earth, bentonite, lignite coal, peat, chitosan, and ion-exchange resin materials, agricultural residues and wastes such as sugarcane bagasse, rice brans, lignocellulosic biomasses, fruit stones, and nut hulls are also employed as adsorbents. In recent literature, novel adsorbent substances such as CNTs, MCM-41 [6, 7], and molecular sieves [7] have been found. Adsorbent selection is critical for the adsorption process. The adsorption capacity of the adsorbent material for a specific adsorbate heavily influences the choice of adsorbent. For this reason, the type of dye molecules is important. The reactive dyes that we discussed in this study are the dyestuffs that are commonly used in the dyeing process of cellulosic textile fibers such as cotton and linen [8, 9]. They have a strong binding affinity for cellulose. Studies have shown that if the adsorbents to be used during the removal of reactive dyes contain hydroxyl groups, the removal capacity is high [10]. The aim of this research was to investigate the adsorption of Reactive Yellow 3 (RY3) from aqueous solution by nut shell-based activated carbon (NSAC). For this purpose, first of all, nut shells were obtained from food commercial establishments, washed, dried, and ground. After the pre-treatment, the characterization of the sample was carried out with instrumental (FTIR, SEM, BET) and analytical methods (pHzpc). The adsorption study was carried out under batch conditions in a thermostatic water bath at 180 rpm shaking speed. Contact time (0-180 min), initial pH values (4-11), temperature (298-318 K), initial dye concentration (25-100 ppm), and sorbent dosage (0.1-0.4 g/L) effect) on the removal, efficiency was investigated. The optimum adsorption capacity was determined as 270 mg/g at 180 minutes, 7 ± 0.02, 318 K, 75 ppm initial dye concentration, and 0.25 mg/L adsorbent dosage. As a result, it was determined that by nutshell based activated carbon is an effective sorbent for the adsorption of RY3 dye molecules from the aqueous medium.

Reference

[1] Aragaw, T.A. Bogale, F.M. “Biomass-Based Adsorbents for Removal of Dyes From Wastewater: A Review”. Front. Environ. Sci. 9, 558, 2021.

[2] Zhu, S. Khan, M.A. Kameda, T. Xu, H. Wang, F. Xia, M. Yoshioka, T. “New insights into the capture performance and mechanism of hazardous metals Cr3+ and Cd2+ onto an effective layered double hydroxide based material”. J. Hazard. Mater. 426, 128062. 2022.

---

[1] Corresponding author

[3] Zhu, S. Chen, Y. Khan, M.A. Xu, H. Wang, F. Xia, M. “In-Depth Study of Heavy Metal Removal by an Etidronic Acid-Functionalized Layered Double Hydroxide”. ACS Appl. Mater. Interfaces 14, 7450–7463, 2022.

[4] Zhu, S. Khan, M.A. Wang, F. Bano, Z. Xia, M. “Exploration of adsorption mechanism of 2-phosphonobutane-1,2,4-tricarboxylic acid onto kaolinite and montmorillonite via batch experiment and theoretical studies”. J. Hazard. Mater. 403, 123810, 2021.[5] Yang, R.T. “Adsorbents: Fundamentals and Applications”; John Wiley & Sons: New York, NY, USA, ISBN 9780471297413, 2003.

[6] Rouquerol, J. Sing, K.S.W. “Adsorption by Powders and Porous Solids: Principles, Methodology And Applications”, Academic Press: San Diego, CA, USA, 1999.

[7] Lam, K.F. Yeung, K.L. McKay, G. “A rational approach in the design of mesoporous adsorbents”. Langmuir, 22, 9632–9641, 2006.

[8] Al-Degs, Y. Khraisheh MA, Allen M., Ahmad, S.J. Ahmad M.N. “Effect of carbon surface chemistry on the removal of reactive dyes from textile effluent”. Water Res. 34, 927–935, 2000.

[9] Al-Degs, Y.S. El-Barghouthi, M.I. El-Sheikh, A.H. Walker, G.M. “Effect of solution pH, ionic strength, and temperature on adsorption behavior of reactive dyes on activated carbon”. Dye. Pigment. 77, 16–23, 2008.

[10] Chiou, M.S. Kuo, W.S. Li, H.Y. “Removal of Reactive Dye from Wastewater by Adsorption Using ECH Cross-Linked Chitosan Beads as Medium”. J. Environ. Sci. Heal. Part A 38, 2621–2631, 2007.

Keywords: Nut shell, activated carbon, adsorption, Reactive Yellow 3, Characterization

Sorption of basic blue 3 dye molecules by chitosan based sorbent

Gizem ÖZER[1], Şeyda TAŞAR[2], Fatih KAYA[3], Melek YILGIN[4], Neslihan DURANAY[5]

[1,2,3,4,5]Chemical Engineering Department, Engineering Faculty, Fırat University, Elaziğ, Turkey.

Abstract

Today, many industrial production processes, especially in the textile, food, beverage, pharmaceutical processing, printing, paper, and pulp production sectors, cause pollution in the receiving environment due to inadequate processing of wastes [1]. Wastewater discharged into the receiving environment poses a serious threat to human and animal health, as well as to plant and aquatic ecosystems. It has been proven that some dye molecules significantly affect especially human health, especially on the skin, kidneys, liver, reproductive system, heart, brain, and nervous system, and some of them cause cancer types and mutations [2, 3]. In addition to the toxic effects of dyes, the decrease in photosynthetic activities caused by the limitation of light transmission in the aquatic ecosystem causes great damage to the aquatic ecosystem [4]. It is also known that the dye molecules in wastewater consume the dissolved oxygen concentration in the water during the degradation process, reducing the water quality. This situation affects negatives the health reproduction trend of fish and aquatic organisms [6]. Although the production and discharge data of wastewater containing dyestuff contamination are not accurately recorded worldwide, according to current industry figures, more than 11,000 dye pigments are used in the food, textile, cosmetics, leather, paper, and plastic industries. And the global dyestuff produced annually is 1.8-1.9×106 tons [6]. According to the structure and characteristics of the production sector, 1-10% of this dyestuff occurs as waste which means that it is discharged into natural water resources [7]. Considering the amount of wastewater and its effect on the ecosystem, it is understood that dyestuff molecules must be treated before being discharged into the aquatic environment. Although there are different treatment methods, the most functional and advantageous method is still the adsorption method today[8-10]. In this study, the removal of Basic Blue 3, which is a reactive dye, from the aqueous medium by using chitosan-based sorbent. The precipitation-collection approach was used to create chitosan-based polymeric particles and the produced particles were analyzed with SEM and FTIR methods. Then, wastewater that contained the reactive dyestuff (Basic Blue 3, BB3) was used to examine the sorption activities of chitosan-based sorbent. On the sorption effectiveness of dye molecules, the impact of different sorption parameters such as temperature, initial pH, sorbent dosage, initial dye solution concentration, contact time, etc. were examined. The optimum sorption capacity of sorbent was determined as 67.41 mg/g. The optimum solution temperature, initial pH, chitosan concentration, contact time, and initial concentration of BB3 dye were 298 K, 10.5 ±0.02, 240 min, 1 g/L, and 150 mg/L, respectively. Under the sorption conditions, the chitosan particles were seen to preserve their physical stability. Repeated the investigation using actual wastewater will help to more precisely identify the dyestuff sorption capabilities of the synthesized sorbent.

Reference

[1] Akakuru, O.U. Iqbal, Z.M. Wu, A. TiO2 Nanoparticles Properties and Applications. In TiO2 Nanoparticles: Applications in Nanobiotechnology and Nanomedicine; John Wiley & Sons, Ltd.: Weinhein, Germany, pp. 1–66. ISBN 9783527825448, 2020.

[2] Oyewo, O.A. Elemike, E.E. Onwudiwe, D.C. Onyango, M.S. “Metal oxide-cellulose nanocomposites for the removal of toxic metals and dyes from wastewater”. Int. J. Biol. Macromol. 164, 2477–2496, 2020.

[3] Zhu, S. Xia, M. Chu, Y. Khan, M.A. Lei, W. Wang, F. Muhmood, T. Wang, A. “Adsorption and Desorption of Pb(II) on l-Lysine Modified Montmorillonite and the simulation of Interlayer Structure”. Appl. Clay Sci. 169, 40–47, 2019.

[4] Khan, S. Malik, A. “Toxicity evaluation of textile effluents and role of native soil bacterium in biodegradation of a textile dye”. Environ. Sci. Pollut. Res. 25, 4446–4458, 2018.

---

[1] Corresponding author

[5] Kishor, R. Purchase, D. Saratale, G.D. Saratale, R.G. Ferreira, L.F.R. Bilal, M. Chandra, R. Bharagava, R.N. "Ecotoxicological and health concerns of persistent coloring pollutants of textile industry wastewater and treatment approaches for environmental safety". J. Environ. Chem. Eng. 9, 105012, 2021.

[6] McKay, G. Parthasarathy, P. Sajjad, S. Saleem, J. Alherbawi, M. Dye removal using biochars. In Sustainable Biochar for Water and Wastewater Treatment; Mohan, D., Pittman, C.U., E.Mlsna, T., Eds.; Elsevier: Amsterdam, The Netherlands, pp. 429–471, 2022.

[7] Velusamy, S. Roy, A. Sundaram, S. Kumar Mallick, T. "A Review on Heavy Metal Ions and Containing Dyes Removal Through Graphene Oxide-Based Adsorption Strategies for Textile Wastewater" Treatment. Chem. Rec. 21, 1570–1610, 2021.

[8] Aragaw, T.A. Bogale, F.M. "Biomass-Based Adsorbents for Removal of Dyes From Wastewater: A Review". Front. Environ. Sci. 9, 558, 2021.

[9] Zhu, S. Khan, M.A. Kameda, T. Xu, H. Wang, F. Xia, M. Yoshioka, T. "New insights into the capture performance and mechanism of hazardous metals Cr3+ and Cd2+ onto an effective layered double hydroxide based material". J. Hazard. Mater. 2022, 426, 128062.

[10] Zhu, S. Chen, Y. Khan, M.A. Xu, H. Wang, F. Xia, M. "In-Depth Study of Heavy Metal Removal by an Etidronic Acid-Functionalized Layered Double Hydroxide". ACS Appl. Mater. Interfaces 14, 7450–7463, 2022.

Keywords: Chitosan based sorbent, Basic Blue 3, Optimum sorption conditions, Characterization

Waste plastic degradation by chemical recycling method

Adil KOÇ[1]

[1]Department of Chemical Engineering, İnönü University, Malatya, Türkiye.

Abstract

In our days, plastics have a major part for social and evolution life and their wastes cause enormous economic source loses. So they have been carried out some degradation techniques such as thermal and catalytic degradation. The major of using waste plastics are PE, PP, PS, PET and PVC and their derivative products, which they have named thermoplastics. Because of fuel like or petrochemical feedstock products could be produced, the waste plastic degradation works are important reusing methods. The original and waste form of some plastics, such as PP, PE, PS have decomposed [1, 2] and found especially in alkene/alkane ratio has important factor for plastic mixture degradation in addition to the found that the PS amount in the mixture has increased the reaction rate coefficient. Low density polyethylene (LDPE) plastic which is a major product within plastics and formed a high amount of waste, was chemical degraded in thermally and catalytical in air media. And it was reported that the oxygenated compounds obtained in the oxidative thermal pyrolysis experiments using air were approximately 85% more than the oxygenated products obtained in the catalytic environment [3].

PE's which they have specific properties such as high resistance (chemical and mechanical), easy machinable, low specific gravity and cost so it produced more than another plastics, such PP, PS, PET and PVC, and so this causes very amount waste PE plastic [3-6]. For the purpose of production like petrochemical feedstock products, an experimental work, [7], has studied and found the reaction products (hydrocarbons mixture) separated considering to molecular weight and this hydrocarbon mixture products can not be solvable in water. Different researches, [8, 10], have done about waste plastic (oxygenic and non oxygen including polymers) degradation by thermogravimetric method and thermal degradation reactor, where it has different parts.

In our study, Poliethylene (PE) and PP plastics selected original and waste form for thermal and catalytic chemical degradation process. The process parameters have been chosen at 400–450 oC temperature range and in presence of 600 mL/min nitrogen gas flow rate. On the verge of using for experimental works, as Co and Mo catalysts were supported on silica (SiO2) material and prepared at different weight ratios. To prepare for Mo catalyst, ammonium molybdate tetra hydrate, and for preparing of Co catalyst, cobalt-2-nitrate hexa hydrate salts were used respectively. For different ratios of catalysts preparation just any salt has dissolved in distilled water and then support material was added to this solution. This liquid-solid solution has been kept waiting at room temperature about at 36 hours and the water smashed then it calcined at various temperatures.

In this study, the original and waste form of Low Density Polyethylene and Polypropylene samples have been decomposed at atmospheric pressure in a horizontal cylindrical ceramic oven. At the end of the experiments, the out of reactor, vapor of pyrolyzed plastic product were liquifed in the ice-salt bath and destilled. And we saw that the distillation ranges have been changed with catalyst/plastic ratios. These liquid products were analysed using an Agilent 19091N-13 HP-INNOWAX GC/MS apparatus with a 60 m capillary column containing 5 % diphenyl and 95% diphenyl polysiloxane. The GC/MS analyses products likes saturated and unsaturated hydrocarbons such as nonan, undecan, hepten, dodecen, eicosen. Also we found by calorimetric method that the pyrolysis products have very high caloric value 10.088 cal/g and so we said that these products can be use in combustion technology as fuels.

Keywords: Catalytic chemical reuse, waste plastic,

---

[1] Corresponding author

Biosorption of basic yellow 51 (BY51) molecules by mussel shell from the wastewater

Şermin DENİZ[1], Şeyda TAŞAR[2], Fatih KAYA[3], Filiz KAR[4]

[1,2,3,4]Chemical Engineering Department, Engineering Faculty, Fırat University, Elaziğ, Turkey.

Abstract

High levels of color pigments, organic compounds, and salt forms are present in the water after the conclusion of the coloring process, which is employed in the leather, paper, textile, plastic, and paint industries. Widespreadly used dye pigments have a complicated structure, a slow rate of spoilage, and carcinogenic properties [1]. Its harmful effects on people and other living things have been demonstrated. These and similar dyestuffs pose harm to aquatic life, impair water clarity, cause eutrophication, and cause anaerobic conditions when wastewater containing them is released into the ecosystem that is receiving it (lake, stream, river, etc.) [2, 3]. The dyestuff-containing wastewater needs to be appropriately treated before being released into the receiving environment. Methods have been developed under three main groups (chemical, biological, and physical) processes in the treatment of dyestuff-containing wastewater such as reverse osmosis, UV degradation process, membrane filtration, etc. However, most of these methods have significant disadvantages. For many poor countries, the use of high-energy input processes such as reverse osmosis and UV degradation processes is impossible. The high cost of photocatalyst synthesis and the high energy consumption of ultrasonic treatment, the sorption process is preferred to more than these techniques. They are not very practical for usage in small-scale companies due to their relatively high costs. Because, biosorption is less expensive and more advantageous than other traditional technologies and as a result, it has recently become one of the most popular techniques for the removal of dye molecules [4,5]. However, two factors (the maximum absorption capacity of the sorbent and its regeneration and reuse capacity) are crucial for the efficiency and economy of the biosorption process. These parameters are the maximum sorption capability of the sorbent and the ability to regenerate properties and reuse the sorbent. Natural sorbents and waste biomass-based activated carbon are the most suitable sorbents to remove color molecules from wastewater [6, 7]. Therefore in this study, a mussel shell was used biosorbent. Most of Turkey's coastal regions raise or gather blue mussels (Mytilus galloprovincialis) for human consumption. Turkey produced between 9000 and 59000 tons of mussels per year from 2000 to 2016. Throughout this time, the volume of blue mussels increased to 12000 tons per year from 78 tons per year. The shell percentages of mussels were between the ratio of 52 and 61%. Turkey produces between 4500 to 28000 tons of mussel shells garbage each year. The organic matrix (aragonite, calcite, or in some situations, vaterite) made up 1-5% of the weight of the mussel shell. The shell's other parts contain calcium carbonate [8-10]. In this study, the removal of Basic Yellow 51 (BY51), which is a reactive dye, from the aqueous medium by using mussel shells was investigated. For this purpose, first of all, natural mussel shells (single type, same type) were obtained from food commercial establishments, washed, dried, and ground. After the pre-treatment, the characterization of the sample was carried out with instrumental (FTIR, SEM, BET) and analytical methods (pHzpc). The biosorption study was carried out under batch conditions (in a thermostatic water bath at 180 rpm shaking speed). The effects of biosorption conditions (contact time (0-180 min), initial pH values (2.5-8.5), temperature (298-328 K), and initial dye concentration (50-150 mg/day)) on removal efficiency were determined. The maximum adsorption yield was determined as % 97 at optimum conditions. As a result, it was determined that mussel shells are an effective sorbent for the biosorption of BY51 dye molecules from the aqueous medium.

---

[1] Corresponding author

Reference

[1] Akakuru, O.U. Iqbal, Z.M. Wu, A. “TiO2 Nanoparticles Properties and Applications. In TiO2 Nanoparticles: Applications in Nanobiotechnology and Nanomedicine”; John Wiley & Sons, Ltd.: Weinhein, Germany, 1–66. ISBN 9783527825448, 2020.

[2] Oyewo, O.A. Elemike, E.E. Onwudiwe, D.C. Onyango, M.S. “Metal oxide-cellulose nanocomposites for the removal of toxic metals and dyes from wastewater”. Int. J. Biol. Macromol. 164, 2477–2496, 2020.

[3] Zhu, S. Xia, M. Chu, Y. Khan, M.A. Lei, W. Wang, F. Muhmood, T. Wang, A. “Adsorption and Desorption of Pb(II) on l-Lysine Modified Montmorillonite and the simulation of Interlayer Structure”. Appl. Clay Sci. 169, 40–47, 2019.

[4] Aragaw, T.A. Bogale, F.M. “Biomass-Based Adsorbents for Removal of Dyes From Wastewater: A Review”. Front. Environ. Sci. 9, 558, 2021.

[5] Zhu, S. Khan, M.A. Kameda, T. Xu, H. Wang, F. Xia, M. Yoshioka, T. “New insights into the capture performance and mechanism of hazardous metals Cr3+ and Cd2+ onto an effective layered double hydroxide based material”. J. Hazard. Mater. 426, 128062, 2022.

[6] Al-Degs, Y. Khraisheh MA, Allen, S.J. Ahmad, M.N. “Ahmad Effect of carbon surface chemistry on the removal of reactive dyes from textile effluent”. Water Res. 34, 927–935, 2000.

[7] Al-Degs, Y.S. El-Barghouthi, M.I. El-Sheikh, A.H. Walker, G.M. “Effect of solution pH, ionic strength, and temperature on adsorption behavior of reactive dyes on activated carbon”. Dye. Pigment. 77, 16–23, 2008.

[8] Barros, M.C., Bello, P.M., Bao, M., Torrado, J.J. “From waste to commodity: transforming shells into high purity calcium carbonate”. Journal of Cleaner Production 17, 400-407, 2009.

[9] Fuentes, A., Fernandez-Segovia, I., Escriche, I., Serra, J.A., “Comparison of physico-chemical parameters and composition of mussels (Mytilus galloprovincialis Lmk.) from different Spanish origins”. Food Chemistry 112, 295-302, 2009.

[10] Marin, F., Luquet, G., Molluscan shell proteins. Comptes Rendus Palevol 3, 469-492, 2004.

Keywords: Mussel shell, Biosorption, Basic Yellow 51, Characterization

Production of nanoparticles from almond shells by green synthesis method and investigation of their antioxidant properties

Buket ERZEN[1], Mukaddes KARATAŞ[2], Ercan AYDOĞMUŞ[3]

[1,2,3]Department of Chemical Engineering, Faculty of Engineering, Fırat University, 23119, Elazığ, Türkiye.

Abstract

Recently, green synthesis has gained importance over other physical and chemical methods, since; it offers environmentally friendly, cheap, biocompatible, shape, and size-controlled nanoparticles. The key aspect of nanotechnology is primarily aimed at the development of suitable and reliable synthesis routes, which in turn govern the size and shape, chemical composition, and large-scale production with better mono-dispersion for the synthesis of nanomaterials. Various synthesis methods are available in literature including green routes based on using plants, bacteria, and fungi, and they are given importance because of their non-toxic, economical, and eco-friendly method of preparation and bio-compatible nature. Also, AgNPs prepared by using the above-mentioned methods do not/less use a toxic chemical, which makes them to be used in medical and pharmaceutical applications. Green synthesis of nanoparticles involves the use of plant or plant parts for the bio-reduction of metal ions into their elemental form in the size range of 1–100 nm. The process of green synthesis is more efficient, simpler, and economical, and can easily be scaled up to perform larger operations.

In this study, nanoparticles were produced by the green synthesis method by evaluating agricultural wastes. The change in the antioxidant capacity of the resulting nanoparticles was examined. The green synthesis method was preferred because it is a simple, environmentally friendly, and cost-effective method compared to traditional physical and chemical methods various phytochemicals found in plants are obtained from the leaves, roots, and stems of plants and can show potential reducing properties in the presence of metal salts. Among them, noble metal nanoparticles, such as Ag, Au, Pt, and Pd nanoparticles are used in physical, chemical, and biological applications. AgNPs represent a good candidate to carry out the nanostructured part of antioxidant antibacterial and anticancer applications. The properties of the nanomaterials are controlled by their shape, size, and nature. AgNPs are highly in demand, because of their various applications in medicine, water treatment, and catalysis. In general, colloidal dispersions lead to the formation of AgNPs and their morphology differs, based on the methods adopted for the synthesis. Silver nanoparticles have a wide range of uses due to their electrical, optical, thermal, and antibacterial properties. For example, it is used in many areas such as water and wastewater treatment, production of antibacterial materials in the biomedical field, and increasing conductivity in electronic materials. Antioxidants that improve health in general have a strengthening effect on the immune system. In addition, antioxidants, which reduce oxidative stress by neutralizing free radicals, help prevent DNA damage that may occur in cells. Antioxidants (AO) protect food quality by preventing oxidative degradation of lipids, an essential ingredient of the diet. Phenolic compounds and some of their types are very effective in preventing autoxidation. All flavonoids have antioxidant activity with their 3-4 dihydroxy configurations. In addition to the functions of flavonoids and other plant phenolic in scavenging radicals such as superoxide, alkoxyl, peroxyl, and nitric oxide, iron and copper chelation, and µ-tocopherol regeneration. It also has vasodilator, immune stimulant, antiallergic, estrogenic and antiviral effects. Antioxidant capacity is a measure of a specific free radical scavenged by a test solution. DPPH (2,2-diphenyl-1-picrylhydrazyl) is a commercially available stable organic nitrogen radical. DPPH radical scavenging ability is determined mostly in organic solvents such as methanol or ethanol by measuring the absorbance drop at 517 nm. The use of methanol is not preferred because of its toxic properties. Analyses were performed with a UV-vis spectrophotometer in 1 mL or 3 mL cuvettes. The displacement of a free electron in the molecule causes the color

---

[1] Corresponding author

violet. When the DPPH solution is mixed with a substance (antioxidant) that can donate hydrogen atoms, a reduced form is formed with the loss of dark violet color.

To this end; Almond shell, an organic waste, was used. Almond shells were obtained from the chemical engineering department laboratory of Fırat University. The almond shells were washed 3 times with tap water and then washed with pure water. The washed almond shells were dried in an oven at 60 °C for 2 days. The dried almond shells were ground in a blade grinder at high speed until they became powder. Then, the aqueous solution of the ground almond shells was prepared and the almond extract was obtained. Nanoparticle production was achieved by reacting almond extract with silver nitrate solution. Nanoparticle characterization was done with the particle sizer device. The antioxidant capacity of the obtained nanoparticles was examined by the DPPH (2,2-diphenyl-1-picrylhydrazyl) method. As a result, silver nanoparticles (AgNPs) below 100 nm were successfully obtained and a significant increase in antioxidant capacity was observed. Figure 1 shows the experimental nanoparticle production scheme.

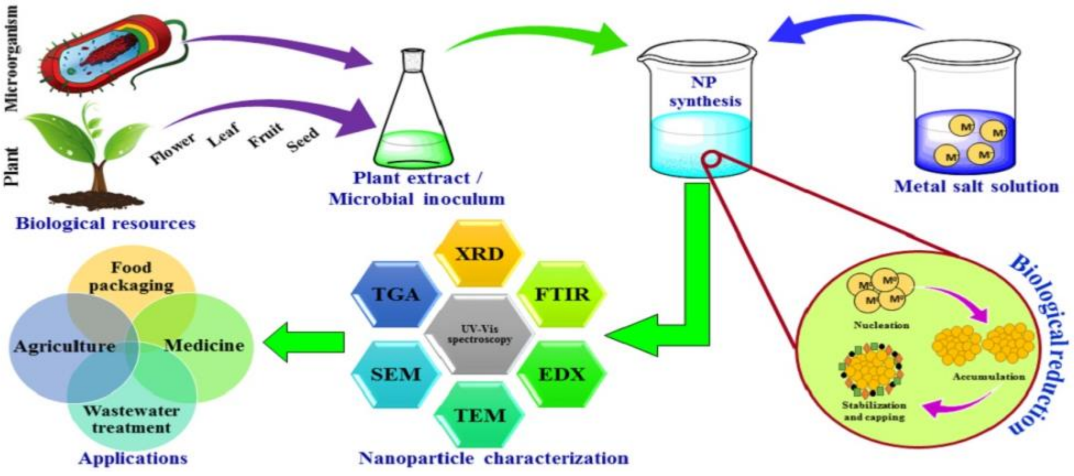

Figure 1. Nanoparticle production scheme and characterization steps by green synthesis

Keywords: Green synthesis, almond shell, nanoparticle, DPPH(2,2-diphenyl-1-picrylhydrazyl).

International Conference on Advances and Innovations in Engineering

International Conference on Advances and Innovations in Engineering
2ICAIE

Design of a control system for temperature-moisture parameters in a greenhouse dryer and modeling of these parameters with machine learning algorithms

Mert ÇEÇEN[1], Mehmet DAŞ[2], Ebru AKPINAR[3]

[1]Computer Engineering Department, Engineering Faculty, Fırat University, Elazig, Türkiye.
[2,3]Mechatnical Engineering Department, Engineering Faculty, Fırat University, Elazig, Türkiye.

Abstract

Drying is the most effective and simple method to extend the consumption life of manufactured products. Drying is the removal of the liquid in a substance. Drying is defined as the reduction of the product to the desired dryness value by removing the moisture of the product to be dried. An important problem of drying under the sun is the slow drying time compared to other drying processes. Dust, soil, rain, microorganism growth, various insects and animals circulating in the exhibition places, and unstable meteorological conditions during the drying season negatively affect the product quality in open exhibition drying by utilizing solar energy. Therefore, it is necessary to dry under controlled conditions. Various systems have been developed for the use of solar-heated air in drying. Cabin, tent, greenhouse, tunnel-type solar dryers, and air solar collector dryers are the most common systems. In today's conditions where agricultural product production policies are becoming increasingly important, the use of greenhouse systems that provide 4 seasonal vegetable and fruit production is becoming increasingly widespread. With the automation systems prepared for greenhouse systems, the optimum thermophysical properties of each product can be obtained in the greenhouse air. Temperature, weight, and energy-controlled systems are becoming increasingly common in greenhouse systems. Many parameters were measured in greenhouse drying systems and system control was realized according to these parameters. Thanks to these control systems, greenhouse air control was realized and the drying time and quality of the grown product were increased. In this study, a product weight control scenario was implemented for a greenhouse dryer and forced air convection was realized by automatically turning on the fan in the greenhouse when the product weight drops below 40 g. A greenhouse measuring 1800 x 1200 x 500 mm was used in this study. The greenhouse used was previously purchased with the 2209 Tübitak Project No. 1919B012107893. The weight and temperature control unit placed in the greenhouse was provided by the 2209 Tübitak Project No. 1919B012210188, which supports the current study. In the system, 1 load cell for weight control, 1 pt-100 temperature sensor, 1 on-off control circuit to activate the circulation fan, and an Arduino Nano board as a microcontroller was used. Predictive models were developed for the product moisture content values obtained in the experiments with the help of artificial intelligence methods. Artificial neural networks and support vector machine methods were used as artificial intelligence methods. Predictive models were created using ANN and SVM for the moisture content values of the product dried in the greenhouse. Root mean squared error (RMSE) analyses were performed to determine the accuracy of these models. A predictive model was created with a 3-layer artificial neural network (ANN) using Logsig Activation function and Backpropagation learning function for moisture content values obtained from experiments. The aim of this study is to realize faster and more effective drying by controlling the product drying process in a portable greenhouse dryer. For this purpose, product weight values were controlled. According to the set values, forced air convection was obtained with the help of a fan in the greenhouse. In this study, two different experiments were carried out in a greenhouse dryer. In experiment 1, standard product drying was performed without weight control. In the 2nd experiment, the product weight was controlled and drying was carried out by activating the fan in the greenhouse. The experiments were carried out using products with an initial weight of 80 g. When the final weight of 20 g was reached, the experiments were terminated.

---

[1] Corresponding author

It was shown that the drying performance of the greenhouse solar energy-assisted dryer in food drying systems increased with the addition of a weight-controlled system. The drying time was 48 minutes earlier with the weight control system. Then, the product wet base moisture content value (MC wet) in the experiments was modeled with ANN and SVM artificial intelligence methods, and the model with the least error (0.531 RMSE) was created using the ANN method. The RMSE error value of the predictive models made with the SVM method for product wet base moisture content values is 0.0599. This error value is higher than the error value of the model created with the ANN method. At the end of the study, itwas concluded that weight- controlled drying reduced drying time and two different machine learning algorithms successfully predicted product moisture content values. More data can be obtained by drying different products other than peach in the greenhouse dryer and more successful predictive models can be created by using different computational intelligence methods.

Keywords: Artificial neural network, machine learning algorithms, moisture and temperature control, multiple linear regression, solar greenhouse dryer,

Parametric optimization of fracture resistance of multilayer 3D printed parts

Erman ZURNACI[1]

[1]Department of Mechanical Engineering, Faculty of Engineering and Architecture, Kastamonu University, Kastamonu, Turkey.

Abstract

Introduction

Technological advances have made it possible to develop faster and lower-cost production techniques. Additive Manufacturing to the production of plastic filaments that are melted at a high temperature and added in layers using an extruder that moves three axes in accordance with predetermined coordinates. Fused Deposition Method (FDM), one of the Additive Manufacturing techniques, is a fast and effective technique that is frequently used in the production of components belonging to many different engineering branches, from the defense industry to the aviation industry. One of the most important features of this technique is that the production parameters that affect the mechanical properties and quality of the product can be configured and the production cost is low. In production using this technique, waste raw material formation is almost non-existent, which minimizes negative environmental impacts. In addition, complex geometries and structures that are difficult to produce with traditional methods can be easily produced with FDM technology.

There are many production parameters in the FDM technique, and the effect of these parameters on production quality is still being investigated by researchers. Many parameters, from production materials to production speed, affect product quality. In this study; the effect of production parameters of multi-layered components on the fracture resistance and filament consumption was examined. Optimum production parameters were determined by determining the statistical relationship between production parameters and fracture toughness, absorbed energy and filament consumption. It is aimed to determine a road map for the production of components with improved mechanical properties with less raw material consumption.

Materials and Methods

In this study, infill pattern (quick 2D infill, strong 2D infill and strong 3D infill), infill density and hotend temperature were determined as production parameters. Taguchi experimental design method was carried out using different levels of production parameters. 3D models of the test samples were created using Solidworks software with dimensions of 125x12.7x5 mm in accordance with the ASTM D6110 standard. Sample 3D models were converted in STL format. Multilayer production G codes were created for the production parameters determined in the experimental design of the models transferred to the Ultimaker Cura software. Three-dimensional printing of the experimental samples was carried out using a Creality Ender 3 S1 brand 3D printer with 1.75 mm diameter polyactic acid (PLA) filament material. Production was carried out with a 0.4 mm diameter nozzle at a bed temperature of 70 °C and a printing speed of 60 mm/s. All samples were produced with the same filament and kept at room conditions for at least 12 hours after production. The filament consumption amount for each sample was provided by the Ultimaker Cura software. Three experimental test samples were produced for each test to ensure measurement accuracy.

---

[1] Corresponding author

Fracture tests of the produced samples were carried out according to the Charpy test method on the Hardway JBW 300B device located in Kastamonu University Central Research Laboratory. A hammer of 150 J impact was used in the impact testing. Machine and specimen setup was made as per ASTM test procedure. After the test, the fracture resistance of the tested samples and the amount of absorbed energy were recorded by the computer connected to the testing device. Each test was repeated three times and the average of the measurement results was calculated.

Response Surface Method is a technique that allows optimizing responses (dependent variables) with two or more quantitative factors (independent variables). In this study, it was used to determine the relationship between experimental test results and production parameters and to optimize.

Results and Conclusions

In the optimization process production parameters as factors; fracture resistance, absorbed energy and filament consumption were modeled as responses. In optimizing the response variables, a maximized objective function was used for fracture resistance and absorbed energy, and a minimized objective function was used for filament consumption. Analyzes of variance were performed for each response variable. Additionally, first-order and interactive regression equations were created for each factor. As a result of variance analysis, the most effective factor on the three response variables was calculated as infill density. Hotend temperature was determined as the least effective production parameter on the response variables.

The Response Optimizer tool calculated that in order to optimize the responses, the infill density should be 20%, the hotend temperature should be 212.7º and the infill pattern should be strong 3D. Additionally, in case of selection of these factor values, the estimated value of the response variables was calculated. While the Composite Desirability value of the optimization was calculated as 0.62, the desirability value of the fracture resistance response was calculated as 0.45, the desirability value of the absorbed energy response was calculated as 0.55, and the desirability value of the filament consumption response was calculated as 99%. In order to reduce the filament consumption value in optimization, the desirability values of the responses were determined low.

Keywords: 3d printid component, multilayared component, fracture resistance, optimization

Production of ferric-phosphate for application in the lithium battery industry

Dragana Bozic[1], Radmila Markovic[2], Ljiljana Avramovic[3], Zoran Stevanovic[4], Dejan Bugarin[5]

[1,2,3,4,5]Mining and Metallurgy Institute Bor, Bor, Serbia

Abstract

This paper presents the results of research with the aim of conquering a new technology for obtaining ferric phosphate for use in the production of lithium batteries. A lithium iron phosphate battery is a type of lithium-ion battery that has cathode materials made of lithium iron phosphate. LiFePO4 has many advantages over other lithium-ion battery designs and older lead acid (LA) batteries. They weigh less, do not require maintenance, have better charging and discharging characteristics and a much longer lifespan. Other key advantages of LiFePO4 include high amperage, longer cycle life, zero leakage and fire hazards, tolerance to sub-optimal charge and discharge cycles. Battery charging times for LiFePO4 batteries are faster than for lead acid or other lithium batteries, typically LiFePO4 units have four times the energy density and charge five times faster than lead acid batteries. The life of a LiFePO4 battery is up to five times longer than some lithium-ion batteries, often reaching up to 5000 cycles without significant performance degradation. Unlike lithium and lead-acid batteries, LiFePO4 batteries do not contain toxic, heavy or rare earth metals such as cobalt, nickel or lead. LiFePO4 consists of common materials such as graphite, iron and copper. Thus, lithium-iron-phosphate batteries are more environmentally friendly to manufacture, but also pose a much lower risk to the environment during their lifetime compared to other lithium batteries. Since the desirable characteristics of iron phosphate precursors for LFP synthesis for batteries are often different or conflict with those for other uses, the existing chemical market is an impractical source for iron phosphate precursors for LFP synthesis. In addition, iron phosphate from commercial sources synthesized by the existing method often contains impurities, for example, sulfates, chlorides, and nitrates, which are harmful to lithium-ion batteries. Moreover, different batches of commercially available iron phosphate material often have inconsistent properties. Therefore, there remains a need to develop a new technology to produce highly pure iron phosphate with consistent and desirable properties for the synthesis of LFP for batteries.

The solid residue obtained during the processing of non-standard jarosite-PbAg precipitate from the zinc production process in Elixir, Šabac was used as the starting material. In order to separate Fe from Cu, Zn, In and other useful and highly valuable components, detailed laboratory tests of the combined procedure, which includes roasting of jarosite PbAg sediment and leaching of the resulting product, were performed. After roasting a sample of Pb-Ag jarosite for 4 hours at a temperature of 5300C and leaching the resulting roasting product with water, with a phase ratio of Č:T=1:5, high leaching of the examined metals Cu (91.07%), Zn (91.97%), In (99.95%) and low leaching of Fe (9.6%) was obtained in 1 hour. These technological parameters were adopted for the tests presented in this paper. After roasting the jarosit and lying the resulting roasting product, the lye solution was separated from the solid residue by filtering. In this paper, the treatment of the solid residue to obtain ferric phosphate is presented.

Chemical composition of the solid residue was, %: Fe - 49.3; Pb - 12.0; Ag – 0.014; Cu - 0.087; Zn - 0.93. X-ray diffraction (XRD) analysis was performed on a "RigakuMiniFlex 600" instrument with a "D/teXUltra 250" high-speed detector and an X-ray tube with a copper anode. The minerals hematite (Fe2O3), anglesite (PbSO4) and gypsum (CaSO4·2H2O) were identified in this sample. The most common mineral is hematite, anglesite is less common, while gypsum is the least common.

Laboratory research on the leaching of the solid residue of jarosite roasting (after leaching in water) was first carried out in a sulfuric acid solution with a concentration of 10% and 65% H2SO4 and with the introduction of oxidants (air and ozone). Research has shown a low level of iron leaching, from 0.6 - 1%. For this reason, subsequent leaching tests were performed with hydrochloric acid of technical quality, under different conditions. The highest degree of

---

[1] Corresponding author

Fe leaching of 91.41%, under the following conditions: ratio of phases Č:T=1:3, temperature t=800C and leaching time 1h, and represent the optimal conditions of the process of leaching in HCl. Hydroxide precipitation of Fe from alkaline solution was performed at pH=4. Alkaline solution was used for the experiments, and 2M NaOH was used as a neutralizing agent. After precipitation, the resulting precipitate was filtered and analyzed. The percentage of precipitated Fe from the ferric chloride solution was 100%.

The resulting hydroxide precipitate from alkaline solution was treated with a minimal amount of concentrated sulfuric acid until the iron precipitate was completely dissolved. The resulting ferric sulfate solution was filtered, the pH value of the filtrate was adjusted and then phosphoric acid was added.

According to literature data, using this procedure, FePO4x2H2O is obtained, while anhydrous FePO4 is obtained when drying at a temperature higher than 1800C. According to the standard (HG/T 4701-2021 China Chemistry Industry Standards), which refers to the required quality of ferric phosphate for the production of lithium batteries, the iron content in the FePO4 x2H2O product should be 28.5-30.0%. Chemical analysis of the obtained ferric phosphate showed that the obtained product was of satisfactory quality, containing 29.02% Fe. A detailed chemical analysis determined that the content of other metals (Zn, Al i Pb) in the ferric phosphate did not comply with the required standard. By recrystallization of the obtained FePO4x2H2O from the H3PO4 solution, the content of elements that deviated from the standard was reduced, whereby the following results were obtained: Pb -0.01%, Zn -0.002% and Al - 0.02%.

Keywords: Hydrometallurgy, ferric phosphate, lithium batteries, jarosite

Apply the copper anodes of non-standard chemical composition for sulphur acid waste solution electrolytical treatment

Radmila Markovic[1], Bern Friedrich[2], Dragana Bozic[1], Zoran Stevanovic[1]

[1]Mining and Metallurgy Institute Bor, Bor, Serbia
[2]Process Metallurgy and metal Recycling (IME), RWTH Aachen University, Aachen, Germany

Abstract

For more than a century, electrolytic refining is the main process for obtaining copper whose physical and chemical properties meet strict requirements for application in electronics, electrical engineering, energy, microelectronics. The accumulation of impurities such as nickel, arsenic, iron, antimony, leads to changes in the chemical composition of the electrolyte as one of the basic parameters in the process of copper cathodes obtaining. At the same time, due to a sudden increase in demand and reduction of copper content in the ores, secondary materials are increasingly being used to commercial copper anode production.

The copper anodes of non-standard chemical composition (high contents of Ni, Pb, Sn and Sb) are examined for electrolytic treatment of the waste sulphur acid solutions. These solutions originated from the commercial electrolytic copper refining processes. As well as the high concentration of Cu ions, these solutions contain high concentrations of Ni and As ions. The investigations were focused on the anode passivation behaviour, changes in the chemical composition of the solution, obtaining the cathode deposit and anode slime. Components for the anodes preparing were selected on the basis of literature data for the chemical composition of the anodes obtained from the secondary materials and the behaviour of impurities in the copper refining process. Nickel content had a constant value of 5 or 10 mass %, whereas the content of Pb, Sn and Sb was in range from 0.1 to 1 mass% per item. Different combinations of these values were used for anodes preparation.

Electrochemical measurements that were performed on laboratory type equipment, applying the method of anodic linear sweep voltammetry (ALSV), were used for preliminary investigations of anodes dissolution in acidic solution. The passivation peaks are registered on all voltammograms, but the values of the potential and current density were different. Comparing the results for series of anodes with the same nickel content (5 or 10 mass % Ni), it was found that anodes with a higher content of impurities (Pb+Sn+Sb mass %) were entering in the passive area at lower current density. The results confirmed that the copper anodes with high content of Ni, Pb, Sn and Sb could be refined in galvanostatic conditions at current density which value is characteristic for the commercial process. Investigations of the electrolytic treatment of the real waste sulphur acid solution with high content of Cu, Ni and As, at current density whose value is within commercial value, were carried out on the large-scale equipment. Refining of copper anodes was performed with constant galvanostatic pulse (25 mA/cm2), at two different temperatures ($T1 = 63 \pm 2$ °C and $T2 = 73 \pm 2$ °C) during the 72 h, the weight of each anode was about 7 kg. Based on the change of cell voltage value, which is measured and recorded by every 10 s for 72 h, it was found that all the anodes are dissolved during the process. Changing the cell voltage was carried out in several characteristic phases. The results showed that no one of the anodes is permanent passivated. In many numbers of the anodes, the passivation is appeared for a few minutes to a maximum of 40 minutes, but the anodes were reactivated after this time and continue to dissolve. The appearance of the stable and oscillatory phase was registered for the all anodes. At the anodes with 5 mass % Ni, the peak of passivation phenomenon was observed in 75 %, and in the anodes of the 10 mass % Ni, in 12.5 % of the total number of anodes.

The analysis of the concentration of Cu and Ni ions in solution showed that the Cu ions concentration decreases and the Ni concentration increases. Maximum concentration of Cu ions is reduced to about 3 % and the concentration of Ni ions maximized to 150 % of the respective baseline values. The decreasing of copper ions concentration was confirmed that along with the process of electrolytic refining of anodes occurs the electrowinning process. That is

---

[1] Corresponding author

confirmed by the data for the cathode deposits mass, which for all anodes and both temperatures were the higher than mass of copper that dissolve from the anodes. For a many numbers of anodes, cathode mass of deposit is greater than the theoretical values of the Cu mass that can precipitate at working current density. The different temperatures of the solution have no influence on the composition of the electrolyte. The investigation of the changes the arsenic ions concentrations has shown that the arsenic concentration was decreased compared to baseline value. The concentration of tin ions at the end of each experiment was greater than the baseline. During the first 24 h concentration changing was the highest, and in the continuation of the process the concentration changing varied from anode to anode. Changing the concentration of antimony in the first 24 h had an upward trend compared to the baseline value. The concentration of antimony is changed up to the end of the tests but there was no proper dependency. The analysis of the anode slime chemical composition was confirmed that the next elements are present in the slime: Pb, Sn, Sb, As, Ni and Cu. Based on the data of the anode slime mass and the weight of dissolved anodes, it was found that the percentage of anode slime is higher for the anodes with a higher content of Pb+Sn+Sb, at lower temperature. The minimum value of 0.58 % is obtained by refining the anode with 10 % Ni and 0.305 % Pb+Sn+Sb. The physical appearance and weight of cathode deposits have confirmed that during the treatment, two processes are conducted: electrorefining and electrowinning.

Keywords: anode, copper, nickel, lead, antimony, tin

Electrochemical performance of plasma sprayed Al_2O_3 coated on AISI 316L austenitic stainless steel in different body fluids

Mustafa YAZICI[1]

[1]High Technology Research and Application Center, Erzurum Technical University, 25050 Erzurum, Türkiye.

Abstract

AISI 316L austenite stainless steel (SS) has been a widely used material for orthopedic implants due to its high anti-corrosion under most atmosphere. High anti-corrosion is attributed to high-concentration Cr addition, which not only increases the corrosive potential of 316L SS but also forms a layer of dense passive films on AISI 316L austenitic stainless steel (SS). However, passive films are susceptible to severe localized attack in body media, which is the major drawback of AISI 316L austenite stainless steel (SS). Therefore, surface modification of AISI 316L austenite stainless steel (SS) resistant to body media is a current hot issue. Plasma spraying is effective for depositing ceramic coatings onto metallic materials and is often applied for raising the corrosion resistances of biomedical materials. Recently, ceramic coatings have been widely used in biomedical applications because of their good biocompatibility and physical properties. Especially, Al2O3 coatings are preferred for hip and knee prostheses owing to their inertness, good biocompatibility, and high corrosion resistance. These ceramic films are expected to improve the integration of implants into the bone system and to protect the substrate from corrosion in the body fluids and the tissue from the corrosion produces of the steel. For example, they are used in hip replacement, knee joints, dental crowns, skull implant applications and subcutaneous implants. Since 316L stainless steels are used in various applications, they are in contact with different body liquids in different environments of the body. Therefore, evaluating the electrochemical properties of Al2O3 coated AISI 316L austenite stainless steel (SS) in a single body fluid limits the correct use of the material to be used as implant and prosthesis. In this study, the samples, which were polished and then cleaned with ethyl alcohol, were coated Al2O3 on the surface of AISI 316L austenite stainless steel (SS) with the plasma spray method. The parameters used in the coating process are given below: power 22 kW, H2 flow rate 20 liter/hour, Ar flow rate 80 liter/hour, applied current 500 A, applied voltage 70 V, spraying distance 90 mm, type of electrode WCu, type of plasma gun Metco 3MB. AISI 316L austenite stainless steel (SS) are used in different applications in the body. XRD and SEM devices were used for structural analysis. The crystal phase structure of coating samples were analyzed with an X-ray diffractometer GNR brand device (XRD, GNR Explorer, Italy) XRD measurements were carried out by using a Cu Kα(λ=1.5418 Å) source and 40 kV and 40 mA diffractometer with 2θ range from 10° to 100°. The surface morphologies after coating were performed by using a environmental scanning electron microscope (E-SEM FEG-Quanta 250, FEI, USA). Electrochemical properties of all samples were measured using a GAMRY Series G750TM Potentiostat/Galvanostat/ZRA device. All measurements were carried out in Ringer Fluid, Simulated Body Fluid (SBF) and Simulated Synovial Fluid (SSF) at 37 °C. The composition of Ringer, SBF and SSF solution was shown in Table 1. A standard three-compartment cell consists of Ag/AgCl, graphite, as prepared specimens with an exposed surface area of 0.502 cm2 was used as the reference, counter and working electrode in 50 mL solutions, respectively. Electrochemical impedance spectroscopy (EIS) measurements were conducted at the open circuit potential (OCP) with the AC amplitude of 10 mV and an applied frequency ranging from 0.01 Hz to 100 kHz. The experimental results were interpreted on the basis of an equivalent circuit using a suitable fitting method elaborated by the Zsimpwin software. Polarization curves were recorded at a scan rate of 1mV s−1 in a potential range from−2 to+2 VRef. All of the electrochemical measurements were repeated at least two times in order to confirm the reproducibility of experimental results. The EIS was performed to observe the electrochemical behavior of the Al2O3 coatings AISI 316L austenitic stainless steel in various aggressive environments (Ringer, SBF and SSF). According to Nyquist curves the largest partial capacitive arc was seen in the SSF medium for all samples while the narrowest partial capacitive arc was observed in the Ringer medium for sample. As the partial capacitive arc enlarges, it can be said that the samples are also less exposed to corrosion. Another demonstration of the results obtained from the EIS analysis is the Bode plots, in which the frequency dependence of the analyzes and the phase angles can be seen. Bode plots of Al_2O_3 coatings in various aggressive environments are obtained. In addition, the

---

[1] Corresponding author

fit curves obtained with the circuits used are also included in the graphs. It can be thought that the ion concentration plays a very significant role in the corrosion mechanism. Especially since Ringer solution has higher inorganic types of ions (Cl^-) and amounts, it creates a more aggressive media than other solutions (SBF and SSF).

Keywords: AISI 316L austenite stainless steel, Al_2O_3 plasma spraying, electrochemical properties, SBF, SSF, Ringer

Designing and controlling of an inverted pendulum on a cart

Cagri KAYMAK[1], Aysegul UCAR[2]

[1,2]Department of Mechatronics Engineering, Fırat University, Elazığ, Turkey.

Abstract

The design and control of mechatronic systems play an important role in modern engineering applications. These systems have the potential to control many different mechanisms and platforms with complex dynamics. In particular, the inverted pendulum, a sub-branch of balancing problems, is a nonlinear system in which the pendulum is stabilized at the upper unstable equilibrium point in order to maintain the balance of the pendulum, and therefore presents a significant control challenge for engineers. Most systems are based on inverted pendulum-like structures. Due to its nonlinear structure and unstable equilibrium point, it is currently used in different fields such as mechatronic systems, acceleration and deceleration movements of rockets, biomechanical systems, wheeled motion and balance mechanisms. There are inverted pendulum systems with different structures in the literature. The prominent ones are single-pole inverted pendulum on a cart, double-pole inverted pendulum on a cart, and single and double-pole rotary inverted pendulum. In this study, system of single-pole inverted pendulum on a cart is investigated. First of all, the mechanical design of the inverted pendulum on a cart is realized. While performing the mechanical design, the designs of the other parts are completed by considering the parts to be used ready-made. Accordingly, the experimental setup of the inverted pendulum on a cart is established. Belt and pulley mechanism is mounted on a ready-made table and a shaft is placed in between. The cart designed in SolidWorks is produced with PolyLactic Acid (PLA) material using 3D printer technology in accordance with the design. The cart is mounted on the shaft and the cart is moved on the shaft with the help of a DC motor. A pendulum structure is created using an aluminum profile of appropriate dimensions. Interconnection parts produced with 3D printer technology are used to mount the pendulum to the cart. In addition, an incremental encoder is placed at the connection point of the pendulum to the cart to obtain information about the position of the pendulum. As hardware materials, a 20 V/1390 rpm DC motor, a 2-phase 400 ppr incremental encoder, ARM Cortex M4 and Teensy 3.6 microcontroller card with CPU frequency of 184 MHz are used to send the PWM information of the motor to the system and to receive the encoder information. To control the pendulum, Proportional-Integral-Derivative (PID) and Linear Quadratic Regulator (LQR), which are the most popular control methods, are preferred in the control structure. These methods are control methods with linear structure. For this reason, these methods give good results in controlling systems with linear structure.

Therefore, the position control of the pendulum is achieved by linearizing the obtained equations of motion of the system. For this purpose, the sine and cosine terms including the pendulum angle in the equations of motion are taken as 0 and 1 for small angles, respectively. The proportional, integral and derivative gain coefficients required for the PID controller are determined using the tuning tool in MATLAB/Simulink environment. The PID control generates the control signal at the output using the angle error of the pendulum. While designing the LQR control, a transition from the equations of motion to the state space form is made. Here, the coefficient matrices A and B are obtained.

These matrices are used in the design of the LQR control method. Since the state space form contains the error and the derivative of the error, the error of the pendulum angle is calculated since it is necessary to generate the error. Therefore, the angle of the pendulum at the upper unstable equilibrium point is required to be 0. The error that occurs enters the LQR controller, eventually producing the control signal. The parameters required in the design for the LQR are determined by trial and error. When the results are examined, it is seen that the pendulum angle reaches 0 degrees at the desired upper unstable equilibrium point in about 0.75 seconds with PID and 1.5 seconds with LQR. While the pendulum angle reaches the desired reference, it is seen from the graphs that the cart goes back and forth around 0 and reaches the reference value 0. When the results obtained with PID and LQR control methods are

---

[1] Corresponding author

analyzed, it is seen that the PID controller gives faster results. The results obtained with robust control methods such as intelligent control methods, sliding mode control can be brought to a better point. Although PID and LQR are linear control methods, the desired target has been achieved by obtaining very successful results. Since the inverted pendulum system forms the basis of many real systems, it is thought that the realization of this study will be very important for the solution of many complex systems.

Keywords: Inverted pendulum, Cart, PID, LQR

PID speed control of slider-crank mechanism in simulation environment

Muhammet AYDIN[1]

[1]Mechatronics Engineering, Faculty of Engineering, Firat University, Elazig, Turkey.

Abstract

Mechanisms are devices that enable the transfer and transformation of motion from one type of movement to another. Mechanisms are used in many places today. The opening and closing of bus doors, automobile jacks, adjustable pliers, attenuation tools, and windshield wipers of vehicles all perform their duties with the use of mechanisms. One of the most widely used mechanisms is the slider-crank mechanism. The slider-crank mechanism is mostly used in internal combustion engines to convert translational motion into rotational motion, and in pumps and compressors to convert rotational motion into translational motion. In the textile sector, the punching is applied to fabric and leather products. This process is mostly done manually using manpower. In order to save time and increase efficiency, a new slider-crank mechanism has been designed to serve this field by designing the slider-crank mechanism to perform this process automatically. In this study, a new design of the slider-crank mechanism has been designed to perform the punching process on fabric and leather materials in the textile industry. The use of the slider-crank mechanism will facilitate the drilling of multi-layer materials. Crank and connecting rod lengths have an effect on the speed of the drilling process. Since the speed of the drilling process is important, the importance of the speed control of the crank-connecting rod mechanism arises. Therefore, in this study, the speed control of the mechanism with PID control is realized in the Matlab/Simulink environment. For these purposes, firstly, the three-dimensional design of the mechanism was realized in the SolidWorks environment. The work started with the motor holder part. Considering the dimensions of the motor to be used, the motor holder part was designed to fix the motor. Then, the design of the crank part, which will perform the rotation process, was started. Since the crank part will be mounted on the motor shaft, it is designed for this purpose. For the next stage, the connecting rod, which connects the crank and the piston and will provide motion transfer between them, was designed. Since a drilling apparatus will be attached to the end of the piston, the piston is designed to consist of two parts. The drilling apparatus was placed between the first and second part of the piston and the piston was made into a single piece with suitable fasteners. Considering the channel in which the piston will move, the stroke is adjusted accordingly, so that the drilling apparatus to be used at the end of the piston can come out. Whether the designed mechanism makes the desired movement or not, the motion study was examined by giving rotational motion to the motor of the mechanism in the Solidworks environment. As a result of the motion study, it was seen that the mechanism realized the desired movement, and the feasibility of the speed control of the mechanism in the simulation environment was investigated theoretically by moving to the next stage. After it was seen that the designed mechanism realized the desired movement in the Solidworks environment, the mechanism was transferred from the Solidworks environment to the Matlab / Simmechanics environment, and the blocks of the mechanism were created. In the Simscape/Simmecanics environment, motor input was applied to the input limb of the mechanism, namely the crank element. For the operation of the motor, PID control is used and the PID control output is applied to the motor as a control signal. The purpose of applying PID control here is to ensure that the mechanism moves at the desired speed. PID control coefficients were found automatically by tuning. After the PID control process was applied to the blocks of the mechanism, the mechanism was requested to move at a constant speed of 4.25 rad/sec. As a result of the speed control,

---

[1] Corresponding author

it was obtained that the mechanism provided a speed of 4.272 rad/sec. This gives an error of 0.022 rad/sec. To sum up, in this study, a unique design of the slider-crank mechanism was made to perform the drilling process. Whether the design works properly or not was first observed as an animation in the solidworks program. Then the drawings were transferred to the Matlab/Simulink environment, and the blocks of the design were created and the speed control of the mechanism was realized. In the Matlab environment, the animation of the speed control of the mechanism was realized and it was successfully observed whether it moved as desired.

Keywords: Slider-Crank Mechanism, PID Control, Speed Control, Simulation.

Recognition of Mnist handwritten data by applying accelerated deep neural networks on the PYNQ FPGA development board and comparison of PYNQ with Nvidia Jetson TK1 and TX1 GPU development boards

Veysel Yusuf ÇAMBAY[1], Ayşegül UÇAR [2]

[1] Electrical Electronics Engineering, Faculty of Engineering, Muş Alparslan University, Türkiye.
[2]Mechatronics Engineering, Faculty of Engineering, Firat University, Elazig, Turkey.

Abstract

Object detection and recognition is one of the fundamental tasks in many fields such as autonomous unmanned ground vehicles, robotics and medical image processing. Recently, deep learning has been used by many researchers in these fields when the data size is large. In particular, Convolutional Neural Networks (ESAs), one of the most current structures of deep learning, have achieved great success in this field. The truth about ESAs Real-time studies were carried out embedded with Graphics Processing Unit (GPU) cards. Although GPUs result in high stability, they pose the problem of high power and energy consumption and large computational load. To overcome this problem, low-precision techniques called Binary Neural Networks (JNs) have been used. In other words, dualized weight and activation ESAs have started to be implemented on Field Programmable Gate Arrays (FPGAs). In this study, the Python development card in Xilinx Zynq was used. Pynq is designed with Python developers in mind. A base hardware full of modules and Python drivers was used in this work to accelerate and test deep learning applications. Xilinx's Zynq provides a very easy transition to the computing field. It also comes with a pre-installed Ubuntu Linux operating system. Therefore, all that is required is the basic logic of Linux and Python, and the user can start communicating with the board's peripherals. The fact that there are many peripherals on the card is the reason why we prefer this card over larger and faster FPGAs. Python is a convenient way to get started using Zynq to communicate with FGPA and run some examples, and it was also used in this project to control the High Speed Ethernet Cable (HDMI) interface. NVIDIA Jetson TK1 Developer Kit includes all the necessary modules to use GPU power in applications developed to run on embedded systems. With the Jetson TK1 Developer Kit, NVIDIA offers a complete software and hardware package. While CUDA, OpenGL 4.4 and Tegra-supported OpenCV standards are supported, various auxiliary development and testing software compatible with the camera and other hardware units are also provided. It is a fully functional CUDA platform that will allow you to quickly develop and deploy compute-intensive systems for computer vision, robotics, and medicine. The world's first supercomputer on a module, the Jetson TX1 delivers the performance and power efficiency required for the latest visual computing applications. It is built around the NVIDIA Maxwell™ architecture and delivers over 1 TeraFLOP performance with 256 CUDA cores. It is the best system for deep learning, computer vision, graphics and high-performance GPU computing, integrated with 64-bit CPUs, 4K video encoding and decoding capabilities, 1400 MPix/s capable camera interface. In this study, MNIST handwriting recognition study was carried out using ANN, which is used in many fields. A comparison was made on both deep learning structures and Nvidia's GPUs such as Jetson TK1 and TX1 on data sets that are widely used in scientific literature, such as MNIST. An application has been made to recognize MNIST handwriting. The MNIST dataset contains 60000 training images and 10000 test data images of 28x28 size consisting of handwritten digits. Conventional ANN was used on this card. If we define the network structure, it consists of 4 fully connected layers and 1024 neurons each. Two different precisions were used for this network structure. The results obtained by working on these networks only in PL (programmable logic) and only in PS (processor) are given in Table 1. The times taken for classification are given graphically. In the tables and figures, 1 bit weight and 1 activation are named ANN-1 and 1 bit weight and 2 activations are named ANN-2. For PS, although results are given on only 10 images in order to perform appropriate processing in the image frame range, as can be seen, the processing time is quite high when processing only in PS. PYNQ's accuracy is lower than GPUs. This is because quantization has been done. On

---

[1]Corresponding author

the other hand, PYNQ is faster than other GPUs. Apart from this, the given Zynq XC7Z020-caffe-lasagne application took longer than ANN-1 and ANN-2. This is because the network structure is more complex than ANN 1 and ANN 2. In the study, results such as duration, power consumption and stability were examined. It has guided us for use in different applications. By applying the recognition process on MNIST handwritten datasets used for comparison in the scientific literature, comparisons were made with CPUs and Nvidia's Jetson TK1 and TX1 GPU cards in terms of speed and stability. Additionally, PYNQ has been shown to provide higher efficiency and lower power usage than Nvidia GPU cards and GPU systems. Judging by the results of this study, good results were obtained in terms of efficiency. Additionally, artificial intelligence with limited hardware such as Jetson TX1, TK1 and has been shown to be implemented successfully. In future studies, efforts will continue to accelerate different DSAs in hardware and software.

Keywords: MNIST, PYNQ, JETSON, GPU, TK1, TK2

Examination of articular cartilage mechanics under sealed and unsealed conditions

Sabri UZUNER[1]

[1]Department of Mechatronics, Faculty of Engineering, University of Duzce, Duzce, Turkey.

Abstract

Articular cartilage, with its distinctive translucent appearance, compatible covers the articulating surfaces of bones within the knee joint, giving it seamless and friction-free movement. At its core, articular cartilage manifests as a water-saturated porous matrix, with fluid constituting a significant portion of its weight. Remarkably, approximately 68-85% of the overall weight of articular cartilage is attributed to fluid content. This high-water concentration allows cartilage to exhibit its unique biomechanical properties, including load-bearing properties, shock absorption, and joint lubrication, by moving through the porous solid or exudating from tissue due to the load exposed.

Most numerical studies on knee mechanics did not consider fluid boundary conditions. The aim of this study was to investigate the effect of different fluid boundary conditions at the joint surfaces on contact mechanics and fluid pressure. Two different finite element (FE) analyses were performed for the knee joint model developed for this purpose. One was the analysis with unsealed boundary conditions, which assumes that the fluid moved out of the tissue, and the other was the analysis with the sealed boundary conditions, which do not allow fluid out of the tissue.

The 3D FE knee joint model was accepted as biphasic to consider the fluid-solid interaction. The model included the bony structures (femur and tibia) and the articular cartilage (femoral and tibial cartilage). The bony structures were considered rigid materials, as they exhibited greater stiffness compared to the articular cartilages. In contrast, the soft tissues were considered compressible and comprised both solid and liquid phases. The solid phase was modelled linear elastic, with Young's modulus of 9 MPa and Poisson’s ratio of 0.36. The fluid phase was considered isotropic, with a permeability value of 0.001 mm4/Ns. In the unsealed analysis, the pore pressure in the Abaqus environment was initially set to zero as a boundary condition. This configuration allows the fluid to escape from the surface and sides of the cartilage freely, facilitating its movement. The knee joint model that was developed underwent a compression force of 200N. The applied force followed a ramp creep profile, gradually increasing to its maximum within 10 seconds and maintaining a constant magnitude for 100 seconds. A comprehensive analysis spanning 100 seconds was conducted, providing ample time for the fluid to permeate through the tissue. This duration facilitated a thorough investigation of the dynamic behaviour within the articular cartilage, offering a comprehensive understanding of its intricate mechanisms. The femur was allowed to move in the vertical direction while restricted in other directions. The tibia was fixed from all sides to provide contact convergence.

The findings from both analyses indicated no significant difference in contact pressure. However, a notable disparity was observed between the pressures exerted by the liquid and solid phases of tibial cartilage. During the early creep phase at the 10th second, the contact pressure in both analyses was approximately 2MPa. However, as the fluid within the porous solid phase started to move, the contact pressure gradually relaxed and decreased to around 1.6MPa by the 100th second. This observation underscores the role of fluid dynamics in the redistribution of pressure within the system over time. The similarity in contact pressure between the analyses could be attributed to the insufficient analysis time for generating significant results. In other words, an adequate amount of fluid may not have been exudated from the tissue during the analyzed timeframe. A longer analysis duration may be necessary to observe more pronounced effects and better understand the behaviours of the fluid within the tissue. At the 10th second, when the compression force peaked, there was no significant difference in liquid pressure between the two analyses. However, at the 100th second, a notable contrast emerged. In the sealed analysis, the fluid pressure was approximately 3.5 times higher than in the unsealed analysis. This discrepancy caused by the sealing prevented the fluid from escaping, resulting in increased pressure. Similarly, the solid stress exhibited the greatest disparity between the two analyses towards the end of the creep phase. At 100 seconds, the sealed analysis demonstrated a 15% lower

---

[1]Corresponding author

solid stress than the unsealed analysis. This difference can be attributed to less fluid being retained within the tissue in the unsealed analysis, leading to increased higher solid stress. Overall, the lower fluid pressure and higher solid stress observed in the unsealed analysis can be attributed to the expulsion of fluid from the tissue, influencing the mechanical behaviour of the system.

This study elucidated the impact of fluid boundary conditions on solid stress, contact, and fluid pressures. The findings underscore the significant influence of boundary conditions on relaxation times and load distribution between solid stress and fluid pressure. Specifically, in the sealed analysis, the stress predominantly relies on the liquid phase, resulting in minimal tissue relaxation.

Keywords: articular cartilage, biphasic, creep, sealed, unsealed

Classification of brain tumors from MRI images using the UNet architecture

Gamze TEKBAŞ[1], Rabia Gizemnur EREN[2], Beyda TAŞAR[3]

[1,2,3]Mechatroics Engineering, Engineering Faculty, Firat University, Elazig, Turkey.

Abstract

The term "brain tumor" is used to describe the uncontrolled growth of cells in the skull region. These tumors can originate within the brain or from the surrounding tissues and can grow inward into the skull. Tumors located inside the skull can exhibit noticeable symptoms due to increased pressure. Since brain tumors are located within the skull, they can lead to common symptoms such as severe headaches, nausea, and vomiting due to increased intracranial pressure. In addition, different symptoms may arise depending on which part of the brain is affected, including weakness, numbness, gait disturbances, vision loss, hearing loss, memory problems, speech difficulties, and imbalance on either the right or left side of the body. In the case of pituitary gland tumors, various hormonal disturbances such as irregular menstruation and growth in the hands and feet can occur [1].

As with any cancer type, there is no universally accepted cause for the development of brain tumors. However, studies on the age relationship of brain tumors have shown that the likelihood of developing a brain tumor increases with age. Due to the aging of the world's population, it is estimated that the incidence of brain tumors in society will gradually increase. Research indicates that one brain tumor develops in every 100,000 individuals. With the prediction that this rate will increase in the coming years, scientists have focused on early diagnosis, treatment, and improving the quality of life for brain tumor patients [1].

Brain tumors are classified based on their locations and shapes. The World Health Organization (WHO) categorized brain tumors into seven main categories in 2016. Under these main categories, there are more than 30 tumor types with different characteristics. One of the significant reasons for this classification is that not all tumors that occur within the brain are directly related to the nervous system; some tumors can develop due to other abnormal cells, blood vessels, meninges, or tumors seen in different parts of the body outside the brain. Brain tumors are fundamentally divided into primary and secondary tumors.

Tumors that occur anywhere in the brain tissue and spread are referred to as primary tumors. Among the most common types of primary tumors, which can be benign or malignant, are gliomas and meningiomas originating from glial cells. Cancer cells from organs such as the stomach, lungs, or intestines can reach the brain through blood vessels. The new cancerous cells formed in the brain due to these cells are referred to as secondary tumors or metastases. Benign tumors are those that do not originate from brain cells and do not contain cancer cells. Generally, benign tumors grow slowly and have well-defined boundaries, making it possible to remove them through surgery, either in part or in whole, from brain tissue. However, when benign tumors grow to very large sizes, they can exert pressure on nearby tissues, interfering with certain brain functions. Although it is rare, benign tumors can occasionally transform into malignant ones. These tumors have a low risk of recurrence and metastasis. Common benign tumors include meningiomas, dermoid and epidermoid tumors, colloid cysts, pituitary adenomas, neurinomas, hemangioblastomas, and astrocytomas [2].

Rapidly growing and spreading malignant tumors are the main cause of brain cancer. Malignant tumors with unclear boundaries can also damage the surrounding brain tissue, disrupting brain function. These tumors, composed of cells responsible for performing brain functions, are not typically completely removed through surgery, as removing all of these cells would result in the loss of brain activities. After surgical procedures, malignant tumors can regrow. Common malignant tumors include glial tumors and metastatic brain cells. Glial tumors, one of the most common brain tumors that lead to cancer, proliferate uncontrollably. As a result of this rapid growth, cancerous cells affect

---

[2] Corresponding author

the surrounding healthy cells. These tumors are categorized as Grade I, Grade II, Grade III, and Grade IV, and various treatment methods are applied to patients. Metastatic cells occur when cancerous cells from a different part of the body outside the brain spread to the brain. Although approximately 10% of all brain tumors are metastatic, these can originate from various organs such as the lungs, stomach, and pancreas, and sometimes, the source of these cancerous cells cannot be identified [2].

Early detection of brain tumors and early initiation of treatment can increase the patient's lifespan and quality of life. The most effective method used for diagnosing brain tumors is MRI, which provides detailed imaging of brain tissues. During MRI imaging, anomalies are identified, and a definite diagnosis is made through the analysis of tissue samples taken by pathology experts. Therefore, it is of utmost importance to demonstrate and describe brain tumors in detail using advanced radiological imaging techniques for treatment planning. In this study, an image analysis-based approach for the detection of brain tumors is presented. Data features (tumor region, tissue, color, location, edge, etc.) are extracted from MRI images, and using the UNet architecture, a tumor detection accuracy of over 98% has been achieved. The results indicate that the developed method can provide decision-support knowledge to experts.

Keywords: Brain Tumor, MR, Classification, UNet.

Reference

[1] Acıbadem Web ve Yayın Kurulu, Beyin Tümörleri, https://www.acibadem.com.tr/ilgi-alani/beyin-tumorleri/ , Erişim tarihi: 06.09.2023

[2] Doç. Dr. Enis Kuruoğlu , Beyin Tümörü Nedir? https://www.medicana.com.tr/saglik-rehberi-detay/10269/beyin-tumoru-nedir , Erişim tarihi: 06.09.2023

International Conference on Advances and
Innovations in Engineering

A survey on hybrid Wheel-Leg mobile robots

İrem MERTYÜZ[1], Ahmet B. TATAR[2] , Alper K. TANYILDIZI [3], Beyda TAŞAR[4], Oğuz YAKUT[5]

[1,3,4,5] Mechatronics Engineering, Engineering Faculty, Firat University, Elazig, Turkey.
[2]Mechanical Engineering, Engineering Faculty, Adiyaman University, Adiyaman, Turkey.

Abstract

Mobile Land Robots (MLRs) have been increasingly used in the military industry in recent years, and they are becoming more common in a variety of applications such as reconnaissance, observation, target detection, destruction, search, and rescue [1]. Different mechanical designs for mobile robotic land robots are being developed to offer them excellent agility in variable and tough environmental circumstances [2]. Robots with wheels can move swiftly and perform effectively on flat areas. The wheel structure, on the other hand, makes it difficult for the robot to overcome obstacles on rough terrain [3-4]. As a result, researchers have created robotic land robots with various operating principles, such as wheeled, tracked, and legged robots [5]. The motions of search and rescue robots in relation to their working environments show that the robot must traverse obstacles like uneven ground and stairs while concurrently moving on flat ground for lengthy periods of time [6]. As a result, several designs for MLRs, which were previously seen with wheeled and tracked designs, have been developed in recent years. These designs include hybrid wheel-leg combinations and those with different types of legs [7,8].

Legged and hybrid mobile land robots were built on studies in biomimicry (animal modeling). They take inspiration from the physiology and anatomy of terrestrial creatures [9] in their designs. The locomotion systems of these animals have been studied and modeled. Research on this subject began with an understanding of the evolutionary development mechanisms of terrestrial creatures [10]. According to studies, the legs of terrestrial animals developed over time into robust, active legs that enable them to move swiftly and easily over uneven terrain [11]. As a result, the concept of using legged MLRs in robotics, designing, and manufacturing them developed [12,13]. In recent years, there has been a rise in research into legged robot design [14-16].

When it comes to crossing uneven terrain, and overcoming obstacles such as curbstones, legged robots have an advantage over wheeled robots. However, legged robots do not perform as well on flat surfaces as wheeled robots. As a result, researchers have concentrated on hybrid robot projects that combine the benefits of both types of robots, particularly for usage in difficult and complex terrains. In this regard, legged-wheeled hybrid robots have received a lot of interest in recent years [13]. Hybrid robots combine the energy efficiency and high-speed potential of wheeled robots with the flexibility of legged robots. This paper includes a thorough examination of hybrid robots.

Legged-wheeled hybrid robots can be classified into three main principles. Firstly, there are robots with a fixed leg structure with wheel mechanisms mounted at the end of each leg. Examples in this category include PAW [17], [18], Hylos [19], Walk'n Roll [20], Roller-Walker [21], AirHopper [22], Wheeleg [23], RT-Mover [24], and HIT-HYBTOR [25]. For instance, PAW [17-18] is a four-legged robot with an active wheel at the end of each leg, allowing it to climb high steps. Hylos [19] enhances movement flexibility in wheeled mode with active wheels but may reduce stability in legged mode.

Secondly, there are robots with transformable segmented wheel mechanisms. This group includes examples such as Armadillo-Inspired Wheel-Leg Robot [26], [27], Transformer Robot [28], [29], Transformable Claw Wheel Robot [30], Quattroped [31], Turboquad [32], RDB [33], LEON [34], RoVaLL [35], Leg-Wheel Transformable Robot [36], WheeLeR [37], LDR [38], and FUHAR [39]. For instance, Quattroped [31] can climb step obstacles by combining its four wheels. RoVaLL [35] can change direction thanks to the cam mechanism inside its wheel.

---

[1] Corresponding author

The third category consists of robots where the wheel and leg structures are independent, and when on flat terrain, the legs are concealed within the wheel or body. Examples in this group include Transleg [40], [41], Serial-Parallel Hybrid Mechanism Wheelleged robot [42], Tendon-Actuated Foldable Wheeled-Legged Robot [43], and PEOPLER-II [44]. For instance, Transleg [40] is a robot that can operate in both wheeled and legged modes and achieves motion transitions with a single actuator.

In conclusion, legged-wheeled hybrid robots have significant potential for various application areas, using different design principles and mechanisms. The advantages and disadvantages of these robots can vary depending on their design features, and each can be optimized for specific tasks or environmental conditions. Therefore, it is likely that these hybrid robots will find more application areas in the coming years, with the emergence of more advanced designs.

Keywords: Hybrid robots, transformable wheels, wheeled-legged robots.

References

[1] L. Bai, An optional passive/active transformable wheel-legged mobility concept for search and rescue robots, Robotics and Autonomous Systems, 107, (2018), 145-155. https://doi.org/10.1016/j.robot.2018.06.005

[2] S. Tao, A transformable wheel-legged mobile robot: Design, analysis and experiment, Robotics and Autonomous Systems, 98, (2017), 30-41. https://doi.org/10.1016/j.robot.2017.09.008

[3] Y. She, C.J. Hurd, H. Su, A transformable wheel robot with a passive leg, 2015 IEEE/RSJ International Conference on Intelligent Robots and Systems (IROS), (2015), 4165-4170. https://doi.org/10.1109/IROS.2015.7353966

[4] X. Xıe, Design and development of a new transformable wheel used in amphibious all-terrain vehicles (A-ATV), Journal of Terramechanics, 69, (2017), 45-61. https://doi.org/10.1016/j.jterra.2016.11.001

[5] Russo, Matteo & Ceccarelli, Marco. (2020). A Survey on Mechanical Solutions for Hybrid Mobile Robots. Robotics. 9. 32. https://doi.org/10.3390/robotics9020032

[6] X. Zhao, W. Su and S. Zhang, "The Simulation and Analysis of a New Rescue Robot with Transformable Wheels," 2019 2nd World Conference on Mechanical Engineering and Intelligent Manufacturing (WCMEIM), Shanghai, China, 2019, pp. 545-548, https://doi.org/10.1109/WCMEIM48965.2019.00116.

[7] T Sun, X Xiang, W Su, H Wu and Y Song, "A transformable wheel-legged mobile robot: Design analysis and experiment", Robotics and Autonomous Systems, vol. 98, pp. 30-41, Dec. 2017.https://doi.org/10.1016/j.robot.2017.09.008

[8] Y She, C J Hurd and H J Su, "A transformable wheel robot with a passive leg", Intelligent Robots and Systems (IROS), vol. 2015, pp. 4165-4170, December, Dec. 2016. https://doi.org/10.1115/1.4037018

[9] K. Tadakuma et al., "Armadillo-inspired wheel-leg retractable module," 2009 IEEE International Conference on Robotics and Biomimetics (ROBIO), Guilin, 2009, pp. 610-615, https://doi.org/10.1109/ROBIO.2009.5420604.

[10] Boston Dynamics, Spot, (6 May,2020),https://www.bostondynamics.com/spot

[11] S.C.Chen, K.J. Huang, W.H. Chen, S.Y. Shen, C.H. Li, Quattroped: A Leg–Wheel Transformable Robot, IEEE/ASME Transactıons On Mechatronıcs, 19(2), (2014). https://doi.org/10.1109/TMECH.2013.2253615

[12] P. Liljeback, K.Y. Pettersen, Q. Stavdahl, J.T. Gravdahl, Snake robot locomotion in environments with obstacles, IEEE/ASME Trans. Mechatronics, 17(6), (2012), 1158-1169. https://doi.org/10.1109/TMECH.2011.2159863

[13] N.O. Perez-Arancibia, J.P. Whitney, R.J. Wood, Lift force control of flapping-wing microrobots using adaptive feedforward schemes, IEEE/ASME Trans. Mechatron., 18(1), (2013), 155–168. https://doi.org/10.1109/TMECH.2011.2163317

[14] S. Lohmeier, T. Buschmann, H. Ulbrich, System design and control of anthropomorphic walking robot LOLA, IEEE/ASMETrans.Mechatron., 14(6), (2009), 658–666. https://doi.org/10.1109/TMECH.2009.2032079

[15] Y.D. Hongand, J.H. Kim, 3-D command state-based modifiable bipedal walking on uneven terrain, IEEE/ASME Trans. Mechatron., 18(2), (2013), 657–663. https://doi.org/10.1109/TMECH.2012.2182777

[16] D.J. Braun, J.E. Mitchell, M. Goldfarb, Actuated dynamic walking in a seven-link biped robot, IEEE/ASME Trans. Mechatron., 17(1), (2012), 147–156. https://doi.org/10.1109/TMECH.2010.2090891

[17] J. A. Smith, I. Sharf, ve M. Trentini, “PAW: a hybrid wheeled-leg robot”, içinde Proceedings 2006 IEEE International Conference on Robotics and Automation, 2006. ICRA 2006., Orlando, FL, USA: IEEE, 2006, ss. 4043-4048. doi: 10.1109/ROBOT.2006.1642323.

[18] J. A. Smith, I. Sharf, ve M. Trentini, “Bounding Gait in a Hybrid Wheeled-Leg Robot”, içinde 2006 IEEE/RSJ International Conference on Intelligent Robots and Systems, Beijing, China: IEEE, Eki. 2006, ss. 5750-5755. doi: 10.1109/IROS.2006.282458.

[19] G. Besseron, C. Grand, F. Ben Amar, ve P. Bidaud, “Decoupled control of the high mobility robot Hylos based on a dynamic stability margin”, içinde 2008 IEEE/RSJ International Conference on Intelligent Robots and Systems, Nice: IEEE, Eyl. 2008, ss. 2435-2440. doi: 10.1109/IROS.2008.4651092.

[20] H. Adachi, N. Koyachi, T. Arai, A. Shimiza, ve Y. Nogami, “Mechanism and control of a leg-wheel hybrid mobile robot”, içinde Proceedings 1999 IEEE/RSJ International Conference on Intelligent Robots and Systems. Human and Environment Friendly Robots with High Intelligence and Emotional Quotients (Cat. No.99CH36289), Kyongju, South Korea: IEEE, 1999, ss. 1792-1797. doi: 10.1109/IROS.1999.811738.

[21] G. Endo ve S. Hirose, “Study on Roller-Walker - Energy efficiency of Roller-Walk -”, içinde 2011 IEEE International Conference on Robotics and Automation, Shanghai, China: IEEE, May. 2011, ss. 5050-5055. doi: 10.1109/ICRA.2011.5980144.

[22] T. Tanaka ve S. Hirose, “Development of leg-wheel hybrid quadruped “AirHopper” design of powerful light-weight leg with wheel”, içinde 2008 IEEE/RSJ International Conference on Intelligent Robots and Systems, Nice: IEEE, Eyl. 2008, ss. 3890-3895. doi: 10.1109/IROS.2008.4650880.

[23] M. Lacagnina, G. Muscato, ve R. Sinatra, “Kinematics, dynamics and control of a hybrid robot Wheeleg”, Robotics and Autonomous Systems, c. 45, sy 3-4, ss. 161-180, Ara. 2003, doi: 10.1016/j.robot.2003.09.006.

[24] S. Nakajima, “RT-Mover: a rough terrain mobile robot with a simple leg–wheel hybrid mechanism”, The International Journal of Robotics Research, c. 30, sy 13, ss. 1609-1626, Kas. 2011, doi: 10.1177/0278364911405697.

[25] Bo Huang, Lining Sun, ve Yufeng Luo, “Statically balanced stair climbing gait research for a hybrid quadruped robot”, içinde IEEE International Conference Mechatronics and Automation, 2005, Niagara Falls, Ont., Canada: IEEE, 2005, ss. 2067-2071. doi: 10.1109/ICMA.2005.1626881.

[26] K. Tadakuma vd., “Armadillo-inspired wheel-leg retractable module”, içinde 2009 IEEE International Conference on Robotics and Biomimetics (ROBIO), Guilin, China: IEEE, Ara. 2009, ss. 610-615. doi: 10.1109/ROBIO.2009.5420604.

[27] K. Tadakuma vd., “Mechanical design of the Wheel-Leg hybrid mobile robot to realize a large wheel diameter”, içinde 2010 IEEE/RSJ International Conference on Intelligent Robots and Systems, Taipei: IEEE, Eki. 2010, ss. 3358-3365. doi: 10.1109/IROS.2010.5651912.

[28] Y.-S. Kim, G.-P. Jung, H. Kim, K.-J. Cho, ve C.-N. Chu, “Wheel Transformer: A Wheel-Leg Hybrid Robot With Passive Transformable Wheels”, IEEE Trans. Robot., c. 30, sy 6, ss. 1487-1498, Ara. 2014, doi: 10.1109/TRO.2014.2365651.

[29] Y.-S. Kim, G.-P. Jung, H. Kim, K.-J. Cho, ve C.-N. Chu, “Wheel transformer: A miniaturized terrain adaptive robot with passively transformed wheels”, içinde 2013 IEEE International Conference on Robotics and Automation, Karlsruhe, Germany: IEEE, May. 2013, ss. 5625-5630. doi: 10.1109/ICRA.2013.6631385.

[30] J.-J. Chou ve L.-S. Yang, “Innovative design of a claw-wheel transformable robot”, içinde 2013 IEEE International Conference on Robotics and Automation, Karlsruhe, Germany: IEEE, May. 2013, ss. 1337-1342. doi: 10.1109/ICRA.2013.6630744.

[31] Ke Jung Huang, S.-C. Chen, Ya Cheng Chou, S.-Y. Shen, Cheng-Hsin Li, ve Pei-Chun Lin, “Experimental validation of a leg-wheel hybrid mobile robot Quattroped”, içinde 2011 IEEE International Conference on Robotics and Automation, Shanghai, China: IEEE, May. 2011, ss. 2976-2977. doi: 10.1109/ICRA.2011.5980480.

[32] H.-S. Lin, W.-H. Chen, ve P.-C. Lin, “Model-based dynamic gait generation for a leg-wheel transformable robot”, içinde 2015 IEEE International Conference on Robotics and Automation (ICRA), Seattle, WA, USA: IEEE, May. 2015, ss. 5184-5190. doi: 10.1109/ICRA.2015.7139921.

[33] C. C. Phipps, B. E. Shores, ve M. A. Minor, “Design and Quasi-Static Locomotion Analysis of the Rolling Disk Biped Hybrid Robot”, IEEE Trans. Robot., c. 24, sy 6, ss. 1302-1314, Ara. 2008, doi: 10.1109/TRO.2008.2007936.

[34] E. Rohmer, G. Reina, ve K. Yoshida, “Dynamic Simulation-Based Action Planner for a Reconfigurable Hybrid Leg–Wheel Planetary Exploration Rover”, Advanced Robotics, c. 24, sy 8-9, ss. 1219-1238, Oca. 2010, doi: 10.1163/016918610X501499.

[35] J. V. Salazar Luces, S. Matsuzaki, ve Y. Hirata, “RoVaLL: Design and Development of a Multi-Terrain Towed Robot With Variable Lug-Length Wheels”, IEEE Robot. Autom. Lett., c. 5, sy 4, ss. 6017-6024, Eki. 2020, doi: 10.1109/LRA.2020.3010495.

[36] T.-H. Wang ve P.-C. Lin, “A Reduced-Order-Model-Based Motion Selection Strategy in a Leg-Wheel Transformable Robot”, IEEE/ASME Trans. Mechatron., c. 27, sy 5, ss. 3315-3321, Eki. 2022, doi: 10.1109/TMECH.2021.3126606.

[37] C. Zheng ve K. Lee, “WheeLeR: Wheel-Leg Reconfigurable Mechanism with Passive Gears for Mobile Robot Applications”, içinde 2019 International Conference on Robotics and Automation (ICRA), Montreal, QC, Canada: IEEE, May. 2019, ss. 9292-9298. doi: 10.1109/ICRA.2019.8793686.

[38] L. Bai, J. Guan, X. Chen, J. Hou, ve W. Duan, “An optional passive/active transformable wheel-legged mobility concept for search and rescue robots”, Robotics and Autonomous Systems, c. 107, ss. 145-155, Eyl. 2018, doi: 10.1016/j.robot.2018.06.005.

[39] İ. Mertyüz, A. K. Tanyıldızı, B. Taşar, A. B. Tatar, ve O. Yakut, “FUHAR: A transformable wheel-legged hybrid mobile robot”, Robotics and Autonomous Systems, c. 133, s. 103627, Kas. 2020, doi: 10.1016/j.robot.2020.103627.

[40] Z. Wei, G. Song, Y. Zhang, H. Sun, ve G. Qiao, “Transleg: A wire-driven leg-wheel robot with a compliant spine”, içinde 2016 IEEE International Conference on Information and Automation (ICIA), Ningbo, China: IEEE, Ağu. 2016, ss. 7-12. doi: 10.1109/ICInfA.2016.7831789.

[41] Z. Wei, J. Zhang, Y. Yang, S. Xiang, H. Sun, ve A. Song, “Design, Control and Simulation of a Leg-Wheel Robot: STransleg”, içinde 2023 3rd International Conference on Computer, Control and Robotics (ICCCR), Shanghai, China: IEEE, Mar. 2023, ss. 234-238. doi: 10.1109/ICCCR56747.2023.10193990.

[42] J. Niu vd., “Kinematic Analysis of a Serial-Parallel Hybrid Mechanism and its Application to a Wheel-Legged Robot”, IEEE Access, c. 8, ss. 111931-111944, 2020, doi: 10.1109/ACCESS.2020.3001653.

[43] Y. Yang, C. Zhang, ve W. Xu, “Design of a Tendon-Actuated Foldable Wheeled-Legged Hybrid Mobile Robot with high load-bearing capacity”, içinde 2022 17th International Conference on Control, Automation, Robotics and Vision (ICARCV), Singapore, Singapore: IEEE, Ara. 2022, ss. 604-609. doi: 10.1109/ICARCV57592.2022.10004338.

[44] T. Okada, W. T. Botelho, ve T. Shimizu, “Motion Analysis with Experimental Verification of the Hybrid Robot PEOPLER-II for Reversible Switch between Walk and Roll on Demand”, The International Journal of Robotics Research, c. 29, sy 9, ss. 1199-1221, Ağu. 2010, doi: 10.1177/0278364909348762.

Modeling a spacecraft simulation of the lunar landing with reinforcement learning

Tolga MERTYÜZ[1] , Alper K. TANYILDIZI [2], Beyda TAŞAR[3], Oğuz YAKUT[4]

[1,2,3,4,5]Mechatronics Engineering, Engineering Faculty, Firat University, Elazig, Turkey.

Abstract

Reinforcement learning is a learning approach within the field of artificial intelligence that aims to simulate behavioral decision-making processes. This approach represents a process in which an agent gains experience by interacting with its environment while attempting to accomplish a specific task. The agent learns by observing environmental states and selecting appropriate actions in response to these states. The outcomes are rewarded or penalized based on the success or failure of the chosen actions. Reinforcement learning aims to enable the agent to learn the most optimal behaviors from these rewards. This method is applied in various domains, including autonomous driving, game strategy development, and industrial process control, representing a significant research topic in the field of artificial intelligence.

Numerous studies have adopted reinforcement learning techniques in the motion planning and control of autonomous robots [1-3]. For instance, reinforcement learning can be used to enhance a robot's ability to navigate obstacles or reach specific targets. Such studies enable robots to adapt to environmental changes in real-time and perform their tasks more effectively. Additionally, reinforcement learning has an impact on the use of robots in industrial automation. Industrial robots are employed for tasks such as optimizing production lines, handling materials, and performing assembly processes [4-5]. Reinforcement learning can assist these robots in working more flexibly and efficiently by quickly adapting to environmental changes. Reinforcement learning is also applied to enable robots to learn how to play games and develop competitive strategies. These studies have led to significant advancements in artificial intelligence and game theory [6]. In summary, the applications of reinforcement learning in robotics are diverse, and academic research in this field serves as a valuable resource for making robots smarter, adaptable, and effective.

In this study, a simulation of a rocket's vertical landing, aimed at enabling rockets to make upright landings on the Earth's surface, was conducted using reinforcement learning-based simulator design. Rockets serve as vehicles for space travel, and during these journeys, parts of the rocket that are no longer needed are discarded into space, contributing to space debris. These discarded parts create thick layers of debris around the planet. To address this issue, reusable rocket designs are necessary, and achieving reusability involves enabling rockets to make vertical landings on Earth. Reinforcement learning, a subfield of artificial intelligence, provides a framework and tools for designing this complex and challenging behavior in rockets. In this study, the Python language and the Gym library from OpenAI were used to simulate the mission of a spacecraft (rocket). The mission was to land the spacecraft vertically between two flags on the moon's surface. The task was initially addressed by training a baseline model, and experiments were conducted to assess the impact of adjustable hyper parameters such as learning rate (α), discount factor (γ), and epsilon decay (ϵ) on the model's performance. These experiments involved changing hyper parameters to observe their effects on the model's performance and comparing the results. The experiments revealed that the spacecraft successfully completed the lunar landing mission. In this study, a reinforcement learning algorithm called Deep Q-Learning (DQL) was used to enable the spacecraft to autonomously explore and learn the lunar landing environment. The lunar landing environment was precisely defined using the OpenAI Gym toolkit. To fully execute the lunar landing experiment, a comparison model was first trained using the Deep Q-Learning algorithm, which incorporates experience replay and ϵ-greedy exploration. Subsequently, experiments were conducted to analyze the effects of changing hyper parameters on the model's performance. Different learning rates (0.0001, 0.001, 0.01, 0.1)

---

[3] Corresponding author

were selected to verify the impact of different learning rates on model performance. The best performance was observed for a learning rate of 0.001, which was the middle value among the chosen learning rates. Different discount factor (γ) values (0.99, 0.9, 0.8, 0.7) were selected to validate their effects on model performance. In Figure 7, it can be observed that the agent performed best for a gamma value of 0.99. Epsilon decay values were changed to 0.999, 0.995, 0.99, and 0.9, and the worst agent performance was observed for an epsilon decay value of 0.999. The results clearly illustrate the impact of hyper parameter selection on the reinforcement learning model.

Keywords: Artificial intelligence, reinforcement learning, deep Q-learning, spacecraft, lunar landing simulator.

References

[1] Zhu, K., & Zhang, T. (2021). Deep reinforcement learning based mobile robot navigation: A review. Tsinghua Science and Technology, 26(5), 674-691.

[2] Huang, B. Q., Cao, G. Y., & Guo, M. (2005, August). Reinforcement learning neural network to the problem of autonomous mobile robot obstacle avoidance. In 2005 International conference on machine learning and cybernetics (Vol. 1, pp. 85-89). IEEE.

[3] Garaffa, L. C., Basso, M., Konzen, A. A., & de Freitas, E. P. (2021). Reinforcement learning for mobile robotics exploration: A survey. IEEE Transactions on Neural Networks and Learning Systems.

[4] Meyes, R., Tercan, H., Roggendorf, S., Thiele, T., Büscher, C., Obdenbusch, M., ... & Meisen, T. (2017). Motion planning for industrial robots using reinforcement learning. Procedia CIRP, 63, 107-112.

[5] Liu, Y., Xu, H., Liu, D., & Wang, L. (2022). A digital twin-based sim-to-real transfer for deep reinforcement learning-enabled industrial robot grasping. Robotics and Computer-Integrated Manufacturing, 78, 102365.

[6] Jayaramireddy, C. S., Naraharisetti, S. V. V. S. S., Nassar, M., & Mekni, M. (2022, October). A survey of reinforcement learning toolkits for gaming: applications, challenges and trends. In Proceedings of the Future Technologies Conference (pp. 165-184). Cham: Springer International Publishing.

CNN based steel plate fault detection

Taner GÖKÇIMEN[1], Emre DEMIREL[2], Rabia Gizemnur EREN[3], Beyda TAŞAR[4]

[1,2,3]Mechatroics Engineering, Engineering Faculty, Firat University, Elazig, Turkıye.

Abstract

Metals are essential building materials in today's world. Flat metal sheet manufacture and processing are extremely delicate procedures. Many pieces of equipment work on flat metals, from heating and rolling to drying and cutting. Defects on metal surfaces can occur for a variety of causes [1]. These include corrosion, erosion, cracks and fractures, wear, and coating defects, among others. Metal surface defects can be prevented or reduced through regular maintenance and proper material selection. Additionally, non-invasive inspection techniques can help in the early diagnosis of surface defects on metals, and numerous research efforts have been conducted in this regard [2], [3]. Preventing or correcting these defects can enhance the durability of metals, contribute to the construction of long-lasting products and structures, and reduce costs [4], [5].

Today, in many factories, image-based production error and deformation detection studies are carried out using high-frequency cameras to detect product defects that occur during the production of metal-based products [6], [7]. Image processing and deep learning-based fault diagnosis algorithms have been developed to make the production of metal-based products more efficient and aid in the early detection of production defects [8], [9].

The image data used in this study are real production defect image data from the Severstal Metal production factory. It is stated that each image in the dataset either has a single defect or belongs to multiple defect types class. For each image, the defects of each class are separated into sections (ClassId = [1, 2, 3, 4]). CNNs, which are widely employed for image classification, played a pivotal role in this study. Within the Python Jupyter environment, a CNN architecture was meticulously crafted. The dataset was meticulously partitioned into 771 training samples and 138 test samples to facilitate the training process. Post-training, the model's efficacy was rigorously assessed through a battery of tests involving previously unseen data. The proposed CNN framework boasts a total of 10 layers, comprising an input layer, 2 convolutional layers, 2 max-pooling layers, 2 dropout layers, 1 fully connected layer, 1 dense layer, and 1 softmax computation layer. Vgg16Net, despite its simplistic architecture, demonstrated superior feature extraction capabilities compared to ResNet. A feature map was methodically built from the training data using this model. Two multi-convolutional layers were followed by max-pooling and dropout layers in this novel architecture. The convolutional layers harnessed the power of filters to multiply input values by neuron weight values, thereby generating output values. During training, the search for optimal filters commenced with the generation of random filters. These filters were then employed in the convolutional layers to subject relevant image regions to convolutional processing, yielding feature maps or activation maps. Max Pooling was judiciously applied in the pooling layer. To put this into action, the developed CNN architecture was meticulously trained using 771 images representing four distinct labeled classes, alongside VGG16 and ResNet50 architectures. The network underwent intensive training for 500 epochs with a batch size of 64. Subsequently, the CNN model, along with ResNet50 and VGG16 transfer models, underwent rigorous testing using previously unseen data to evaluate their fault detection capabilities. The proposed CNN architecture achieved the most successful accuracy performance with an average accuracy of 95.14% when considering all classes. This was followed by ResNet50 with 85.42% and VGG16 with 81.51% accuracy, respectively.

Due to the high accuracy rate achieved with the developed methodological approach, it can be concluded that it is applicable in product quality control units in steel plate production facilities and can provide experts with decision support mechanisms.

Keywords: Metal surface, Fault diagnosis, CNN.

---

[1] Corresponding author

References

[1] S. M. Halawani, “a Study of Decision Tree Ensembles and Feature Selection for Steel Plates Faults Detection,” vol. 2, no. 4, pp. 127–131, 2014.

[2] K. Rajan, “Materials informatics,” *Mater. Today*, vol. 8, no. 10, pp. 38–45, 2005, doi: 10.1016/S1369-7021(05)71123-8.

[3] A. Kelly and K. M. Knowles, “Crystallography and Crystal Defects: Second Edition,” *Crystallogr. Cryst. Defects Second Ed.*, no. January, 2012, doi: 10.1002/9781119961468.

[4] A. Abdullahi, N. A. Samsudin, M. R. Ibrahim, M. S. Aripin, S. K. A. Khalid, and Z. A. Othman, “Towards IR4.0 implementation in e-manufacturing: Artificial intelligence application in steel plate fault detection,” *Indones. J. Electr. Eng. Comput. Sci.*, vol. 20, no. 1, pp. 430–436, 2020, doi: 10.11591/ijeecs.v20.i1.pp430-436.

[5] T. Nkonyana, Y. Sun, B. Twala, and E. Dogo, “Performance evaluation of data mining techniques in steel manufacturing industry,” *Procedia Manuf.*, vol. 35, pp. 623–628, 2019, doi: 10.1016/j.promfg.2019.06.004.

[6] A. Schumacher, T. Nemeth, and W. Sihn, “Roadmapping towards industrial digitalization based on an Industry 4.0 maturity model for manufacturing enterprises,” *Procedia CIRP*, vol. 79, no. July 2018, pp. 409–414, 2019, doi: 10.1016/j.procir.2019.02.110.

[7] W. S. Alaloul, M. S. Liew, N. A. W. A. Zawawi, and I. B. Kennedy, “Industrial Revolution 4.0 in the construction industry: Challenges and opportunities for stakeholders,” *Ain Shams Eng. J.*, vol. 11, no. 1, pp. 225–230, 2020, doi: 10.1016/j.asej.2019.08.010.

[8] J. K. M. P. J. HAn, *Data mining: Data mining concepts and techniques*. 2014.

[9] M. Perzyk, A. Kochanski, J. Kozlowski, A. Soroczynski, and R. Biernacki, “Comparison of data mining tools for significance analysis of process parameters in applications to process fault diagnosis,” *Inf. Sci. (Ny).*, vol. 259, pp. 380–392, 2014, doi: 10.1016/j.ins.2013.10.019.

International Conference on Advances and
Innovations in Engineering

Hand tremor detection Via 1D-CNN model

İrem Mertyüz[1], Ahmet Burak TATAR[2], Beyda TAŞAR[3]

[1,3]Mechatroics Engineering, Engineering Faculty, Firat University, Elazig, Turkıye.
[2]Mechanical Engineering, Engineering Faculty, Adiyaman University, Adiyaman, Turkey.

Abstract

The neuromuscular system, which consists of muscles and nerves, regulates motor functions in the human body. Neurodegenerative illnesses, in particular, induce motor function loss by affecting the structure and, as a result, the function of neurons. In this situation, the body undergoes reflex tremor movements [1, 2]. Tremors are caused by a variety of illnesses, including Parkinson's disease (PD), dystonia, multiple sclerosis, and traumatic brain injury [1, 3, 4]. According to a World Health Organization study, more than 10 million individuals worldwide, including over 150,000 in Turkey, seek medical treatment for tremors [3-5].

Tremors are divided into two types based on when they occur: activity tremor and resting tremor. The most frequent type of tremor is resting tremor, which arises as a result of a decline in dopamine production in Parkinson's disease. It occurs when body components are at rest and do not move voluntarily. Tremors occur at a frequency of 3-6 Hz in the hands and legs [7, 8]. Patients with essential tremor (ET) frequently have action tremors. This condition makes it difficult for these people to do daily tasks such as eating, writing, and washing [5, 9]. Tremors in the hands, head, and voice at frequencies ranging from 5 to 12 Hz are symptoms of Essential Tremor (ET) [7, 8]. ET can be caused by a variety of factors, including brain bleeding, brain traumas, adverse drug side effects, neurodegenerative illnesses, cerebellar injuries, and liver or thyroid insufficiency.

Tremors are often treated with pharmaceutical and surgical procedures. Medication, on the other hand, can cause a variety of side effects in some patients, including blurred vision, disorientation, weariness, and muscle weakness [10, 11]. When pharmacological treatment fails, patients are exposed to surgical techniques such as deep brain stimulation, magnetic resonance-guided focused ultrasound thalamotomy or gamma knife radiosurgery. Individuals who do not respond to this treatment and are not candidates for surgical intervention, on the other hand, require assistance equipment. There is a demand for equipment that helps people with untreatable tremors go about their daily lives.

This research focuses on involuntary tremors that occur during upper extremity exercises. Patients' daily activities are hampered by these tremors, which make eating, drinking, writing, holding a cup, and using keys difficult. Eating difficulties, in particular, can lead to a decrease in food intake, making it critical [12]. Furthermore, meal times are the most important social occasions in people's lives, as they assemble with their family and friends. Individuals who are unable to give their own sustenance efficiently and sufficiently owing to hand tremors face psychological challenges in society, which drives them to form partnerships [13].

This article addresses the difficulty of distinguishing between essential and Parkinsonian tremors. Although various methods have been proposed to diagnose these highly prevalent types of tremors, diagnosing them quickly and effectively, especially in their early stages, has been proven to be particularly challenging and complex due to their wide range of causes and the similarity of symptoms. In this study, a dataset collected from a group of volunteers, including patients diagnosed with essential and Parkinsonian tremors, was used [14]. When creating this dataset, patients were asked to perform a series of predefined movements, and a wearable inertial sensor device was used to measure forearm tremor characteristics. Within the scope of this study, an architecture of 1-dimensional CNN was developed to determine whether individuals have tremor disease or are healthy individuals. The results showed that

---

[1] Corresponding author

the proposed network architecture could diagnose hand tremor disease with 100% accuracy. The results indicate that the developed method can provide decision-support knowledge to experts.

Keywords: Hand tremor, detection, IMU data, CNN.

References

[1] NINDS Parkinson’s Disease Information: Focus On Parkinson’s Disease Research. (2021) Internet. 2021, 2020–2022

[2] Fraiwan L, Amir S, Ahmed F, Halepota J (2018) Design of a stabilisation platform for Parkinson’s disease patient. J Med Eng Technol 42:43–51 https://doi.org/10.1080/03091902.2018.1430183

[3] Pourfar MH, Louis ED (2006) Essential tremor. Curr Ther Neurol Dis, pp. 288–292 https://doi.org/10.1016/B9780323034326.500660

[4] Lava N, (2015) Understanding ALS.

[5] Abbasi M, Afsharfard A, Arasteh R, Safaie J (2018) Design of a noninvasive and smart hand tremor attenuation system with active control: a simulation study. Med Biol Eng Comput 56: 1315–1324, https://doi.org/10.1007/s11517-017-1769-9

[6] Crawford P, Zimmerman EE (2011) Differentiation and diagnosis of tremor. Am Fam Physician 83:697–702

[7] Bhidayasiri R (2005) Differential diagnosis of common tremor syndromes. Postgrad Med J 81:756–762, https://doi.org/10.1136/pgmj.2005.032979

[8] Bhidayasiri R, Maytharakcheep S, Phumphid S, Maetzler W (2022) Improving functional disability in patients with tremor: A clinical perspective of the efficacies, considerations, and challenges of assistive technology. J Neurol Sci 435:120197, https://doi.org/10.1016/j.jns.2022.120197

[9] Abbasi M, Afsharfard A (2018) Modeling and experimental study of a hand tremor suppression system. Mech Mach Theory 126:189–200, https://doi.org/10.1016/j.mechmachtheory.2018.04.009

[10] Case D, Taheri B, Richer E (2013) Design and characterization of a small-scale magnetorheological damper for tremor suppression. IEEE/ASME Trans. Mechatronics 18:96–103, https://doi.org/10.1109/TMECH.2011.2151204

[11] Case D, Taheri B, Richer E (2013) Multiphysics modeling of magnetorheological dampers. Int J Multiphys 7:61–76, https://doi.org/10.1260/1750-9548.7.1.61

[12] Cavalcanti A, Amaral MF, Silva e Dutra FCM, Santos AVF, Licursi LA, Silveira ZC (2020) Adaptive Eating Device: Performance and Satisfaction of a Person with Parkinson’s Disease. Can J Occup Ther 87:211–220, https://doi.org/10.1177/0008417420925995

[13] Nilsson MH, Iwarsson S, Thordardottir B, Haak M (2015) Barriers and facilitators for participation in people with Parkinson’s Disease. J Parkinsons Dis 5:983–992, https://doi.org/10.3233/JPD-150631

[14] Vasileios Skaramagkas, George Andrikopoulos, Zinovia Kefalopoulou, & Panagiotis Polychronopoulos.(2021). Arm Tremor Database - A Study on the Essential and Parkinson's Arm Tremor Classifi cation(Version 1) [Data set]. Zenodo. https://doi.org/10.5281/zenodo.4698248

Machine learning improvements to human motion classification with IMU

Rabia Gizemnur EREN[1] , Ahmet B. TATAR[2] , Beyda TAŞAR [3]

[1,3]Mechatroics Engineering, Engineering Faculty, Firat University, Elazig, Turkıye.
[2]Mechanical Engineering, Engineering Faculty, Adiyaman University, Adiyaman, Turkey.

Abstract

Inertial sensors have been used for dynamic modeling and vibration studies of cars, IHA, and the automotive sector for several decades [1,2]. Because of the rapid development of Micro-Electro-Mechanical Systems (MEMS), the size, weight, and cost of conventional inertial sensors have lately decreased considerably, making them wearable sensor devices. Some of these sensors are sensitive just along a single axis, whilst others are multi-axial (often over two to three axes). Wearable MEMS inertial sensors have opened up new avenues for monitoring, identifying, and categorizing human motion activities. These sensors are now being used in a wide range of potential applications human motion tracking, biomimetic, industrial robot application and mobile robot navigation.

This article focuses on the description of motion activities, and it discusses various methods that have been employed over the years. One of the earliest methods used for describing motion activities involves single or multiple video camera-based systems. Although image processing-based methods are still in use today, they come with many disadvantages. Camera systems require installation and usage within a home, laboratory, or office environment, limiting the workspace. Additionally, factors such as lighting and vibrations can affect the quality of camera data. Another disadvantage is that when a single camera is used during recording, the image is reduced to two dimensions, resulting in the loss of important information about the three-dimensional scene. In the method of using cameras to monitor human movements, markers (indicators) with lights or reflectors are placed on the human body body part in the surroundings. The positions of interest points are monitored, calculated, and tracked based on image-based changes. However, challenges arise when markers (indicators) are occluded or shadowed, hindering visibility and making motion tracking difficult.

MEMS IMU sensor can be placed on various parts of the body's front and back surfaces since they are wearable miniature sensors. Inertial sensors directly provide dynamic motion information through direct measurement. Inertial Sensors (MIMU) essentially consist of three sensor groups: accelerometers, gyroscopes, and magnetometers. The gyroscope provides angular rate information around a sensitivity axis, while accelerometers provide information about linear or angular velocity ratios. Application studies combining camera-based and accelerometer sensor-based activity recognition have also been documented in the literature [3]. Due to its high performance and possible applications, visual and inertial data fusion was sparked considerable attention, prompting the formation of workshops. Inertial sensor and magnetometer data fusion has also been studied [4]. When examining motion recognition studies, most involve relatively easily classifiable activities such as sitting, lying, standing, walking, descending stairs, and climbing stairs [5-7]. Signal processing and motion detection techniques, as well as sensor configurations, numbers, and types, vary from study to study [5-7]. There is no widely accepted protocol in this regard.

This study focuses on the classification of lower extremity activities (walking, running, descending stairs, sitting and standing) using a 9 DOF MIMU sensor (gyroscope, accelerometer, and magnetometer) worn on one leg. The study classifies three human movement modes (walking, running, standing) and device modes (held, in the pocket, on the backpack) and evaluates their accuracy using data from inertial sensor measurement systems (IMU) and sample-based methods. In this study, a model is proposed to recognize human activities using machine learning. Two motion

---

[3]Corresponding author

classification algorithms were used in this study: Decision Tree Classifier and Artificial Neural Network Classifier. The highest success rate, 99.92%, was achieved with the Decision Tree method.

Keywords: Machine Learning, Motion Classification, IMU.

Reference

[1] Ahmad, N., Ghazilla, R. A. R., Khairi, N. M., & Kasi, V. (2013). Reviews on various inertial measurement unit (IMU) sensor applications. International Journal of Signal Processing Systems, 1(2), 256-262.

[2] Seo, K. (2023, May). Real-Time Estimation of Walking Speed and Stride Length Using an IMU Embedded in a Robotic Hip Exoskeleton. In 2023 IEEE International Conference on Robotics and Automation (ICRA) (pp. 12665-12671). IEEE.

[3] Li, C., Yu, L., & Fei, S. (2019). Real-time 3D motion tracking and reconstruction system using camera and IMU sensors. IEEE Sensors Journal, 19(15), 6460-6466.

[4] Gong, J., Zhang, X., Huang, Y., Ren, J., & Zhang, Y. (2021). Robust inertial motion tracking through deep sensor fusion across smart earbuds and smartphone. Proceedings of the ACM on Interactive, Mobile, Wearable and Ubiquitous Technologies, 5(2), 1-26.

[5] Chen, Y. L., Yang, I. J., Fu, L. C., Lai, J. S., Liang, H. W., & Lu, L. (2021). IMU-based estimation of lower limb motion trajectory with graph convolution network. IEEE Sensors Journal, 21(21), 24549-24557.

[6] Madrigal, J. A. B., Rodríguez, L. A. C., Pérez, E. C., Rodríguez, P. R. H., & Sossa, H. (2023). Hip and lower limbs 3D motion tracking using a double-stage data fusion algorithm for IMU/MARG-based wearables sensors. Biomedical Signal Processing and Control, 86, 104938.

[7] Wei, W., Kurita, K., Kuang, J., & Gao, A. (2021, November). Real-time limb motion tracking with a single IMU sensor for physical therapy exercises. In 2021 43rd Annual International Conference of the IEEE Engineering in Medicine & Biology Society (EMBC) (pp. 7152-7157). IEEE.

Image-based detection of construction surface defects using deep learning methods

Muhammet Raşit BATUR[1] , İrem MERTYÜZ[2], Beyda TAŞAR[3]

[1,2,3]Mechatroics Engineering, Engineering Faculty, Firat University, Elazig, Turkey.

Abstract

Today's infrastructure projects and civil structures are essential elements that need to be long-lasting and reliable. These structures can be subjected to various damages over time due to the influence of many factors. One of the most common types of damage is cracks observed on concrete surfaces. Concrete structures are widely used in various fields such as highways, bridges, buildings, and dams, and their durability is of critical importance for controlling and preventing cracks. Cracks on concrete surfaces are significant flaws in construction structures. The detection of cracks plays a crucial role in assessing the stability and tensile strength of buildings during structural inspections, determining the overall health of the structures.

Cracks on concrete surfaces can occur due to various reasons, including physical factors, chemical reactions, deformation under load, weather conditions, and poor construction practices. These cracks can grow over time and jeopardize the durability and safety of the structures.

Effectively managing cracks is crucial for the sustainability and safety of concrete structures, making it a critical issue in the construction industry. This article focuses on the application of image-based methods for the early detection of cracks. Image-based defect detection on surfaces involves the use of advanced technologies such as high-resolution cameras and image analysis software to identify such issues. These technologies typically consist of three main components: cameras, image processing software, and learning algorithms. High-resolution cameras capable of capturing detailed images at a microscopic level are required. These cameras can record images from different angles and lighting conditions, allowing the detection of various surface defects. Image processing software is used for analyzing images, making pixel-level detections, and identifying surface irregularities and defects. Machine learning and artificial intelligence algorithms are also employed to detect the types and levels of defects on surfaces. Furthermore, the capacity of deep learning (DL) approaches to process and automate feature extraction from large-volume data enables DL to propose answers to actual fracture detection concerns [1]. Video frames were individually examined for crack detection using a combination of CNN and Naive Bayes [2]. CNN models have been utilized in various applications for detecting cracks, including pavement crack detection [3], asphalt surface cracks [4], automatic road crack detection [5], fractures in mechanical steel constructions [6], damage detection, steel corrosion, bolt corrosion, and steel delamination [7]. Thanks to advancements in hardware and computational software, deep convolutional neural networks (DCNNs) are now extensively employed for categorizing concrete crack images and detecting objects [8].

Image data contributed by Ozgenel F. on the Kaggle platform were used in this investigation [9]. Images of various concrete surfaces with and without cracks are included in these datasets. The image data for classification was separated into two folders: negative (no cracks) and positive (cracks). Each class has 20,000 photos, for a total of 40,000 images with RGB channels and 227 × 227 pixel size. To begin, picture preprocessing processes were used to resize the photos to (299, 299, 3). Following that, the photos were randomly divided into 70-30 training and test sets. This training data was used to retrain the previously trained Inception V3 model, and the model's performance was evaluated using the test data. In the binary classification problem (crack, intact surface), the network achieved a success rate of 99.9%. The results demonstrate that the proposed method excels in detecting surface defects. This study can be utilized for monitoring surface quality and early detection of defects in industrial or construction fields.
Keywords: Building, Surface Defect, Fault Diagnosis, Crack, Construction.

---

[1] Corresponding author

Reference

[1] ZhangK, Cheng HD, Zhang B (2018) A unified approach to pavement crack and sealed crack detection using preclassification based on transfer learning. J Comput Civ Eng 32:04018001.

[2] Chen FC, Jahanshahi MR (2017) NB-CNN: Deep learning-based crack detection using convolutional neural network and Naïve Bayes data fusion. IEEE Trans Ind Electron. https://doi.org/10.1109/TIE.2017.2764844.

[3] Fan Z, Wu Y, Lu J, Li W (2018) Automatic pavement crack detection based on structured prediction with the convolutional neural network. arXiv:1802.02208.

[4] Wang KC, Zhang A, Li JQ, Fei Y, Chen C, Li B (2017) Deep learning for asphalt pavement cracking recognition using convolutional neural network. Airfield and Highway Pavements, pp 166–177.

[5] Zhang L, Yang F, Zhang YD, Zhu YJ (2016) Road crack detection using deep convolutional neural network. In: IEEE international conference on image processing (ICIP), pp 3708–3712. https://doi.org/10.1109/ICIP.2016.7533052.

[6] Pauly L, Hogg RD, Fuentes, Peel H (2017) Deeper networks for pavement crack detection. In: Proceedings of the 34th ISARC. 34th international symposium in automation and robotics in construction, IAARC, Taipei, Taiwan, pp 479–485.

[7] Ren S, He K, Girshick R, Sun J (2017) Faster R-CNN: towards real-time object detection with region proposal networks. IEEE Trans Pattern Anal Mach Intell 39:1137–1149. https://doi.org/10.1109/TPAMI.2016.2577031.

[8] Rawat W, Wang Z (2017) Deep convolutional neural networks for image classification: a comprehensive review. Neural Comput 29:2352–2449.https://doi.org/10.1162/neco_a_00990

[9] Özgenel, Ç.F., Gönenç Sorguç, A. “Performance Comparison of Pretrained Convolutional Neural Networks on Crack Detection in Buildings”, ISARC 2018, Berlin.

A novel transformable wheel-leg mechanism design

İrem Meryüz[1], Ahmet B. TATAR[2] , Alper K. TANYILDIZI [3], Beyda TAŞAR[4], Oğuz YAKUT[5]

[1,3,4,5] Mechatronics Engineering, Engineering Faculty, Firat University, Elazig, Turkey.
[2]Mechanical Engineering, Engineering Faculty, Adiyaman University, Adiyaman, Turkey.

Abstract

Transformable wheeled-legged hybrid robots have become an important subject of research and development in the field of robotics in recent years. These robots have the ability to move with wheels while also using their legs to maneuver in challenging terrain conditions. These versatile robots offer significant potential benefits in various application areas, especially in exploration missions, rescue operations, agriculture, military purposes, and many others.

Traditional wheeled robots are effective on flat and smooth surfaces but have limitations in rough terrains and challenging conditions. On the other hand, legged robots can overcome such difficulties but are less effective on flat surfaces compared to wheeled robots. Transformable wheeled-legged hybrid robots combine the best features of these two worlds, making them capable of excellent performance in various tasks.

Research on robots with transformable segmented wheel structures has increased significantly in the last few decades. Tadakuma et al. [1], [2] introduced the Armadillo-Inspired Wheel-Leg Robot, featuring a wheel composed of three continuous segments connected by two joints. However, a significant drawback of this design lies in the wheel's substantial size, primarily due to each segment housing a motor and connecting elements. Kim et al. [3], [4] tackled this challenge in the Transformer Robot by adopting a segmented wheel structure and enhancing energy efficiency through a specialized mechanism, thus eliminating the need for motors within the wheel opening mechanism. Chou et al. [5] took a unique approach, conceiving the Transformable Claw Wheel Robot, where the two-part wheel configuration transforms into a structure with two two-fingered robots at the front and back, enabling it to navigate step-like obstacles with ease. The Quattroped robot [6] stands as a four-wheeled hybrid, featuring a two-part wheel mechanism that folds next to each other to assume a semi-circular shape when required, facilitating the traversal of step-like obstacles. Similarly, Lin et al. developed the TurboQuad robot, which boasts a two-part wheel structure capable of forming an S shape when necessary [7]. It's worth noting that the TurboQuad robot's energy consumption is somewhat higher due to the incorporation of actuators into the wheel system. On a different note, the four-part RDB robot [8] emerges as a versatile 3-degrees-of-freedom planar robot capable of transitioning between a chain and ring structure through joint configurations, allowing it to perform climbing, rolling, and walking motions. LEON [9] adopts a two-part wheel system using a similar transformation approach, coupled with four legs, each equipped with three degrees of freedom. When the transformable wheel structure is deployed, the robot takes on a hexapod configuration. In the case of RoVaLL [10], the robot features shape-changing wheels designed for movement across hard and soft soil terrains. A cam mechanism inside the wheel extends fingers when required, with the wheel's shape controlled by the torque applied to the cam mechanism. Researchers provided detailed explanations of the mechanism control, complemented by motion videos of the robot. Wang et al. [11] contributed the Leg-Wheel Transformable Robot, which focuses on analyzing the interaction between the wheel and the surface. This analysis leads to the creation of a concentric, two-part wheel mechanism capable of transforming into a finger mechanism depending on the terrain conditions. The researchers employ an RGB camera to explore and classify terrain roughness, enabling the robot to switch between leg-wheel mode based on this classification. WheeLeR [12] presents a mobile robot featuring a three-part foldable passive transformation mechanism. The robot's wheel incorporates a central gear and partial gears that rotate around it. When activated, this mechanism transforms the wheel configuration into three fingers. Researchers have meticulously designed five different transformable wheel structures with varying sizes and

---

[1] Corresponding author

gear ratios, rigorously testing them across various surface conditions. Lastly, LDR [13] takes a passive approach to its three-part wheel structure, triggering the mechanism upon contact with obstacles, thus eliminating the need for extra actuators. The LDR robot's prototype underwent practical testing, evaluating parameters such as maneuverability, stability, maximum obstacle clearance height, and transformation rate. Impressively, the robot demonstrated the capability to overcome obstacles with lengths up to 2.8 times the radius of its wheel. Developed by Mertyüz et al., FUHAR [14] is an innovative robot equipped with a six-part wheel structure. Each wheel integrates two motors, allowing the finger mechanism to open even while the robot is in motion, granting it the capacity to conquer obstacles with heights reaching 1.981 times its diameter.

This study provides details about the design of an original wheel structure for transformable wheeled-legged hybrid robots. The designed transformable wheel mechanism includes six finger elements that can move radially and open-close. There are two distinct states for the wheel, where the fingers are fully open and fully closed. The six fingers in the wheel are divided into two groups, with three on the right side of the wheel and three on the left side, allowing independent operation. In the design, the curvature of the fingers on the right and left sides is designed in opposite directions. This ensures equal grip on the ground when the wheel moves both forward and backward. When necessary and deemed sufficient, any three fingers on either side can be opened to enable movement. Additionally, having a larger number of fingers provides an advantage in reducing vibration. The mechanism that opens and closes the fingers is placed inside the wheel's main body. This mechanism is actuated by linear drive elements. Depending on the existing conditions, either a hydraulic piston-cylinder pair or a linear electric motor can be chosen. The mechanism that opens and closes the fingers is achieved by combining two different slider-crank mechanisms. Depending on the amount of motion of the drive elements, the fingers can be held in intermediate positions in addition to being fully open or fully closed.

Keywords: transformable wheel, wheel-leg, robot.

Reference

[1] Tadakuma, K., Tadakuma, R., Maruyama, A., Rohmer, E., Nagatani, K., Yoshida, K., ... & Kaneko, M. (2009, December). Armadillo-inspired wheel-leg retractable module. In 2009 IEEE International Conference on Robotics and Biomimetics (ROBIO) (pp. 610-615). IEEE.

[2] Tadakuma, K., Tadakuma, R., Maruyama, A., Rohmer, E., Nagatani, K., Yoshida, K., ... & Kaneko, M. (2010, October). Mechanical design of the wheel-leg hybrid mobile robot to realize a large wheel diameter. In 2010 IEEE/RSJ international conference on intelligent robots and systems (pp. 3358-3365). IEEE.

[3] Kim, Y. S., Jung, G. P., Kim, H., Cho, K. J., & Chu, C. N. (2014). Wheel transformer: A wheel-leg hybrid robot with passive transformable wheels. IEEE Transactions on Robotics, 30(6), 1487-1498.

[4] Kim, Y. S., Jung, G. P., Kim, H., Cho, K. J., & Chu, C. N. (2013, May). Wheel transformer: A miniaturized terrain adaptive robot with passively transformed wheels. In 2013 IEEE International Conference on Robotics and Automation (pp. 5625-5630). IEEE.

[5] Chou, J. J., & Yang, L. S. (2013, May). Innovative design of a claw-wheel transformable robot. In 2013 IEEE International Conference on Robotics and Automation (pp. 1337-1342). IEEE.

[6] Huang, K. J., Chen, S. C., Chou, Y. C., Shen, S. Y., Li, C. H., & Lin, P. C. (2011, May). Experimental validation of a leg-wheel hybrid mobile robot Quattroped. In 2011 IEEE International Conference on Robotics and Automation (pp. 2976-2977). IEEE.

[7] Lin, H. S., Chen, W. H., & Lin, P. C. (2015, May). Model-based dynamic gait generation for a leg-wheel transformable robot. In 2015 IEEE International Conference on Robotics and Automation (ICRA) (pp. 5184-5190). IEEE.

[8] Phipps, C. C., Shores, B. E., & Minor, M. A. (2008). Design and quasi-static locomotion analysis of the rolling disk biped hybrid robot. IEEE transactions on robotics, 24(6), 1302-1314.

[9] Rohmer, E., Reina, G., & Yoshida, K. (2010). Dynamic simulation-based action planner for a reconfigurable hybrid leg–wheel planetary exploration rover. Advanced Robotics, 24(8-9), 1219-1238.

[10] Luces, J. V. S., Matsuzaki, S., & Hirata, Y. (2020). RoVaLL: Design and development of a multi-terrain towed robot with variable lug-length wheels. IEEE Robotics And Automation Letters, 5(4), 6017-6024.

[11] Wang, T. H., & Lin, P. C. (2021). A reduced-order-model-based motion selection strategy in a leg-wheel transformable robot. IEEE/ASME Transactions on Mechatronics, 27(5), 3315-3321.

[12] Zheng, C., & Lee, K. (2019, May). WheeLeR: Wheel-leg reconfigurable mechanism with passive gears for mobile robot applications. In 2019 International Conference on Robotics and Automation (ICRA) (pp. 9292-9298). IEEE.
[13] Bai, L., Guan, J., Chen, X., Hou, J., & Duan, W. (2018). An optional passive/active transformable wheel-legged mobility concept for search and rescue robots. Robotics and Autonomous Systems, 107, 145-155.
[14] Mertyüz, İ., Tanyıldızı, A. K., Taşar, B., Tatar, A. B., & Yakut, O. (2020). FUHAR: A transformable wheel-legged hybrid mobile robot. Robotics and Autonomous Systems, 133, 103627.

International Conference on Advances and
Innovations in Engineering

Deep learning models for detection of lung infections training and evaluation

Canan KOÇ[1] , Fatih ÖZYURT [2]

[1,2]Software Engineering, Faculty of Engineering, Firat University, Elazig, Turkey.

Abstract

1. Introduction

Medical imaging has many techniques and is a branch of medicine used to diagnose and treat diseases. Techniques such as X-ray, magnetic resonance imaging (MRI), computed tomography (CT), ultrasonography, and positron emission tomography examine anatomical structures and pathological changes within the body. Medical imaging and deep learning constitute an essential field of study in analyzing medical images and diagnosing diseases (Huang, 2023). The first of these areas of study is medical image classification, where deep learning algorithms are used to detect cancer, tumors, or other pathological conditions by analyzing medical images such as MRI and CT scans. This field is the basis of the work done in this article. In addition to this application, applications such as automatic segmentation, neurological disease diagnosis, retinal images, diabetic retinopathy, and advanced radiology are examples of the merger of these two fields. The basis of all these applications is to help patients receive faster and more accurate diagnoses, allowing health professionals to support their work. The point to be noted here is that careful validation and regulation are required for these technologies to be used safely and effectively in clinical applications.

Medical image classification automatically analyzes and assigns images to a specific category and class. This classification process is used in applications based on diagnosing diseases, identifying pathological conditions, determining treatment options, and patient management. There are various examples of applications of machine learning or deep learning techniques, such as radiological diagnoses, histopathological image analysis, retinal images, and neurological disease diagnosis.

Machine learning and artificial intelligence techniques are used to analyze radiological images to diagnose and detect lung infections, especially diseases such as pneumonia. Applications in these areas enable medical images to be analyzed quickly and accurately. Thus, patients are enabled to access better diagnosis and treatment. However, the reliability and accuracy of such classification systems are of great importance and, therefore, require a strict verification and validation process. It is also important that health professionals evaluate the results of these systems and use them to make the final diagnosis.

2. Material And Methods

In the study conducted in the article, lung vision images taken from the open-source dataset were used (Kaggle). The dataset contains 10050 image data consisting of 5256 normal images, 4042 pneumonia images, and 752 tuberculosis-infected images. The images were obtained from multiple sites, including RSNA, Montgomery County chest X-ray set, Shenzhen chest X-ray, Qatar University, Doha, Qatar, and Dhaka University in Bangladesh and collaborators, and are available as open source.

---

[1] Corresponding author

This study examined the classification success of the data set consisting of lung images divided into three classes. Classification studies were performed with Convolutional Neural Network (CNN) based deep learning models and achieved a significant success rate (Liu, 2023).
The first of the models used in the study is AlexNet (Amanollah, 2023). AlexNet is a deep neural network model that is considered an important milestone in the field of deep learning. It consists of 8 layers, 5 of which are convolutional and 3 of which are fully connected. Convolutional layers are used to extract the features of the images. ReLU is used as an activation function. The overfitting problem is tried to be reduced by using dropout in the model. Another model used is the DenseNet161 model (Anjos, 2023). It is specially designed for large data sets and complex image classification tasks. It consists of Dense blocks and transition layers. Like ResNet, it is based on the idea of skip connections, which reduces overfitting problems and makes it possible to create deeper networks with fewer parameters. Another classification method used is the ResNet model (Ji, 2023). The main feature of the ResNet model is the use of link skipping or abbreviations, which makes it possible to make the network very deep and reduces overfitting. In addition, it uses Batch normalization to normalize the outputs to train the network faster and more stable. The main idea of ResNet is to skip connections that allow the network to capture the identity function better. This improves the training and generalization of the network. In the study, three different types of ResNet models were used.

3. Results

In this study, the lung image dataset obtained from open source was classified into three different groups: normal, pneumonia, and tuberculosis. In the study, the data were classified with multiple different deep learning models. In training these models, the number of epochs and learning rate were set as constant. The highest accuracy rate among the models used in the study is 91% obtained using denseNet161. In addition, the overall accuracy rate of the study is 87%. The lowest classification accuracy rate is 85.88%, obtained with AlexNet. The closest result to the accuracy rate obtained with AlexNet is 85.98%, obtained with ResNet18.

In addition to these studies, classification studies were also performed with ResNet50 and ResNet101 models. An accuracy rate of 90% was obtained with the ResNet50 model and 87% with the ResNet101 model.

4. Conclusion

This study investigated the performance of deep learning models on the classification of lung images using an open-source dataset. Our study used deep learning algorithms, including AlexNet, DenseNet161, and various ResNet models, to identify different lung conditions such as normal, pneumonia, and tuberculosis.

Our results show that these deep learning models are highly effective in classifying lung images. The highest classification accuracy was achieved with the DenseNet161 model at 91%. This result shows that this model is a powerful tool that can be used in the diagnosis of lung diseases. We also observed that other deep learning models, ResNet50 and ResNet101, also have high classification accuracies. The performance of these models can also be adapted for different datasets and tasks.

In conclusion, this study shows that deep learning techniques have great potential in medical image classification applications. These models can help healthcare professionals to make fast and accurate diagnoses. However, it is important to note that rigorous validation and regulation are required before these technologies can be used safely and effectively in clinical applications. This study highlights the potential in the field of medical image classification while providing a foundation for further research and development.

Finally, this study aimed to help patients receive faster and more accurate diagnoses through the combination of medical imaging and deep learning. Advances in this field could be an important step towards providing better patient care and treatment in medical applications.

Keywords: Lung Vision, Deep Learning, Classification

Structural and morphological characterization of waste toner powder considered as e-waste

Şeyda TAŞAR[1] , Melek YILGIN [2], Neslihan DURANAY[3], Dursun PEHLİVAN[4]

[1,2,3,4]Chemical Engineering Department, Engineering Faculty, Fırat University, Elaziğ, Turkey.

Abstract

In parallel with urbanization, industrialization, and population growth, the need for electrical and electronic equipment (EEE) is increasing exponentially. The wastes released in parallel with the widespread use of EEE's are called “e-waste” and contain both ecologically harmful and valuable components [1]. Production of e-waste worldwide was climbed by 9.2 Mt since 2014, and by 2030, it is anticipated to reach 74.7 Mt. It is known that the rapidly increasing amount of e-waste is mainly due to higher EEE consumption rates, and shorter life cycles. But, the EES's recycling activities cannot keep up with global growth [2].

Although the Chinese government has made great efforts to refill, renew and re-manufacture used toner cartridges within the scope of the "Waste electrical and electronic equipment recycling management regulation" that came into force in 2008, all over the world the number of discarded toner cartridges has increased rapidly. Despite the increase in digital communication and electronic e-signature document management systems in the last 20 years, printers and cartridges are still an important source of e-waste. Globally, approximately 375 million cartridges and approximately one million printer cartridges are included in the e-waste reserve every year. However, toner cartridges should be recycled and reused. This is at a scale that can contribute to both the prevention of waste and the maintenance of the national economy in the national framework.

Due to their short working lives, resistance to deterioration after being disposed of in a landfill, and incapability to be recycled or reused, toner cartridges make up a significant portion of electronic trash. They may also result in soil and water pollution when they are not disposed of in landfills, which poses numerous health risks [3]. Toner cartridges are expected to cause significant environmental issues shortly as a result. Therefore, in recent years, projects have started to be developed on the improvement of waste toner cartridges and waste solid processing at an international level [4]. In this research, it has been established that waste toner powder not only endangers the environment and human health but also possesses certain useful qualities and should be considered a waste [5]. Therefore, various studies have been started carried out for the evaluation of waste toner powder [6-8]. However, studies on the evaluation of waste toner powder in the energy sector are very limited. Studies on the energy sector; research on vacuum pyrolysis and product distribution/characterization of toner waste powder [9] and It is the production of waste egg trays and toner-derived high-efficiency 3d solar evaporators for freshwater production [10].

This study is a preliminary study designed to reveal the usability of waste toner powder in the energy sector, especially in the production of bio-briquettes. The second step is the process of evaluating biofuel aggregates as an energy source in the direct combustion process. In this context, first of all, the structure of the waste toner powder was tried to be revealed. Waste toner powders were obtained from a facility operating in the organized industrial zone, which was established for the recycling of toner cartridges within the provincial borders of Elazig. The structural properties, morphological properties, and fuel properties of the waste toner powders supplied and stored under suitable conditions were tried to be characterized and the obtained characterization results were interpreted. Structural and morphological properties of waste toner powder were tried to be revealed by FTIR, SEM-EDX, particle size distribution analyses, and fuel properties by proximate and ultimate analyzes and higher heating value (HHV) determination. Particle size distribution analysis was carried out in three different disperse media, and the dispersion behavior in different sedimentary media was examined. All analyses and tests were performed using standard test methods and calculated using generally accepted empirical equations. Obtained results showed that toner powder is a waste that should be evaluated in bio-briquette production applications, its combustion characteristics and behavior should be examined in detail, and it is a waste with high calorific value and binding properties.

References

[1] Nnorom, I.C. Osibanjo, O. “Overview of electronic waste (e-waste) management practices and legislations, and their poor applications in the developing countries”. Resour. Conserv. Recycl. 52, 843–858, 2008.

[2] Forti, V. Balde, C.P. Kuehr, R. Bel, G. “he Global E-Waste Monitor 2020: Quantities, Flows and the Circular Economy Potential; United Nations University (UNU)/United Nations Institute for Training and Research (UNITAR)–co-hosted SCYCLE

---

[1] Corresponding author

Programme”, International Telecommunication Union (ITU) & International Solid Waste Association (ISWA): Bonn, Germany; Geneva, Switzerland; Rotterdam, The Netherlands, 2020.

[3] Babar, S., Gavade, N., Shinde, H., Gore, A., Mahajan, P., Lee, K. H., Garadkar, K. “An innovative transformation of waste toner powder into magnetic g-C3N4-Fe2O3 photocatalyst: sustainable e-waste management”. Journal of Environmental Chemical Engineering, 7(2), 103041, 2019.

[4] Park, Y. Fray, D. 2009. “Recovery of high purity precious metals from printed circuit boards”, J. Hazard. Mater. 164, 1152–1158.

[5] Parthasarathy, M. “Challenges and emerging trends in toner waste recycling: a review”. Recycling, 6(3), 57, 2021.

[6] Arjunan, P. Kouthaman, M. Kannan, K. Diwakar, K. Priyanka V., Subadevi, R. Sivakumar. M. “Study on Efficient Electrode from Electronic waste renewed carbon material for sodium battery applications”. Journal of Environmental Chemical Engineering, 9 (2), 105024, 2021.

[7] Zhengshan Tian, Kesheng Cao, Suzhen Bai, Guoxu He, Jitao Li. “One-Pot Transformation of Waste Toner Powder into 3D Graphene Oxide Hydrogel”. ACS Sustainable Chemistry & Engineering 7 (1), 496-501, 2019.

[8] Zhengshan Tian, Lijuan Sun, Hao Tian, Kesheng Cao, Suzhen Bai, Jitao Li, Qiuxiang Zhu. “3D Graphene Oxide Hydrogel Derived from Waste Toner as Adsorbent”. Journal of Nanoscience and Nanotechnology, 21 (10), 5275-5281, 2021.

[9] Dong L "Pyrolysis Routine of Organics and Parameter Optimization of Vacuum Gasification for Recovering Hazardous Waste Toner", ACS Sustainable Chem. Eng. 5, 11, 10038–10045, 2017.

[10] Ivan N.A.S “Waste Egg Tray and Toner-Derived Highly Efficient 3D Solar Evaporator for Freshwater Generation”, ACS Appl. Mater. Interfaces 2022, 14, 6, 7936–7948, 2022.

Keywords: Waste toner powder, FTIR, SEM-EDX, Particle size distribution, Proximate and ultimate analysis

Investigation of the effect of non-perforated and perforated collector fins on pv surface temperature

Erhan ARSLAN[1]

[1]TÜBİTAK Marmara Research Center, Gebze, Kocaeli

Abstract

In this study, two different types of photovoltaic thermal collectors were designed to be embedded in the wall. The collector dimensions are designed to be 115x67x9 cm. The length of the winglets, the distance between the winglets and the distance from the side edges are designed as 95, 31 and 18 cm, respectively. The air selected as the working fluid for cooling the photovoltaic thermal collector is designed to enter the collector through the opening on the front surface and exit through the openings on the sides. For this purpose, the collector depth was made to be the same as the copper fins inside. Ansys program was used to perform numerical analysis. The CFX module, which has many sub-modules for computational fluid dynamics, has advantages over other modules in terms of ease of use in its interface, domain determination and the option to work with different turbulence models. Due to these advantages, the CFX module was preferred to perform numerical analysis in this study. The "Design Modeler" program, a subprogram of the Ansys program, was chosen to create the geometry of the collector. The numerical study was analyzed by considering two different situations. In the first case, the results were obtained without drilling the copper fins, and in the second case, the results were obtained by drilling the fins. In the second case, five elliptical holes were drilled into the copper fins, 2.5 cm wide, 4 cm long and 10 cm away from each other. Creating a mesh structure is defined as the process of dividing the geometric structure by the number of elements and nodes. As the number of elements or nodes increases, the accuracy of the results increases. The use of finer mesh elements at or near the wall provides good resolution of the boundary layer and temperature field gradients. This is especially important in flows containing a natural convection boundary layer. At the end of the build, "Fine" was selected in the suitability center and "medium" was selected to soften the size. The temperature and flow rate of the air entering the collector, which was numerically analyzed, were selected as 25°C and 0.02 kg/s, respectively, in all experiments. The solar radiation coming to the collector surface was chosen as 565 W/m2, which is the annual average radiation value of Ankara. This value is taken from GEPA. The fins were chosen as copper material and the thermophysical properties required for numerical analysis are given in Table 1. The sides of the collector are chosen as adiabatic walls. While the PV module surface was selected as "heat flux", other surfaces were introduced as "wall" and selected adiabatically. "No slip condition" has been applied to all walls. The mass flow rate was applied uniformly to the inlet area. The average static pressure in the outlet section is introduced as zero. In order to perform numerical analysis in the study, the optimum mesh number must be determined. In this study, in the analyzes performed on mesh numbers 7922-45309, the most suitable mesh number was determined as 45309, since the outlet air temperature differed by 0.05% and 0.06% from the previous mesh number for perforated and perforated collectors, respectively. Accordingly, the exit air and PV surface temperatures for both collectors were determined as 322.59; 458.66 and 326.53; 430.68, respectively. The initial and boundary conditions values of the numerical study were made so that the air inlet temperature and the ambient air temperature were the same. The "opening" pressure of the edges is 101325 Pa. The assumptions taken into account for the simulation are as follows:

- air is used as the working fluid.
- the collector is considered in three dimensions and steady state conditions are applied
- solar radiation is considered constant
- the flow is turbulent.

The convergence of the velocity components for their "residuals" is taken as 10E-6 in the continuity equation. A finite volume algorithm and a second-order upwind scheme were chosen to solve the main equations (continuity, momentum, energy). The SIMPLE algorithm was chosen to discretize the governing equations. The main equations, including fluid continuity, momentum and energy equations, were chosen to test the suitability and applicability of the model regarding their motion. Thermal and electrical efficiencies of the unperforated and perforated fin collectors are 78.2%, 10.72% and

---

[1] Corresponding author

91.01%, respectively; It is calculated as 10.91%. Only by drilling the fins, a 13.2% increase in thermal efficiency and a 0.19% increase in electrical efficiency was achieved. It was determined that the increase in efficiency was equal to 57.5 W and 1.29 W power, respectively.

As a result, the PVT collector with perforated fins exhibited better thermal and electrical efficiency.

Keywords: PVT collectors, CFD, Ansys, Cooling perform, Solar radiation

International Conference on Advances and Innovations in Engineering

Modeling of Reel-to-Reel Electrolytic Coating Line with Petri Nets in Process Mining

Ayşe AZATEŞ[1], Erhan AKIN[2], Ahmet Celal TOPKAYA[3], Mert ONAN[4]

[1]Department of Computer Engineering, Firat University,Elazığ,Turkey
[2]Hatko Teknik Hardware Representative and Trade Joint Stock Company, R&D Center, Istanbul, Turkey

Abstract

n the electrolytic plating method, the plating process of the products to be plated is carried out using an electric current in an electrolytic solution. Electronic and semiconductor components are produced with reel-to-reel electrolytic plating. These parts can usually be connector terminals, lead frames, connecting parts, protective caps. Compared to other plating methods, thinner and micron-level plating thicknesses can be obtained efficiently and economically. Terminals are plated at speeds up to 15 m/min in a multi-layer manner with materials such as gold, silver, nickel, copper, tin on a reel-to-reel plating line passing through various chemical baths. The process is very complex and there are hundreds of parameters that affect the plating quality and these show serious differences depending on the raw material, geometry and plating material of the plated terminal. Due to the complexity of the process, various errors can occur in coatings. In this study, the material strip is first shaped as pin terminals on the coating line and then selective coating is applied only to the desired areas on the surface. Our study was carried out on a special type of pin terminal for selective coating processes. In the coating process, the product to be coated is cleaned from dirt with ultrasonic degreasing. After the material to be coated enters the coating baths, rinsing is performed after each bath and finally drying is performed and after checking the terminal strip, it is wound and packaged. Since the electrolytic coating process is very complex, faulty production is inevitable. The most common errors encountered in terminals are low coating thickness, dullness and stains and similar unwanted errors can occur. These errors can result from changes in many parameters such as current, voltage, temperature, pH, liquid level in baths.

In the reel-to-reel electrolytic plating method, anomalies or deviations can be detected by analyzing the process with process mining to detect and correct errors in the continuously operating line during production. Suspicious, unwanted situations and rare events affecting the outcome in the coating line process are called anomaly detection. Unexpected situations or deficiencies in production arise with anomaly detection using Petri nets in process mining. In this study, it was aimed to analyze the behavior of the process and determine improvement areas by applying process mining to event logs taken from Hatko A. Ş's electrolytic plating line, which produces continuously up to 70 meters in length. Process mining techniques were applied to three event logs determined after the electrolytic plating process. The parameter values of event logs were classified according to zero, low, normal, and high values. Having all parameters within normal range values indicates ideal process management and is used to discover the most suitable process model. This process model is then used as a criterion to detect abnormality in examples where parameters are low, zero, and high. The open-source tool ProM 6.12, which is widely used for process mining, was used to perform our analysis. After examining the processes of the product produced on the electrolytic plating line in the line, data from event logs obtained were preprocessed and analyzed with process discovery algorithms. Thus, it has been revealed that it is possible to increase the quality and efficiency of the electrolytic plating process with process mining. The graphical appearance of the process was obtained with alpha, heuristic and inductive mining algorithms in ProM. The output of these algorithms is places, transitions and petri nets connecting them. A place represents a state of the process while a transition represents an activity. Arches connect places and transitions and show the flow of tokens representing the progress of the process. Data extracted from the automation system was preprocessed because it was not in a suitable format for process mining. Since the data obtained from the system did not make sense on its own, data on current, voltage, and temperature parameters were also obtained from sensors. The time spent in bath cells, the speed of the draw, and the length of the bath cell were calculated taking into account. The event log of continuous reel-to-reel electrolytic plating has been rearranged according to the time spent. Process models are discovered based on event logs prepared in the previous stage. There are various process discovery algorithms in process mining. It is very important to determine the appropriate algorithm according to the characteristics of the process. In this study, alpha miner algorithm, heuristic miner algorithm, and inductive miner algorithm were used

---

[1] Corresponding author

among process discovery algorithms. While arranging a 3-day event log taken from the automation system of a product that has selective tin and silver plating on nickel that we have determined to be used in process mining, we determined all processes and parameters. When creating the event log, it was first assumed that all processes were completed with normal values and event logs were arranged accordingly and a process model was created with process discovery algorithms. Later, a process model was created for each algorithm with event logs belonging to the coating process at three different times. In all mining algorithms worked in cases where all processes progress according to work order when the process is stable, a sequential petri net model is formed. We can be detected before the quality control process with process mining that production is faulty.

The biggest challenge of this study is data preprocessing and process discovery. With the process mining done with the arranged event logs, it was concluded that Inductive mining is the best mining for our process.

One of the areas of future work is to develop an automated system to convert event logs obtained from automation systems into event logs suitable for process mining-based analysis. The anomaly detection technique does not work in real-time. Techniques should be developed to process event logs in real-time. With process mining before the quality control step, it can be predicted whether the product is faulty and sent to packaging or scrapped.

Keywords: Electrolytic coating, Process mining, Petri nets, Inductive mining, Anomaly detection, ProM

Evaluation of Antimicrobial Activity Biosynthesized Silver Nanoparticle and Silver-Zinc Nanocomposites-Doped Hydroxyapatit

İlkay ÜNAL[1], Burcu AYDOĞDU[2], Mehmet AYTAR[3]

[1]Department of Gastronomy and Culinary Arts, Faculty of Fine Arts, Design and Architecture Education, Munzur University, Tunceli, Turkey.
[2]Department of Mechanical Engineering, Faculty of Engineering, Munzur University.Tunceli, Turkey.
[3]Department of Biology, Graduate School of Natural and Applied Sciences, Adnan Menderes University, Aydin, Turkey.

Abstract

Introduction: Nowadays, bone defects have become one of the important health problems due to many reasons such as aging, traumatic or non-traumatic injuries, various orthopedic diseases. Despite all these bone defects, bone also has the ability to heal and remodel itself, but its ability to regenerate decreases over time for various reasons. Hydroxyapatite (Ca10(PO4)6OH2), has recently attracted great interest in the biomedical field due to its chemical similarity to bone-forming minerals, biocompatibility with body fluids, bioactivity. osteoconductive property and thermodynamic stability. HA can be produced by different methods, either from synthetic materials or natural sources. HA which is produced by the wet process, contains impurities such as hydrogen phosphate, carbonate, chloride and sodium ions, leading to the formation of HA with low calcium content. The main disadvantage is also that high temperatures and long heat treatment processes are required. Natural hydroxyapatite is usually produced by calcination from fish bones, coral, cattle bones, eggshells, and shells. One of the main problems with the use of hydroxyapatite is that it has no antibacterial properties. Especially when it is used as a bone implant, the risk of infection increases, which is the main problem of modern reconstructive surgery. Therefore, additional factors that increase antibacterial activity around biomaterials are being investigated in implantation surgery. Metal and metal oxide nanoparticles have been extensively studied for their antibacterial properties and have shown promising results in combating bacterial infections. The production of nanoparticle-loaded materials is important in terms of providing long-term antibacterial properties. Silver nanoparticles have been extensively researched and are widely used due to their potent antibacterial activity. Similarly, zinc nanoparticles have shown antibacterial properties against various bacteria. Metal nanoparticles can be synthesized using various methods such as physical, chemical biological and green techniques. Green synthesis methods utilizing plant extracts are considered eco-friendly and sustainable compared to conventional chemical synthesis.

This study aimed to o investigate the synthesis, characterization and antimicrobial activity of silver and silver@zinc nanoparticle-doped HAp derived from sheep bone.

Material-Method: HAp powder was fabricated from sheep bone by thermal calcination with modifications to previously reported literature. AgNPs-HAp and Ag@ZnNPs-HAp were produced by the green bio-reduction method using Marrubium astracanicum called mountain tea extract, a plant species in Tunceli/Turkey. Firstly dried plant was weighed 20 g and mixed with a 1:2 ethanol/water mixture at 60°C for 10 minutes in a 250 ml beaker and filtered through filter paper. 0.01 M 100 mL AgNO3 solution was prepared. Next, 2 g of HAp powder was added to the AgNO3 solution and mixed for 30 minutes on a magnetic stirrer. Then, 10 ml of plant extract was added to the HAp-AgNO3 mixture and stirred at room temperature for 24 hours at 400 rpm. The solution was collected by centrifugation and filtration and washed with ethanol. To synthesize HAp-Ag@Zn nanocomposite, firstly, 100 mL of Zn(NO3)2 6H2O (0.05 M) and 50 mL of AgNO3 (0.01 M) solution were prepared and mixed in a 250 beaker. Next, the same procedure was applied to HAp-AgNPs synthesis The physicochemical properties of the prepared composite were characterized with X-ray diffraction (XRD), transmission electron microscopy (TEM), Fourier-transform infrared spectroscopy (FTIR) and scanning electron microscopy (SEM-EDX). The agar well diffusion method was used to examine the antimicrobial activity of HAp, AgNPs-HAp, and Ag@Zn-HAp nanocomposite against gram-negative Escherichia coli (E. coli, ATCC 25922), Pseudomonas aeroginosa (P. aeroginosa, PAO1), gram-positive Staphylococcus aureus (S. aureus, ATCC 25923) and Candida albicans (C.albicans 90028) fungus at three different concentrations (5, 10, and 20 mg/mL).

Result and conclution: The characterization results show that biosynthesis AgNPs and Ag@ZnNPs-doped hydroxyapatite

---

[1]Corresponding author

composite was successfully synthesized by a simple, inexpensive, and environmentally friendly method. According to the TEM results, nanoparticles were synthesized in different shapes and sizes. The characteristic peaks and 2θ values observed in the XRD curves confirm that the obtained materials are in the pure HAp, AgNPs and ZnO phase. and According to SEm-edx analysis results, the Ca/P ratio was 2.39, 2.10 and 2.20 for HAp HA which contains 39.68 wt% calcium and 18 wt% phosphorus, has a Ca/P molar ratio of 1.67. natural hydroxyapatite is not stoichiometric due to trace amounts of elements such as Na+, K+, Mg2+, Sr2+, Zn2+ and Al3+ or anions such as F-, Cl-, SO42- and CO3-2, which are found in natural sources. But these elements are useful because they promote bone regeneration AgNPs-HAp and Ag@ZnNps-HAp, respectively. AgNPs-HAp and Ag@ZnNPs provided effective bacterial resistance against Gram-negative, Gram-positive, and fungal strains with increasing concentration while pure HAp did not show any effect. Furthermore, adding Zn NPs increased the antibacterial activity through the synergistic effects of Ag+ and Zn+2

Keywords: Hydroxyapatite, Biosynthesis, AgNPs, Ag@ZnNPs, Nanocomposite, Antimicrobial Activity

Evaluation of The Antimicrobial Activity Of Silver and Zinc Nanoparticle Loaded- Multi-Walled Carbon Nanotube

İlkay ÜNAL[1]

[1]Department of Gastronomy and Culinary Arts, Faculty of Fine Arts, Design and Architecture Education, Munzur University, Tunceli, Turkey

Abstract

Introduction: Antimicrobial resistance is one of the most important health problems worldwide. The use of antibiotics in treatment causes many strains of bacteria to develop antibiotic resistance. New resistance mechanisms threaten treatment of infectious diseases. In this context, nanotechnological applications have shown significant developments. Metal and metal oxide nanoparticles (silver and silver oxide, titanium dioxide, zinc oxide, gold, etc.), which can inactivate microorganisms, are used for this purpose. Multiwall carbon nanotubes (MWCNTs) have potential applications in engineering, electronics and medicine due to their many attractive electrical, mechanical and thermal properties. In this study, multi-walled carbon nanotubes were decorated with different concentrations of silver and zinc nanoparticles to increase antimicrobial activity. a green synthesis method was used for the synthesis of nanoparticles, which is cost-effective, environmentally friendly and non-toxic. Marrubium astracanicum plant extract was used as a natural agent to reduce/stabilize NPs.

Material-Method: First, to functionalize the pristine multi wall carbon nanotube (50-100 nm, 95% purity) 4M HNO3 and 10M H2SO4 solution were prepared and mixed at a ratio of 1/3. Then, 1 g of pristine MWCNT was added to the mixing solution and stirred vigorously for 18 hours on a magnetic stirrer. It was dried in an oven at 120 °C for 24 hours. 20 g of the M. astracanicum plant was weighed and mixed in ethanol-water mixture at 60 ◦C for 20 minutes. 100 mL of 0.05 M silver nitrat (AgNO3)), 0.01M AgNO3, and 0.05M zinc nitrate hexahydrate Zn(NO3)2· 6H2O solutions were prepared using ethanol. 250 mg MWCNTs were added to 50 mL plant extract, and the salt solutions were added separately. The synthesized Ag-MWCNTs, Zn-MWCNTs and Ag@Zn-MWCNTs nanocomposites were characterized by X-ray diffraction(XRD), transmission electron microscopy (TEM), scanning electron microscopy-Energy Distribution Spectroscopy (SEM-EDX), Fourier transform infrared (FT-IR) and thermogravimetric analysis (TGA). Antimicrobial activity was tested against gram-negative Escherichia coli (E. coli, ATCC 25922), Pseudomonas aeroginosa (P. aeroginosa, PAO1), gram-positive Staphylococcus aureus (S. aureus, ATCC 25923) and fungal Candida albicans (C. albicans 90028) by using agar well method.

Results and Conclusıons: According to TEM images, it was seen that AgNP, ZnNP, and Ag@ZnNPs had irregular shapes and different sizes. The NPs are dispersed on the wall surface of the carbon nanotubes. Ag, O and Zn signals were observed in the EDX spectrum, confirming the presence of Ag on the ZnO surface. X-ray powder diffraction (XRD) patterns of the NP-loaded MWCNT powder samples were taken to determine the crystal structures. The characteristic peaks and 2θ values observed in the XRD curves confirm that the synthesized particles are in the pure Ag and ZnO phase. The characteristic stretching mode of Zn-O and Ag-O bonds is seen at 457 and 579 cm-1 in the FTIR spectrum. The silver and zinc content of MWCNTs was evaluated using TGA. Ag (0.05)-MWCNTs Ag(0.01)-MWCNTs Ag@Zn–MWCNTs and Zn(0.05)-MWCNTs now yielded 44%, 0.008%, 9% and 20% by weight, respectively. Likewise, Ag(0.05)-MWCNTs showed greater thermal stability than Ag(0.01)-MWCNTs. The increase in silver concentration increased the thermal stability. f-MWCNTs and Zn-MWCNTs did not show antibacterial activity for all strains, while Ag-MWCNT samples showed more significant antibacterial activity than positive control antibiotics in bacterial and fungal strains except E.coli. The increase in silver concentration increased the antibacterial effect. The results showed that Ag and Ag@Zn doped MWCNT had an antibacterial effect as effective as antibiotics.

Keywords: : MWCNTs, Green Synthesis, Silver Nanoparticle, Zinc Nnaoparticle, Antimicrobial activity

---

[1] Corresponding author

Chromium Recovery by Solvent Extraction

Şeyma YÜKSEL SAĞMAN[54], Mehmet Deniz TURAN[2], Ramazan ORHAN[3] Gökhan BAŞMAN[4],
[1]Eti Chrome Inc, Elazig, Türkiye
[2]Metallurgy and Materials Engineering, Faculty of Engineering, Fırat University, Elazig, Türkiye.
[3]Chemical Engineering, Faculty of Engineering, Fırat University, Elazig, Türkiye.
[4]Eti Chrome Inc., Elazig, Türkiye.

Abstract

Solvent extraction is a liquid-liquid extraction, and it is a suitable method used in the extraction of low concentration charged metal solutions in recent years, enabling the removal of valuable and/or non-valued metal ions from charged solutions. It is also economical in terms of regenerating the solvent used and evaluating low grade ores. In addition, it is cheaper than pyrometallurgical methods and pollutes the environment and the atmosphere less. In this study, it is aimed to selectively remove the chromium compounds found in the wastes generated in the ferrochrome production facilities of Eti Krom Inc. Thus, environmental awareness will be gained and environmental pollution caused by chromium will be at a minimum level.

Keywords : Solvent extraction, chrome, environmental pollution

1. Introduction

In liquid liquid extraction, the mixture of two miscible liquids, one of which is soluble, is presented as the alternative diluent, the treatment exchange with a third liquid known as the solvent consists of two separate liquid phases in which the solvent is unmixed or partially mixed. It is applied by taking advantage of the density difference of two liquids [1]. When the mixture is placed in the separating funnel, the liquid with the lower density is collected at the top and the larger one is collected at the bottom. Substances with similar densities cannot be separated easily. The solvent-rich phase is called the extract, and the residual liquid phase, which is free from solute, is called raffinate [2].

In this study, a study was carried out to remove chromium from the wastes in the Eti Krom A.Ş. Facility by solvent extraction. Cr (VI) removal studies were carried out from waste, which initially contained 163 mg/L Cr (VI). The optimum values in chromium removal studies are studies with S:O (solution organic) 1:0.5 and S:O 1:3. In both studies, the chromium removal percentage is 55.75%. When evaluated in terms of cost, it is more economical to determine the operation with a low solvent amount of S:O 1:0.5 as the optimum operation.

2. Material and Methods

Experiments were performed to determine the optimum amount of solvent. In the studies, firstly, 150 g of flue dust was mixed with 1500 liters of tap water for 15 minutes and filtered to obtain a stock Cr (VI) solution. The Cr (VI) value of the solution is 163.3055 mg/L. In the studies, stock Cr (VI) solution Cyanex 923 and toluene were mixed in a beaker for 15 minutes at 550 rpm. pH values were recorded and taken into the separatory funnel for resting. After a 5-minute rest period, the solutions were taken and Cr(VI) and total Cr values were analyzed and Cr removal percentages were calculated.

In this study, the amount of aqueous solution, amount of organic matter, amount of toluene, mixing time and resting time are fixed, but the S:O ratio varies.

The studies carried out are given in Table 1.

---

[54] Corresponding author

Table 1. Solvent Extraction Experiments

Parameters	Variables	Variables	Variables
S:O (solution: organic)	1:0,5	1:1	1:2
Amount of Aqueous Solution (ml)	20	20	20
Amount of Organic Matter (ml)	9	19	39
Amount of Toluene (ml)	1	1	1
Mixing Time (min)	15	15	15
Resting Time (min)	15	15	15
pH	4,987	4,98	4,96
Filtered Solution (organic)pH	4,685	4,73	4,85
Filtered Solution Cr (VI) (mg/L)	74,3	22,2	0,555
Filtered Solution AAS Result (Total Cr Amounts) (mg/L)	90,88	35,48	2,476

The studies carried out are shown in Figure 1.

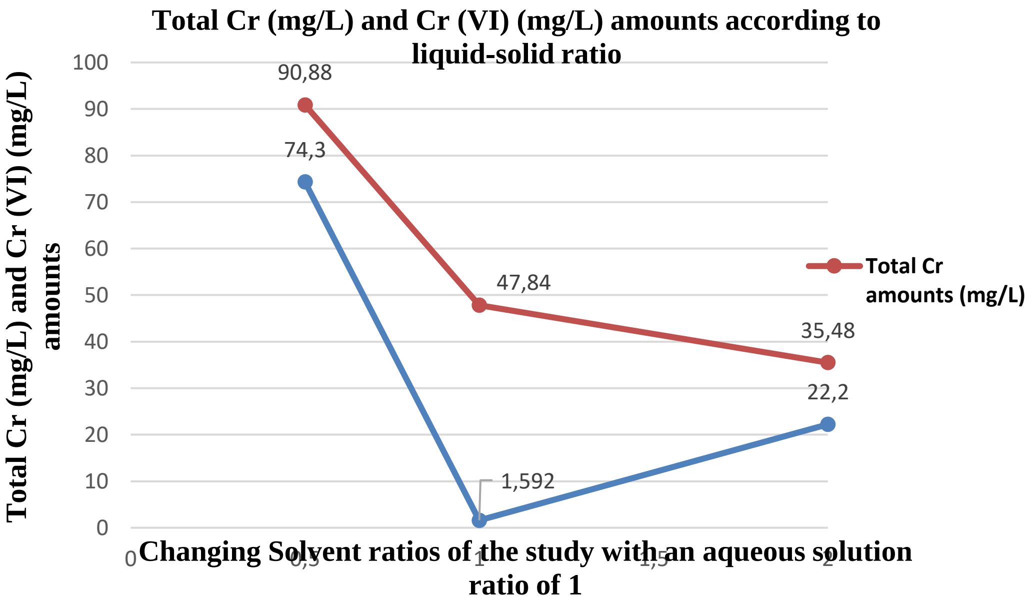

Figure 1. Solvent Extraction Experiments

3. Results

In the studies, the liquid remained constant at the S:O ratio and the amount of organic matter was increased gradually. In studies with S:O 1:0.5, 1:1, 1:2, chromium removal percentages are 55.75%, 21.8 and 1.52, respectively. Studies show that as the amount of organic matter increases, the chromium removal efficiency decreases. The optimum removal is the study in which the S:O ratio is 1:0.5 and the removal percentage is 55.75%. The study is promising due to the high prices of organic matter. The organic material used in this study is economical because it is regenerated. How much work can be done for organic matter regeneration will be determined in future studies. The fact that solvent extraction is both practical and cheaper than other methods makes it attractive. When evaluated in terms of cost, this study is both cheaper and more practical than other pyrological methods in the literature. This work does not create a carbon footprint and is also environmentally friendly.

4. Acknowledgements

We would like to thank Eti Krom A.Ş for providing raw material and analysis support in the studies.

5. References

[1] Öztürk, A. 'Sıvı sıvı ekstraksiyonu ile maya atıksuyu membran çıkışından uçucu yağ asidi geri kazanımı'. İstanbul Teknik Üniversitesi Fen Bilimleri Enstitüsü Yüksek Lisans Tezi, 2014
[2] Ying, Z., Ren, X., Li, J., Wu, G., & Wei, Q., 'Recovery of chromium(VI) in wastewater using solvent extraction with amide'. Hydrometallurgy, 196, 105440, 2020.

Modelling of Oxytetracycline Adsorption from Aqueous Solutions by Fe3O4-MWCNTs

Özlem ERDAL[1] , Veyis SELEN[2]
[1,2]Bioengineering, Engineering Faculty, Fırat University, Elazığ, Turkey.
[1]ozlemerdal6@gmail.com, [2]vselen@firat.edu.tr

[1](ORCID: 0000-0002-4468-8631), [2](ORCID: 0000-0003-0016-0840)

Abstract

Antibiotics are pharmaceuticals that are frequently used in medicine for the treatment of diseases, in veterinary medicine for the prevention of infections and growth promoters, on farms as feed additives, and in agriculture for the protection of crops. The antibiotics, which are not completely metabolized in the body, are thrown into the nature through urine and feces and cause waste containing antibiotic residues in the environment. Thus, it leads to both water and soil pollution in the environment and the development of antibiotic resistance in living receiving environments. While this makes the treatment of existing diseases difficult, it also brings about the emergence of new diseases. Therefore, it is extremely important to remove antibiotics before they are introduced into the receiving environment.

In this study, the removal of oxytetracycline (OTC) antibiotics, which are frequently used in human and veterinary medical applications, from aqueous solutions using magnetic multi-walled carbon nanotubes (Fe_3O_4-MWCNT) was investigated. Synthesis of Fe_3O_4-MWCNT was carried out by chemical co-precipitation method and all experiments were modeled using the Response Surface Method (RSM). In the modeling study, parameters effective on percentage of antibiotic removal selected as the response variable and independent variables were selected as the initial pH of solution, the concentration of antibiotic, the concentration of Fe_3O_4-MWCNT and the contact time. The experimental design was designed using five different levels of each parameter according to Central Composite Design (CCD), and the independent variables for the removal of OTC antibiotics, their experimental values and their levels for CCD are given in Table 1. As a result of variance analysis (ANOVA), high regression coefficients (R^2=0.971; R^2_{Adj}=0.943; R^2_{Pre}=0.831) were obtained for OTC removal.

Keywords: Adsorption, Antibiotics, Response Surface Method, Fe_3O_4-MWCNT.

Table 1. Independent variables for OTC removal, experimental values and levels for CCD

Independent variables	Kod	-2.0 (-α)	-1.0 (Low)	0.0 (Central)	+1.0 (High)	+2.0 (+α)
Initial pH	A	2.0	4.0	6.0	8.0	10.0
Initial concentration of antibiotic, mg/L	B	15	30	45	60	75
Concentration of Fe_3O_4-MWCNT, g/L	C	0.25	0.50	0.75	1.0	1.25
Contact time, min	D	6	12	18	24	30

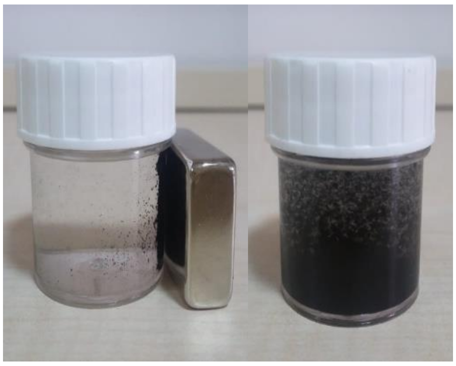

Figure 1. Separation of Fe_3O_4-MCCNTs from antibiotic solutions with neodymium magnet

---

[1] Corresponding author

The synthesis of multi-walled carbon nanotube (Fe_3O_4-MWCNT) with magnetic character, which will be used in the removal of antibiotics from aqueous solutions containing antibiotics, was carried out using the chemical co-precipitation method.

$$FeCl_2.4H_2O + 2\ FeCl_3.6H_2O + 8\ NH_4OH \longrightarrow Fe_3O_{4\ (s)} + 8\ NH_4Cl + 20\ H_2O \tag{1}$$

$$Fe_3O_4 + \text{ÇDKNT} + 20\ H_2O \longrightarrow Fe_3O_4\text{-ÇDKNT}_{\ (s)} \tag{2}$$

As a result of analysis of variance (ANOVA) obtained using Design Expert 10 software, effect values for linear, binary interactions, quadratic and cubic parameters were defined. The statistical results obtained from the application of different mathematical models are shown in Table 2 for OTC.

Table 2. Statistical results of models for OTC

Source	**p-value**	**Lack of Fit p- value**	**Adjusted R^2**	**Predicted R^2**
Linear	< 0.0001	< 0.0001	0.8106	0.7522
2FI	0.9690	< 0.0001	0.7663	0.7471
Quadratic	< 0.0001	< 0.0001	0.9430	0.8308
Cubic	0.6862	< 0.0001	0.9322	-1.3354

In the analysis of variance performed for OTC antibiotics, the quadratic model was found to be significant at the 95% confidence level with the Prob>F value <0.0001, and it was determined that the model terms B, C, D and A^2, where the Prob>F value was less than 0.05, were effective in the adsorption of OTC. In addition, the Prob>F value of the C^2 model term was found to be 0.0512, which is close to 0.05, so it was accepted that it would be effective in the adsorption process. Prob>F values of linear, quadratic and interaction terms are presented in Table 3.

Table 3. Analysis of variance (ANOVA) for quadratic model and regression coefficients on the response surface of OTC removal.

Source	**Sum of squares**	**DF**	**Mean square**	***F*-value**	**Prob > F**
Model	8151.31	14	582.24	35.28	< 0.0001
B-Initial OTC Conc.	2745.83	1	2745.83	166.38	< 0.0001
C-Fe_3O_4-MWCNT Conc.	4095.36	1	4095.36	248.15	< 0.0001
D-Contact Time	185.65	1	185.65	11.25	0.0043
A^2	852.08	1	852.08	51.63	< 0.0001
C^2	70.10	1	70.10	4.49	0.0512
Residual	247.55	15	16.50		
Lack of Fit	246.38	10	24.64	104.81	< 0.0001
R^2	0.971				
R^2_{Adj}	0.943				
R^2_{Pre}	0.831				
Standard Dev.	4.06				
C.V. %	6.26				
PRESS	1420.82				
Adeq Precision	21.90				